COUPLED FLUID FLOW AND GEOMECHANICAL MODELING FOR UNCONVENTIONAL FIELD DEVELOPMENT OPTIMIZATION AND INDUCED SEISMICITY ASSESSMENT

A Dissertation

by

JAEYOUNG PARK

Submitted to the Office of Graduate and Professional Studies of
Texas A&M University
in partial fulfillment of the requirements for the degree of

DOCTOR OF PHILOSOPHY

Chair of Committee,	Akhil Datta-Gupta
Committee Members,	Michael J. King
	Hadi Nasrabadi
	Debjyoti Banerjee
Head of Department,	Jeff Spath

May 2021

Major Subject: Petroleum Engineering

ABSTRACT

Fluid injection and extraction activities in subsurface result in disturbance of pressure and stress field underground. Such disturbance might intentionally or unintentionally cause the failure of geo-material. For example, hydraulic fracturing involves injection of large fluid volume with high injection pressure to enhance permeability and contact surface area for economically exploiting hydrocarbon from tight formation. Understanding hydraulic fracture geometry and underlying mechanisms and their impacts on well performance are key factors in the success of unconventional field development. Disposal of large volume of produced water into subsurface alters stress and pressure fields as well and it can cause the failure of faults in deep crystalline basement. The failure and slip along fault planes sometimes produce earthquakes which can damage properties on surface. Therefore, it is essential to assess and manage risks associated with fluid injection and production to minimize potential seismicity. To address the aforementioned challenges in unconventional field development and fluid-induced seismicity, this dissertation discusses studies related to coupled fluid flow and geomechanical modeling workflows.

First, we developed a novel hybrid Fast Marching Method-based simulation (FMM-Sim) workflow for history matching and completion optimization of hydraulically fractured wells. We introduced pressure-dependent fracture property curves, based on empirical relationship, lab experiments and theoretical background, to mimic fracture propagation and closure in reservoir simulations. Therefore, we can capture the impact of completion design such as injection fluid volume and cluster spacing on the well performance.

Second, we built a hybrid model, combining physics-based reservoir simulations and machine learning algorithms for unconventional reservoirs. The simulation input and output were incorporated into machine learning algorithms such that the algorithms can learn underlying physics between simulation input (e.g. completion design) and output (e.g. cumulative oil production). The hybrid model provides fast and scalable applications for unconventional field development with high accuracy which makes the hybrid modeling approach more suitable for field applications.

Third, we utilized one-way coupled fluid flow and geomechanical simulations with detailed fault modeling in the Azle area, North Texas to quantitatively assess potential for induced seismicity. We incorporated fault geometry based on the operator's seismic survey into flow and geomechanical simulations and assessed fault slip and fault frictional energy. The fault frictional energy was then compared with the radiated energy from the observed earthquakes to build empirical seismological model. The seismological model was used to predict earthquake frequency with different injection/production operations.

DEDICATION

To Haemin and Hannah

ACKNOWLEDGEMENTS

First of all, I would like thank my committee chair, Dr. Datta-Gupta, for his guidance and support throughout my Ph.D. journey. I truly understand that it is such a blessing to complete a graduate study with an advisor who sincerely cares graduate students responsibly and is interested in seeing the students growing patiently. Dr. Datta-Gupta was not simply an academic advisor for me but he also presents a role model that inspires me for how to succeed in my upcoming professional life after the graduate school.

I also would like to thank Dr. Michael King in my committee members who always throws intriguing and challenging questions that stimulate intellectual curiosity. A conversation with him is always enjoyable and has me learn something new or have a new idea, which was helpful in carrying out my graduate research. I would also remember and thank his warm kindness that he dropped me and other two graduate students off around mid-night after 6-hour long drive from Austin after a meeting at Bureau of Economic Geology due to a heavy snowstorm. It was definitely a memorable road trip during my Ph.D. program.

My thanks go to other committee members, Dr. Hadi Nasrabadi and Dr. Debjyoti Banerjee as well. They were always supportive and responsive when I needed their help. I feel grateful for their help and comments throughout my Ph.D. study.

During my Ph.D. program, I was privileged to be a part of Model Calibration and Efficient Reservoir Imaging (MCERI). It offers me priceless opportunities to directly interact with industry sponsors and other institutions. Collaborating with them provides me other aspects than graduate research and it broadens my perspective in the oil and gas industry. I especially thank Anadarko Petroleum, Bureau of Economic Geology, ExxonMobil, Parsley Energy, and Occidental Petroleum for collaboration and internship opportunities. Preparing MCERI annual meetings was the best time to revisit my research progress with advisors. It gave me opportunities to learn how I should present myself professionally and respectfully, and to deepen my understanding of ongoing cutting-edge researches in the group, getting new ideas and inspirations.

I would like to thank my friends and mentors in MCERI as well. Throughout the graduate study, we have supported and helped each other and worked on many great projects. It was a great pleasure working with brilliant people around the world. I specifically thank Jixiang Huang, Atsushi Iino, Xu Xue, Rongqian Chen, Hongquan Chen, and Tsubasa Onish who helped me start my research and shared their experience and opinion, working on projects together. Occasional small chit-chat and laughter with MCERI friends were joyful moments during my graduate study as well.

Lastly, my family has been a great support all the time. My daughter, Hannah, was a great help in understanding and behaving well while her busy dad could not spend more time with her during weekends and night times. It was my wife who walked through this journey with me and who makes our growing family together while pursuing her own doctorate degree, which was not easy. I feel fortunate that she is the one who stands by me and I believe we will do well whatever it takes for a new start.

CONTRIBUTORS AND FUNDING SOURCES

Contributors

This work was supervised by a dissertation committee consisting of Professor Akhil Datta-Gupta (advisor), Michale J. King and Hadi Nasrabadi of the Department of Petroleum Engineering and Professor Debjyoti Banerjee of the Department of Mechanical Engineering.

The Fast Marching Method-based simulation code for Chapter 2 was provided by Atsushi Iino. The CMG model setup in Chapter 4 was helped by Rongqiang Chen.

All other work conducted for the dissertation was completed by the student independently.

Funding Sources

Graduate study was supported by Texas A&M University Joint Industry Projects (JIP), Model Calibration and Efficient Reservoir Imaging (MCERI). I appreciate MCERI members' support and interaction throughout my graduate study.

Computing Sources

Portions of research in Chapter 2 and Chapter 4 were conducted with high performance research computing resources provided by Texas A&M University.

NOMENCLATURE

P_{fi} = Fracture initiation pressure (psi)

w_{ini} = Initial fracture width (in)

$Trans.MLT_{ini}$ = Transmissibility multiplier (dimensionless)

$Trans.MLT_{ini}$ = Transmissibility multiplier at P_{fi} (dimensionless)

k_{rf} = Fracture residual permeability ratio (dimensionless)

K_n = Fracture stiffness (MPa/mm)

$PV.MLT$ = Pore-volume multiplier (dimensionless)

c_{pp} = Porosity-permeability coefficient

MLT_{PV} = Pore-volume multiplier for completion cells

MLT_{TR} = Transmissibility multiplier for completion cells

K_{romax} = Maximum relative permeability for water

K_{rwmax} = Maximum relative permeability for oil

N_w = Water exponent for Brooks-Corey functions

N_o = Oil exponent for Brooks-Corey functions

S_{wc} = Critical saturation of water

S_{or} = Residual saturation of oil

TABLE OF CONTENTS

Page

LIST OF FIGURES

LIST OF TABLES

CHAPTER I

INTRODUCTION

Introduction

Fluid injection and extraction activities in subsurface result in the change of pore pressure and/or stress field underground. Although the changes in pressure and stress are not independent, in most cases, numerical simulations of fluid flow in porous media are decoupled with geomechanics. This is because updating mechanical change of flow properties without solving geomechanical equations is sufficient to capture flow mechanisms in most reservoirs. For example, the porosity modification due to reservoir pressurization or depletion is actually function of total strain change while its modification is generally described as function of pressure in reservoir simulations. However, when it associates with large scale deformation or the failure of the formation, which leads to substantial change in flow properties, it is necessary to couple geomechanics with fluid flow to adequately capture flow mechanisms and its consequence. The examples include reservoir depletion and subsequent subsidence, fluid-induced fault reactivation and associated seismic events, and hydraulically fractured well performance in unconventional reservoirs. This dissertation specifically addresses coupled fluid flow and geomechanical modeling and its applications for unconventional field development optimization and fluid-induced seismicity assessment.

The advent of multistage hydraulic fracturing techniques along with long lateral horizontal wells enable economic production of hydrocarbon from tight formations. The key challenge in unconventional field development is to find the optimum number of wells to place in a section or given area to efficiently recover hydrocarbon. Current practices in unconventional field development highly depend on pure curve-fitting like Decline Curve Analysis (DCA) and data-driven approach like machine learning and Rate Transient Analysis (RTA), which is based on simplified physics. Even though these tools are fast and scalable, they do not serve fidelity simultaneously. To address complex dynamics in unconventional reservoirs including parent and child well interaction, physics-based reservoir simulations are still essential. However, common practices in the industry model hydraulic fractures in a stand-alone tool and consequent fracture parameters are transferred to flow simulators. This requires extensive resources, manpower, and additional efforts to resolve the compatibility issue between two simulators. Furthermore, the speed of traditional simulation-based decision support for unconventional field development might have limitations to provide scalable applications, given the pace of current operations and the number of newly drilled wells. In order to bridge the gap, we introduce a simplified physical model to represent the mechanical behavior of fracture properties as function of pressure. The model mimics fracture propagation and closure in reservoir simulations and is validated with ABAQUS, a fully coupled fluid flow and geomechanical simulator. To amplify the computation efficiency, we incorporated the model into FMM-Sim, and machine learning algorithms such that the workflow can provide fast and scalable applications with underlying physics to capture the interaction between fracture geometry and well spacing.

Another coupled fluid flow and geomechanical modeling application is to assess fluid-induced seismicity. Anthropogenic fluid activities can possibly induce or trigger earthquakes, altering pore pressure and/or stress on fault plane. There are two main mechanisms associated with such earthquakes. The first mechanism is due to direction interaction with pore pressure. The increase in pore pressure decreases effective normal stress along the fault plane leading to reactivation of the faults. The second mechanism is due to poroelastic effect. The mass or volume change away from the faults can modify the loading condition onto the fault plane. This results in the change of stress state, invoking the reactivation of the faults as well. Though the reactivation of the faults does not always produce seismic events, it is important to assess and manage risks associated with oil and gas activities-related seismicity, especially in the area like Forth Worth Basin (FWB), North Texas. FWB is a metropolitan area where active hydrocarbon production and produced water disposal are ongoing with the increase in seismic event frequency for the last decade. The Azle area in FWB, the area of interest in this dissertation, experienced a series of earthquakes around 2014 while most of larger events occurred in the crystalline basement, far deeper than the reservoir. We employed computational coupled fluid flow and geomechanics for the area to assess potential induced seismicity, given operational conditions. The computational coupled fluid flow and geomechanics can account for poroelastic effect which can induce fault reactivation without direct pressure interaction by solving actual stress and pressure change in the basement. Also, we can evaluate the post failure behavior of faults including fault slip and fault frictional energy, which can be used to build an empirical seismological model to predict the earthquake frequency.

This dissertation consists of three chapters of coupled fluid flow and geomechanical simulation applications: two chapters dealing with unconventional field development and the last chapter dealing with fluid-induced seismicity.

Dissertation Outline

The overarching theme in this dissertation is to utilize coupled fluid flow and geomechanical modeling and its applications to address challenges in unconventional field development optimization and fluid-induced seismicity assessment. The dissertation is comprised of three chapters and the objective of each chapter is summarized below.

In Chapter II, we extended the rapid reservoir simulation technique, FMM-based simulation to injection phase of hydraulically fractured shale wells. This enables us to efficiently evaluate the completion design for field development planning and economic decision making on top of forecasting well performance through rapid history matching.

In Chapter III, we combined physics-based reservoir simulations and machine learning algorithms to build a hybrid model. Thus, the model can provide fast and scalable applications for unconventional field development with underlying physics to provide high accuracy.

In Chapter IV, we incorporated detailed fault configuration from field data into flow and geomechanical simulation models to quantitatively assess potential fluid-induced seismicity. The site-specific empirical seismological model was built by correlating the observed earthquakes and fault frictional energy from the geomechnical simulation model to predict the earthquake frequency at given operational conditions.

CHAPTER II

NOVEL HYBRID FAST MARCHING METHOD-BASED SIMULATION WORKFLOW FOR RAPID HISTORY MATCHING AND COMPLETION DESIGN OPTIMIZATION OF HYDRAULICALLY FRACTURED SHALE WELLS*

Chapter Summary

This chapter introduces a novel hybrid Fast Marching Method-based simulation (FMM-Sim) workflow for rapid history matching and completion design optimization of hydraulically fractured shale wells in unconventional reservoirs. The workflow incorporates fracture propagation to model the injection phase using a 3D finite difference (FD) simulation and seamlessly transitions to FMM-Sim for the subsequent production phase modeling. A simplified physical model for pressure-dependent fracture dilation/compaction was proposed and parameterized to emulate fracture propagation. The model was validated with ABAQUS, a fully coupled fluid flow and geomechanics simulator. In the workflow, the fracture parameters such as fracture geometry and

---

* Part of this chapter is reprinted from Park, J., Iino, A., Datta-Gupta, A., Bi, J. and Sankaran, S., 2020c. Novel hybrid fast marching method-based simulation workflow for rapid history matching and completion design optimization of hydraulically fractured shale wells. Journal of Petroleum Science and Engineering, 196: 107718 with permission from Elsevier, whose permission is required for further use.

* Part of this chapter is reprinted from Park, J., Iino, A., Datta-Gupta, A., Bi, J. and Sankaran, S., 2019a. Rapid modeling of injection and production phases of hydraulically fractured shale wells using the fast marching method. Unconventional Resources Technology Conference (URTEC) with permission from URTeC, whose permission is required for further use.

permeability are obtained as a result of the injection phase modeling. Next, they are transferred into the subsequent production phase modeling with FMM-Sim which transforms 3D reservoir simulation model into 1D simulation model leading to orders of magnitude faster computation. The workflow was successfully applied to a field case in the Delaware Basin. The injection and production well data was first history-matched using a genetic algorithm. The calibrated models provide a range of estimated ultimate recovery (EUR) and net present value (NPV) of the history-matched well. After the history matching, the calibrated fracture dilation/compaction curves were used to investigate the optimum completion design for the well. The workflow has been proposed in practical and efficient way in the sense that the entire workflow, from the fracture propagation to the subsequent production, can be performed in any 3D FD simulator. This substantially saves computation resources and manpower compared to common industry workflows. The proposed workflow which connects completion design and hydrocarbon production with efficient computation would be beneficial for field development planning and economic decision making in unconventional reservoirs.

Introduction

As end of 2018, total liquids proved reserves in the United States reached 47.1 billion barrels and major shale plays accounted for almost half of it (EIA, 2019). About 6.5 million barrels per day of crude oil were produced directly from tight oil resources in the United States which was about 59% of total U.S crude oil production in 2018. The tight plays such as the Permian, the Eagle Ford, the Bakken and other formations, which are hydrocarbon-bearing formations with low permeability, must be hydraulically fractured in order to economically produce oil. To further maximize productivity of wells, the current industry practice involves horizontal drilling with multi-stage hydraulic fracturing, tighter cluster spacing, and large volume of fracturing fluid and proppant. This practice results in complex fracture geometry and flow pattern from the stimulated reservoir volume to a well. While empirical or analytical solutions such as decline curve analysis (DCA) or rate transient analysis (RTA) are frequently used to assess unconventional well performance because of their efficiency, the solutions might not be sufficient to reliably demonstrate such complexity(Cipolla et al., 2011; Kam et al., 2015; Park et al., 2020b). Physics-based reservoir simulation is still essential to better understand the complex dynamics of the stimulated unconventional reservoir (Cipolla, 2009). It is especially true when it comes to optimization problems in tight shale reservoir (Bansal et al., 2018; Chen et al., 2019; Liang et al., 2019; Park and Janova, 2019; Sen et al., 2018; Xiong et al., 2019; Zhu et al., 2017). However, the physics-based approach requires substantially more computation resources and manpower compared to DCA or RTA.

As an effort to mitigate such issues, previous studies proposed FMM-Sim, which transforms a 3D reservoir simulation model into an equivalent 1D simulation model using pressure propagation information. It has been used as a sophisticated proxy of the full 3D reservoir model and demonstrated its efficiency and accuracy in field-scale unconventional reservoir modeling (Iino et al., 2019; Iino et al., 2017a; Xie et al., 2015;

Xue et al., 2019a; Yang et al., 2017b; Zhang et al., 2016). It is based on a high frequency asymptotic solution which transforms the diffusivity equation to the Eikonal equation (Vasco et al., 2000; Vasco and Datta-Gupta, 2016). The Eikonal equation can be effectively solved using the Fast Marching Method (FMM) which is a one-pass algorithm tracking propagation of a front away from a source point (Sethian, 1996; Sethian, 1999). The solution of the equation yields the diffusive time of flight (DTOF). The DTOF is the generalized concept of radius of investigation (Datta-Gupta et al., 2011), and its application has been extended to flow diagnostic and production data analysis from unconventional reservoirs (Xue et al., 2018; Xue et al., 2019b; Yang et al., 2017a). The DTOF can be used as a spatial coordinate to transform a 3D model to an equivalent 1D model (Zhang et al., 2016). It allows us to significantly benefit in computation efficiency from simulating the equivalent 1D model instead of the original full 3D model, especially when the original model contains multiple hydraulic fractures with heterogeneous matrix. A body of previous studies successfully showed its application in fractured shale wells in unconventional reservoirs. However, fracture parameters such as fracture geometry and permeability in the previous studies were user-specified input for FMM-Sim. Therefore, it was difficult to dynamically link completion design parameters (e.g., fluid injection volume) to well performance after the model calibration. For example, Iino et al. (2017a) showed rapid history matching of a fractured shale well using FMM-Sim by calibrating fracture geometry and properties as history matching parameters. The history matching results and calibrated models helped understand reservoir dynamics and forecast the well performance. However, the history matching results cannot be applicable to assess well performance with different completion designs. The calibrated fracture parameters are only valid given the completion design. This issue can be resolved by incorporating forward modeling of hydraulic fractures in the workflow. Therefore, this study aims to extend the rapid simulation technique to injection phase of hydraulically fractured shale wells. This makes it efficiently assess completion design for unconventional field development planning and economic decision making on top of forecasting well performance through rapid history matching.

In order to incorporate fracture modeling in the workflow, pressure-dependent fracture properties were proposed and parameterized to demonstrate fracture compaction and dilation. The difference in this study compared to previous study which also tried to integrate permeability change of hydraulic/natural fractures as function of pressure into 3D FD simulation (Chipperfield et al., 2007; Ji et al., 2019; Ji et al., 2004; Min et al., 2018; Mittal et al., 2015; Sen et al., 2018) is that the shape of the curve is parameterized by introducing physical parameters. This allow us to calibrate the curve shape during the history matching and use it when different completion design and its impact on well performance are investigated after the calibration. The construction of the compaction and dilation curves is motivated and inspired by previous experiments (Bandis et al., 1983; Barton et al., 1985; Cho et al., 2012; Lee and Cho, 2002; Min et al., 2004; Tang et al., 2002; Wang and Park, 2002; Zhang et al., 2013) and numerical modeling (Dempsey et al., 2015; Pogacnik et al., 2016; Samnejad et al., 2017) of fracture property modification due to stress and pressure change in fractured or damaged rock mass. The validation of this empirical and simplified physics-based pressure-dependent curves for fracture dilation/compaction will be discussed later compared to a fully coupled fluid flow and geomechanics simulator, ABAQUS.

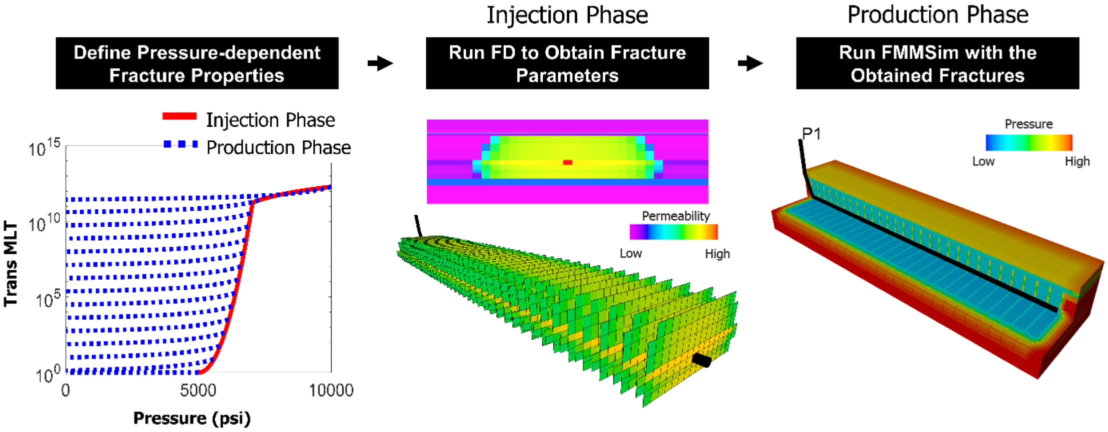

Figure 1. Schematics of hybrid FMM simulation workflow

Figure 1 illustrates the overall view of the hybrid FMM-Sim workflow. First, empirical and simplified physics-based pressure-dependent fracture property curves are defined. The way the curves are generated will be discussed in the methodology section in detail. Given the curves, the injection phase is simulated using FD to mimic fracture propagation. As a result, fracture parameters such as fracture geometry and permeability are obtained. Next, the workflow proceeds to running FMM-Sim for the subsequent production phase with the fracture parameters obtained in the previous injection phase. Thus, compared to previous hydraulically fractured unconventional reservoir studies with FMM-Sim, the injection phase modeling is included in the workflow to provide FMM-Sim with the fracture parameters as input. The main reason that injection phase is simulated in 3D FD, not FMM-Sim is that as fractures propagate, the permeability field changes so that the geometry of the DTOF also eventually changes. This requires the 1D simulation grid to be updated at major permeability changes to accurately capture pressure propagation front which compromises the efficiency of FMM-Sim. After the methodology is introduced and validated with ABAQUS, the field application of the proposed workflow to a field case in the Delaware Basin will be presented. The reservoir model was first history-matched using a population-based evolutionary algorithm. After history matching, the calibrated parameters were used to investigate different completion designs and their impact on cumulative oil production and NPV. It should be emphasized that the workflow is a simulator-independent and the entire workflow, from fracture propagation to subsequent production, can be performed in a single simulator. This avoids the additional effort in common industry workflows where hydraulic fracture is simulated in a stand-alone tool and consequent fracture parameters are transferred to flow simulators. This further adds efficiency in the workflow combining with FMM-Sim.

Methodology

The Fast Marching Method-based Flow Simulation

The underlying idea of the FMM-Sim is to utilize the DTOF as the 1D spatial coordinate, which embeds reservoir heterogeneity of in the original 3D space, transforming a 3D flow simulation into an equivalent 1D flow simulation. High frequency asymptotic solution leads the diffusivity equation to the Eikonal equation (Vasco et al., 2000; Vasco and Datta-Gupta, 2016),

$$\left|\nabla \tau(\mathbf{x})\right| = \frac{1}{\sqrt{\alpha(\mathbf{x})}}, \tag{1}$$

where τ is the DTOF and $\alpha(\mathbf{x})$ is the diffusivity at a location $\mathbf{x}$. In a multi-phase flow system, the diffusivity at the location $\mathbf{x}$ is defined as

$$\alpha(\mathbf{x}) = \frac{\lambda_t(\mathbf{x})k(\mathbf{x})}{\phi(\mathbf{x})c_t(\mathbf{x})}, \tag{2}$$

where $\phi(\mathbf{x})$ is the porosity, $k(\mathbf{x})$ is the permeability, $\lambda_t(\mathbf{x})$ is the total mobility, and $c_t(\mathbf{x})$ is the total compressibility at the location $\mathbf{x}$.

The Eikonal equation is the generalization of the concept of radius of investigation (Lee, 1982) to heterogeneous, anisotropic, and fractured geologic medium (Datta-Gupta et al., 2011). Given the pressure propagation velocity, which is the square root of the diffusivity, the DTOF represents the travel time of ‘peak’ pressure response from an impulse source or sink (Figure 2).

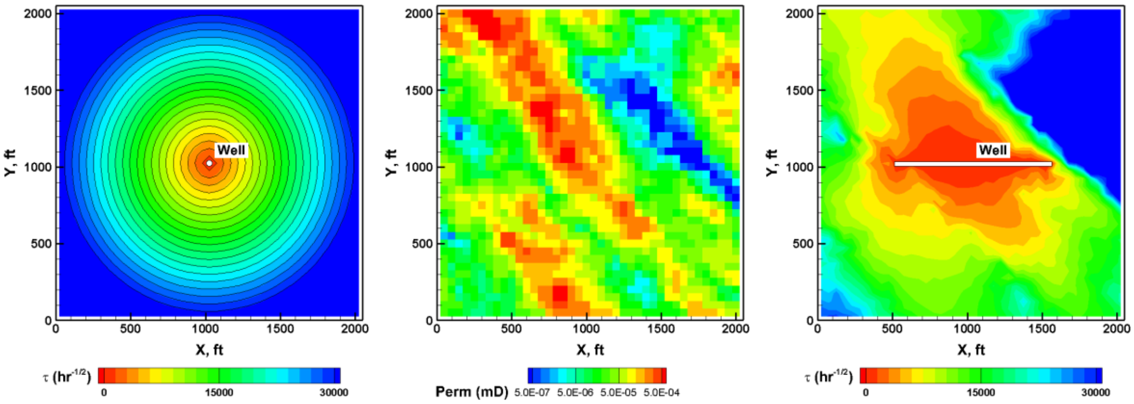

(a) (b) (c)

Figure 2. (a) The DTOF from a vertical well in homogenous reservoir, (b) a reservoir with heterogeneous reservoir and (c) the DTOF from a horizontal well in the heterogeneous reservoir (modified from Iino et al. (2017a))

Given the diffusivity of a reservoir, the Eikonal equation can be efficiently solved for the DTOF by using the FMM which is a one-pass algorithm tracking the propagation of a front away from a source point (Sethian, 1996; Sethian, 1999). Xie et al. (2015) showed the implementation of FMM algorithm in the Cartesian grid system and recently its implementation has been extended to various types of grid system such as unstructured grids (Yang et al., 2017c), embedded discrete fracture models (EDFM), and local grid refinements (LGR) (Xue et al., 2019a).

In order to transform a 3D simulation model into an equivalent 1D simulation model, the diffusivity equation needs to be reformulated. By assuming that the pressure propagation contour is aligned with the DTOF contour and introducing $w(\tau)$, which is the derivative of drainage volume with respect to the DTOF,

$$w(\tau)=\frac{dV_p(\tau)}{d\tau}, \tag{3}$$

where $V_p(\tau)$ is the drainage volume and the 3D diffusivity equation is now reduced in the 1D DTOF coordinate (Yang et al., 2017a; Zhang et al., 2016)

$$\frac{\partial}{\partial \tau}\left[w(\tau)\frac{\partial p}{\partial \tau}\right]=w(\tau)\frac{\partial p}{\partial t}. \tag{4}$$

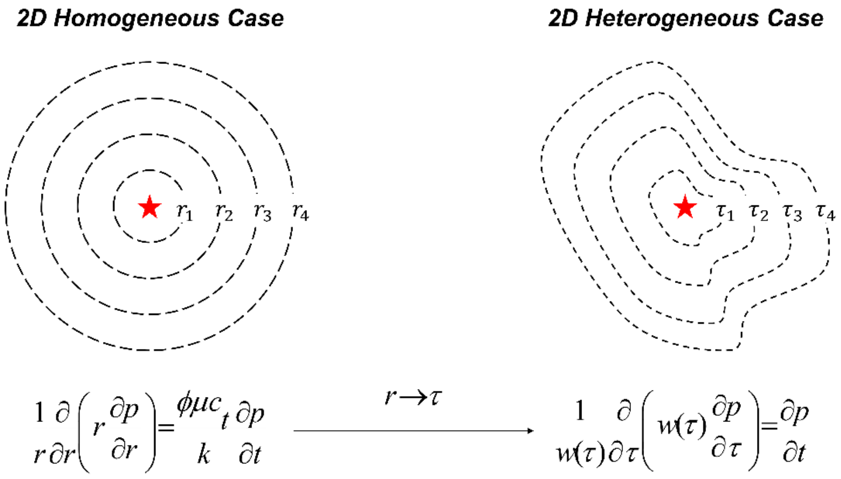

Figure 3. Analogy between a radial coordinate in a homogenous reservoir (left) and DTOF as a spatial coordinate in a heterogeneous reservoir (right) (modified from Yang et al. (2017a))

Figure 3 shows an analogy between the familiar radial coordinate and the DTOF as a spatial coordinate. The DTOF can resolve pressure front information in 2D space and express the governing equation solely in terms of DTOF and t, as the radial coordinate can do with r and t. However, the DTOF coordinate can embed the spatial heterogeneity. Given the reformulated equation, the 3D reservoir model can be transformed into an equivalent 1D simulation model. The core of FMM-Sim process is to reformatting 3D reservoir model into an equivalent 1D model in a standard FD simulator input format with a series of pore volume and transmissibility of 1D cells.

As illustrated in Figure 4, the FMM-Sim involves multiple steps. First, multi-phase diffusivity of each grid block in the 3D model is computed. Given the diffusivity, the Eikonal equation is solved by using FMM to obtain the DTOF starting from the source to each grid cell. Next, the pore-volume is accumulated with respect to the DTOF and discretized on the DTOF coordinate. From the discretization, $w(\tau)$ is obtained and the number of discretization is corresponding to the number of grid cells in the 1D simulation model. Therefore, the discretized pore-volume corresponds to the pore-volume of each grid in the 1D simulation model and the $w(\tau)$ is used for transmissibility and well index calculation for the 1D simulation model. Finally, the 1D simulation model is written in a standard FD simulation format with a series of pore-volume and transmissibility such that the 1D model can be simulated in any kind of FD simulator. Because the FMM-Sim reduces the 3D simulation model to an equivalent 1D simulation model, it results in significant benefit in computation efficiency leading to orders of magnitude faster computation compared to the 3D FD simulation (Iino et al., 2017a). The benefit is even more substantial when it comes to compositional modeling (Iino et al., 2019; Iino et al., 2017b).

In this study, FMM-Sim is used for production phase modeling as a sophisticated proxy of full 3D simulations, which has demonstrated its efficiency and accuracy in the previous studies. Combining with fracture propagation in FD simulation using pressure-dependent fracture property curves, FMM-Sim maximizes the efficiency in the workflow.

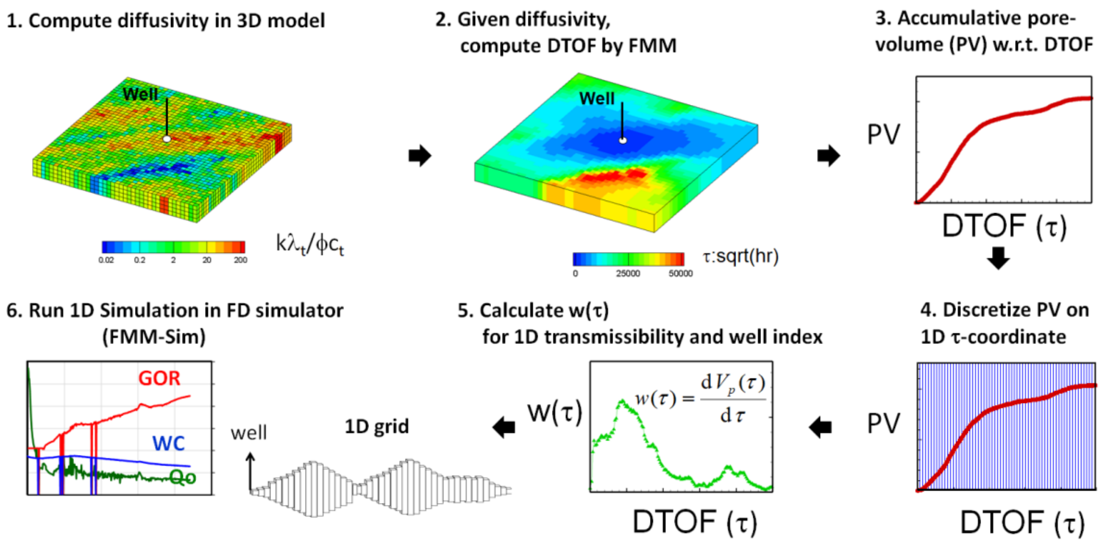

Figure 4. Steps of FMM-based flow simulation (modified from Iino et al. (2017a))

Pressure-dependent Compaction and Dilation Curves for Hydraulic Fractures

The fundamental underlying assumption in the dilation/compaction curve generation is that the total stress does not vary with time. Therefore, changes in fracture permeability and porosity can be simply expressed as function of pressure. In order to mimic geomechanical behavior of the fracture properties, transmissibility and pore-volume multiplier curves are assigned to predefined fracture propagation paths (Figure 5). Thus, fracture opening and closure are determined by pressure at grid cells along the predefined fracture paths. In the current study, all hydraulic fractures are assumed to be planar. However, incorporating natural fractures in reservoir models, the method can be easily extended to complex non-planar fracture networks.

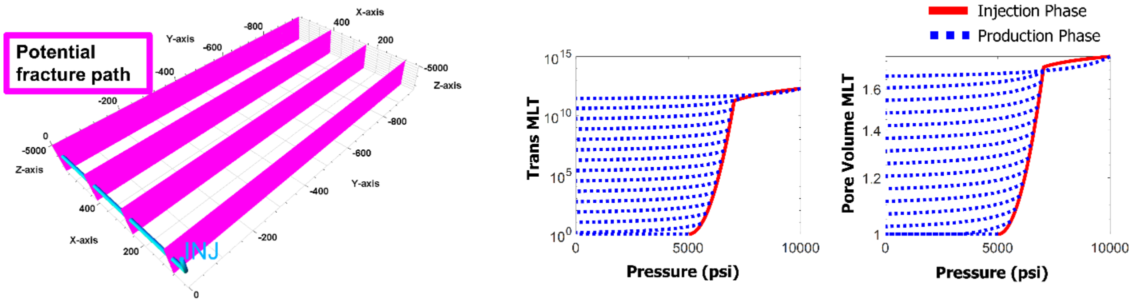

Figure 5. Schematics of potential fracture propagation path (left) and transmissibility and pore-volume multiplier curves (center and right). The red lines are for injection phase (i.e., dilation) and the blue lines are for production phase (i.e., compaction).

The transmissibility enhancement during injection phase is modeled by adopting implicit fracture width. The implicit fracture width varies with respect to pressure at a grid cell. The calculated implicit fracture width is a stepping stone to obtain an equivalent permeability for flow simulation (Park and Kim, 2016) by using the cubic law, the solution of Navier-Stokes equation for fluid flow between two smooth parallel walls (Witherspoon et al., 1980; Zimmerman and Yeo, 2000). The variation in pore-volume follows an empirical correlation between permeability and porosity obtained from experiments on sedimentary rocks (Davies and Davies, 1999). The following section discusses step-wise curve generation and its parameterization.

The injection phase transmissibility multiplier curve is generated with six parameters. The fracture initiation pressure, p_{fi}, is the pressure necessary to initiate a fracture. The initial fracture width, w_{ini}, is the fracture width at the fracture initiation pressure. We also need Young's modulus (E), Poisson's ratio (ν), initial reservoir pressure (p_{ini}), and matrix permeability (k_{mat}) to generate the complete curve. However, in this study, the last four parameters are known in the model calibration and history matching process. Therefore, only first two parameters, p_{fi} and w_{ini}, are utilized to calibrate models.

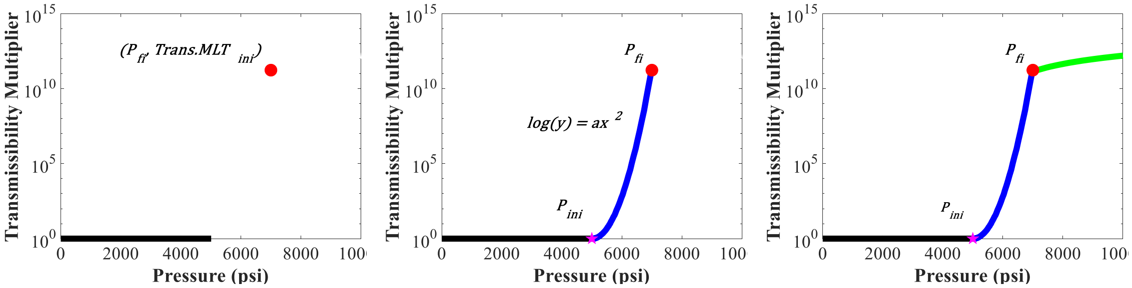

(a) (b) (c)

Figure 6. Step-wise injection phase transmissibility multiplier curve generation

The step-wise curve generation is illustrated in Figure 6. First, the fracture initiation pressure, p_{fi}, and the initial fracture width, w_{ini}, are assigned. Given the fracture width, the transmissibility multiplier for the fracture is computed by cubic law (Witherspoon et al., 1980; Zimmerman and Yeo, 2000)

$$Trans.MLT_{ini} = \frac{w_{ini}^2}{12} / k_{mat}, \tag{5}$$

so that the red dot in Figure 6(a) is determined as (p_{fi}, $Trans.MLT_{ini}$). Next, the curve is assumed to follow a log-quadratic behavior from the initial reservoir pressure, p_{ini}, to the fracture initiation pressure,

$$\log\left(Trans.MLT\right) = \alpha\left(p - p_{ini}\right)^2, \tag{6}$$

which is highlighted by the blue curve in Figure 6(b). The quadratic behavior assumption is motivated by laboratory and numerical experiments on permeability change with respect to stress, strain and displacement (Dempsey et al., 2015; Lee and Cho, 2002; Min et al., 2004; Pogacnik et al., 2016; Tang et al., 2002; Wang and Park, 2002; Zhang et al., 2013). Finally, after the fracture initiation pressure, the curve follows linear elastic fracture mechanics (Figure 6(c)). The assumptions including plain strain and fixed fracture height (Gidley, 1989) lead the Sneddon solution for classic crack problem (Sneddon and Elliot, 1946) to a PKN-type equation (Economides and Nolte, 1989; Nordgren, 1972; Perkins and Kern, 1961). Therefore, the fracture width is now calculated by

$$w = w_{ini} + \frac{2\left(1-v^2\right)h_f}{E}\left(p - p_{fi}\right), \tag{7}$$

where h_f is the fracture height. Given the fracture width, the corresponding transmissibility multiplier for the fracture can be again calculated by using Equation (5).

Mechanistic description of the dilation curve can be sought by comparing the dilation curve parameters with parameters in a fully-coupled fluid flow and geomechanical simulator. The detailed description of hydraulic fracture propagation modeling in ABAQUS is discussed in the next section. However, here one simple and intuitive comparison is presented between the effective horizontal stress in ABAQUS and the fracture initiation pressure in the dilation curve. Figure 7(b) shows that the increase in effective minimum horizontal stress, $\sigma_h^{'}$, induces the increase in the fracture propagation pressure in ABAQUS model. This is because $\sigma_h^{'}$ acts as the closure pressure of the fracture so that the fracture needs to be pressurized more to initiate the fracture at the tip and maintain fracture propagation. Similarly, the increase in p_{fi}, the fracture initiation pressure, reflects in the fracture propagation pressure. The comparison shows that the proposed parameter in the curve generation not only parameterizes the shape of the curve but also conveys physical meaning.

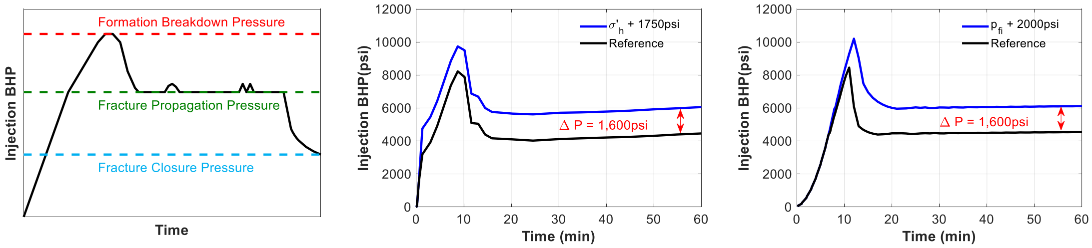

(a) (b) (c)

Figure 7. (a) Schematic of injection BHP response during hydraulic fracturing (modified from (Zoback, 2010)), BHP response in (b) ABAQUS and (c) FD simulator

In the production phase, the Barton-Bandis model is used to describe pressure-dependent fracture conductivity reduction. The original paper (Barton et al., 1985) describes that the fracture permeability reduction converges to a single residual fracture permeability value. In this study, the original equation is modified such that the reduction paths in the fracture permeability depend on retained permeability after stimulation (Chipperfield et al., 2007; Ghanizadeh* et al., 2016; Keshavarz et al., 2015; Keshavarz et al., 2014). Therefore, the multipliers decrease proportionally preserving the enhancement from the prior injection phase during the compaction. The equation is modified from the original equation as follows (see the Appendix),

$$Trans.MLT = \left(1 - \frac{\sigma_n^{'}\left(1-k_{rf}^{\;0.25}\right)}{K_n\left(w_{ini}\times\left(1-k_{rf}^{0.25}\right)\right)+\sigma_n^{'}}\right)^4, \tag{8}$$

where $\sigma_h^{'}$ is the effective normal stress whose change is simply pressure change in this case, k_{rf} is the fracture residual permeability ratio, and K_n is the fracture stiffness.

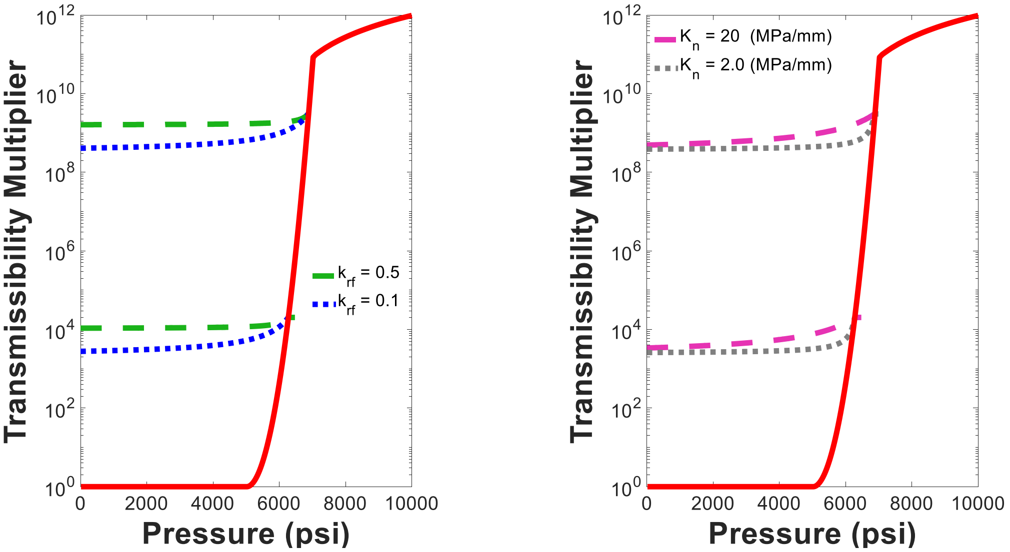

(a) (b)

Figure 8. Compaction behaviors with different parameters: (a) fracture residual permeability ratio with 10MPa/mm of K_n and 0.001m of w_{ini} (b) fracture stiffness with 0.1 of k_{rf} and 0.001m of w_{ini}

Figure 8 illustrates the impact of these parameters on compaction behavior. The residual permeability ratio controls the point that the transmissibility multipliers converge to (Figure 8(a)). The fracture stiffness controls how fast the multiplier approaches to the convergence point (Figure 8(b)). Therefore, the model governs the compaction behavior by controlling the convergence point and the degree of approaching.

For the pore-volume multiplier curve, an empirical relationship between enhanced permeability and porosity is referred. It was first introduced by Davies and Davies (1999) based on their experimental study on sedimentary rocks. Later, it has been modified by other researchers (Rutqvist and Tsang, 2002; Winterfeld and Wu, 2011; Wu et al., 2014a; Wu et al., 2014b) to bring the correlation into numerical simulations in a form of the following equation,

$$PV.MLT = \left(\frac{1}{c_{pp}} \times \ln\left(Trans.MLT\right) + 1 \right). \tag{9}$$

The correlation tells the pore-volume multiplier, $PV.MLT$, has a log-linear relationship with the transmissibility multiplier, $Trans.MLT$, and the porosity-permeability coefficient, c_{pp}, is the coefficient in front of log $Trans.MLT$ term. The value of c_{pp} depends on the rock type (Davies and Davies, 1999).

Methodology Validation Using ABAQUS

ABAQUS simulates fully-coupled fluid flow and mechanical problems in the finite element (FE) discretization scheme. The goal of the validation is to capture mechanisms in fully-coupled ABAQUS fracture model with the proposed method by calibrating 3D FD flow simulation model. We utilized the cohesive zone model (CZM) in ABAQUS to model fracture propagation. The cohesive zone is a thin layer embedded between continuum elements to demonstrate cohesive force at the interference of elements. There are two main reasons that we decided to validate the proposed method with CZM. Firstly, CZM has been widely used to model fracture propagation of hydraulically fractured shale reservoirs (Chen et al., 2017; Gonzalez-Chavez et al., 2015; Haddad et al., 2017; Haddad and Sepehrnoori, 2014; Huang et al., 2017; Huang et al., 2016; Shin and Sharma, 2014; Wang et al., 2016; Zhang et al., 2010). This is primarily because it accounts for the fracture process zone, the area ahead of fracture tip, and the softening effect which are important to accurately predict the behavior of ductile and quasi-brittle rocks like shale. Secondly, CZM resembles our method in the sense that cohesive zone should be defined before fracture propagation simulations. The fractures only propagate along the predefined cohesive zone. The constitutive behavior of the cohesive zone follows the traction-separation law. As continuum elements separates, the traction of the interface between the elements first increases (damage initiation). After the traction limit, the traction starts decreasing (damage evolution) until the complete separation (see Yao (2012)).

Table 1. Input parameters for the ABAQUS reference case

Parameters	Value	Unit
Initial reservoir pressure	4,850	psi
Overburden stress	11,000	psi
Maximum horizontal stress	8,300	psi
Minimum horizontal stress	7,900	psi
Bottom-hole pressure for production	3,000	psi
Total compressibility	3.6E-6	psi^{-1}
Porosity	0.043	
Reservoir permeability	100	nd
Young's modulus	2.56E6	psi
Poisson's ratio	0.25	
Fracture toughness	2000	$psi \times in^{1/2}$
Leakoff Coefficient	1E-6	ft/(psi×s)

The benchmark ABAQUS model is a single-phase flow system. It has four fractures with 165ft spacing and all the fractures are assumed to be planar. The simulation domain size is 660ft in x-direction, 1,000ft in y-direction and the thickness of the domain is 100ft. The normal faulting stress regime is imposed in the model such that the fracture propagates in y-axis which is the maximum horizontal stress direction (Figure 9(a)). Other necessary parameters for the benchmark case is summarized in Table 1. The cohesive element parameters are assigned based on the CZM simulation guideline (Saad, 2013). The simulation is constrained by injection rate which increases until 10 minutes and is maintained at 18.5bpm afterward. As a response, the BHP increases until 10 minutes of the injection and then drops after the breakdown pressure. The subsequent production simulation is performed with a constant 3000psi BHP for the following 1000 days incorporating viscoelastic elements inside the cohesive elements to demonstrate proppants (Huang et al., 2017; Huang et al., 2016). Therefore, in the production phase, the fracture opening depends on time and stress imposed on the proppant elements as the reservoir is depleted.

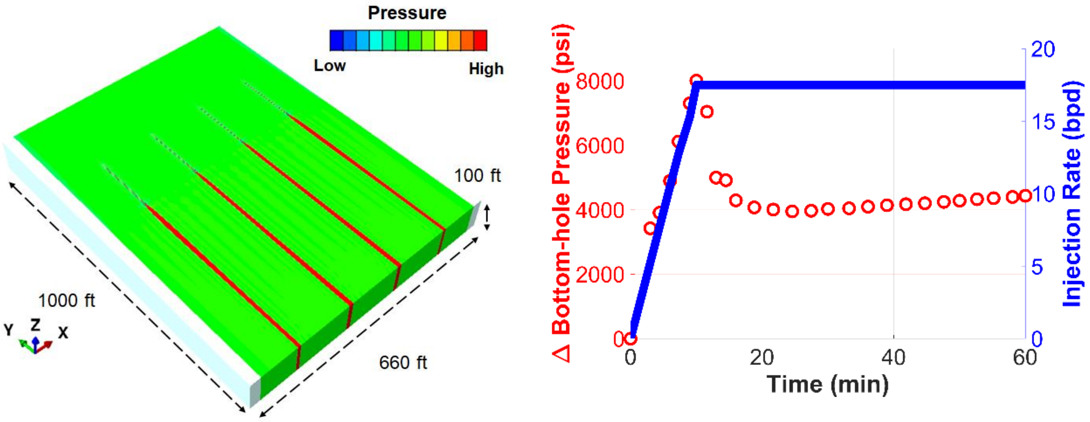

(a) (b)

Figure 9. ABAQUS fracture propagation model for model calibration reference

Figure 10 shows the Eclipse (3D FD) model used for the calibration. The Eclipse model has the same geometry as the ABAQUS model. The tartan gridding is utilized to describe hydraulic fractures and surrounding area. It should be noted that completion cells in the model are initially assigned with high permeability and porosity to enable initial fluid injection avoiding numerical instability. Also, the permeability and porosity of the completion cells are going to be adjusted using multipliers during the calibration process in order to match injection BHP response.

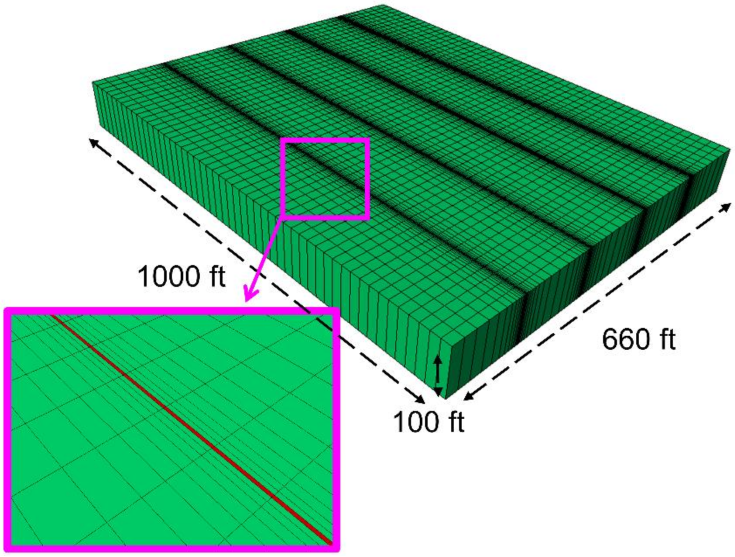

Figure 10. Eclipse model used for the calibration

The detailed the model calibration method is listed in Table 2. The model calibration is performed using Matlab-based in-house genetic algorithm program. It is one of the evolutionary algorithms, imitating “Survival of the fittest”. The algorithm begins with populations of sampled parameters from predefined parameter ranges. In each generation, the algorithm stochastically chooses multiple models based on their fitness. Next, new populations for the next generation are created by mutation and crossover of the selected populations. During the calibration, the well is constrained with rates and BHP for injection and production phases, respectively. The goal of the calibration is to minimize misfit in injection BHP and cumulative water production between the ABAQUS and the 3D FD simulation results.

Table 2. Calibration methodology for the validation

Calibration Algorithm	Genetic algorithm (100 population/generation, total 10 generation)	
Well Constraints	Injection: pump rate	Production: bottom-hole pressure
Calibration Period	Injection: 60 minutes	Production: 1000 days
Objective Function	$f(\mathbf{m}) = \sum_{i}^{Inj\_steps}\left[\ln\left|\Delta inj\_BHP\right|_i\right] + \sum_{j}^{Prd\_steps}\left[\ln\left|\Delta Cum.wat\right|_j\right]$	

Figure 11 shows a schematic of the calibration process. First, parameters listed in Table 3 are stochastically sampled from the predefined ranges using Latin hypercube sampling method. Given the parameters, multiplier curves are generated and prepared as a format of simulation input so that simulations can read and use the pressure-dependent fracture property information. Specifically, the keyword *ROCKTAB* is used for Eclipse simulation. Next, the injection phase is simulated with injection rate constraint. As a result, hydraulic fracture parameters such as fracture geometry and permeability are obtained. The subsequent production phase is simulated with the fracture parameters transferred from the previous injection phase. Finally, the misfit between the ABAQUS and Eclipse simulation results is evaluated. This procedure is iterative toward minimizing the misfit until a satisfactory quality of history matching result is achieved or the number of generations reaches to its maximum.

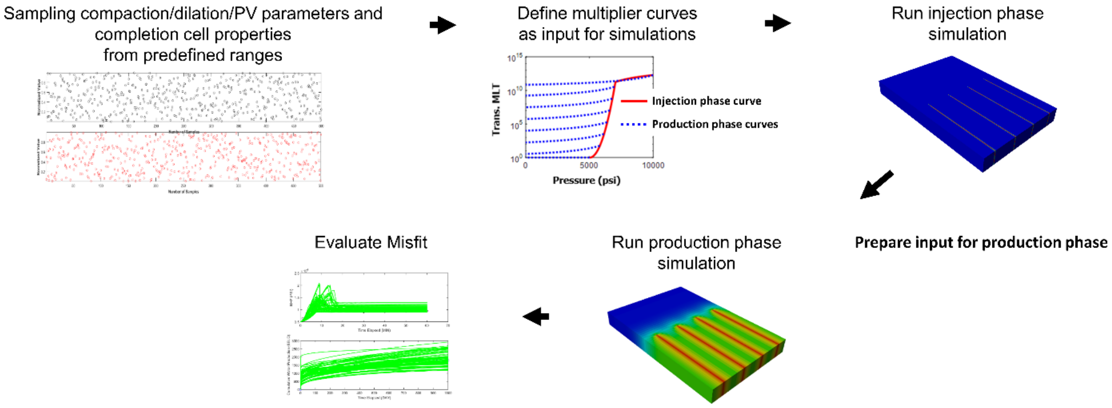

Figure 11. Schematics of the calibration process for the validation

Table 3. Calibration parameters and parameters' range for Eclipse FD simulation

Category	Parameter	Description	Low	Base	High
Dilation/Compaction Parameters	p_{fi} (psi)	Fracture initiation pressure	5.0e+3	6.0e+3	7.0e+3
	w_{ini} (m)	Initial fracture width	5.0e-3	1.0e-2	5.0e-2
	K_n (MPa/mm)	Fracture stiffness	5.0e-1	1.0e+1	3.0e+1
	k_{rf}	Fracture residual permeability ratio	1.0e-4	1.0e-1	8.0e-1
	c_{pp}	Porosity-permeability coefficient	30.0	60.0	80.0
Completion Cell Properties	$MULTPV$	PV multiplier	1.0e+0	5.0e+0	1.0e+1
	$MULTX$	Transmissibility multiplier	1.0e+0	2.0e+0	3.0e+0

The calibration results are presented in Figure 12. Figure 12(a) shows that the global misfit gradually decreases as the algorithm evolves with the number of generations. Updated models (magenta circles) which have lower misfit than the threshold (red dotted-line) were selected to compare with the initial population (Figure 12(a)). The updated models show substantial improvement and good agreement in both injection BHP (Figure 12(b)-(c)) and cumulative water production (Figure 12(d)-(e)) after the calibration.

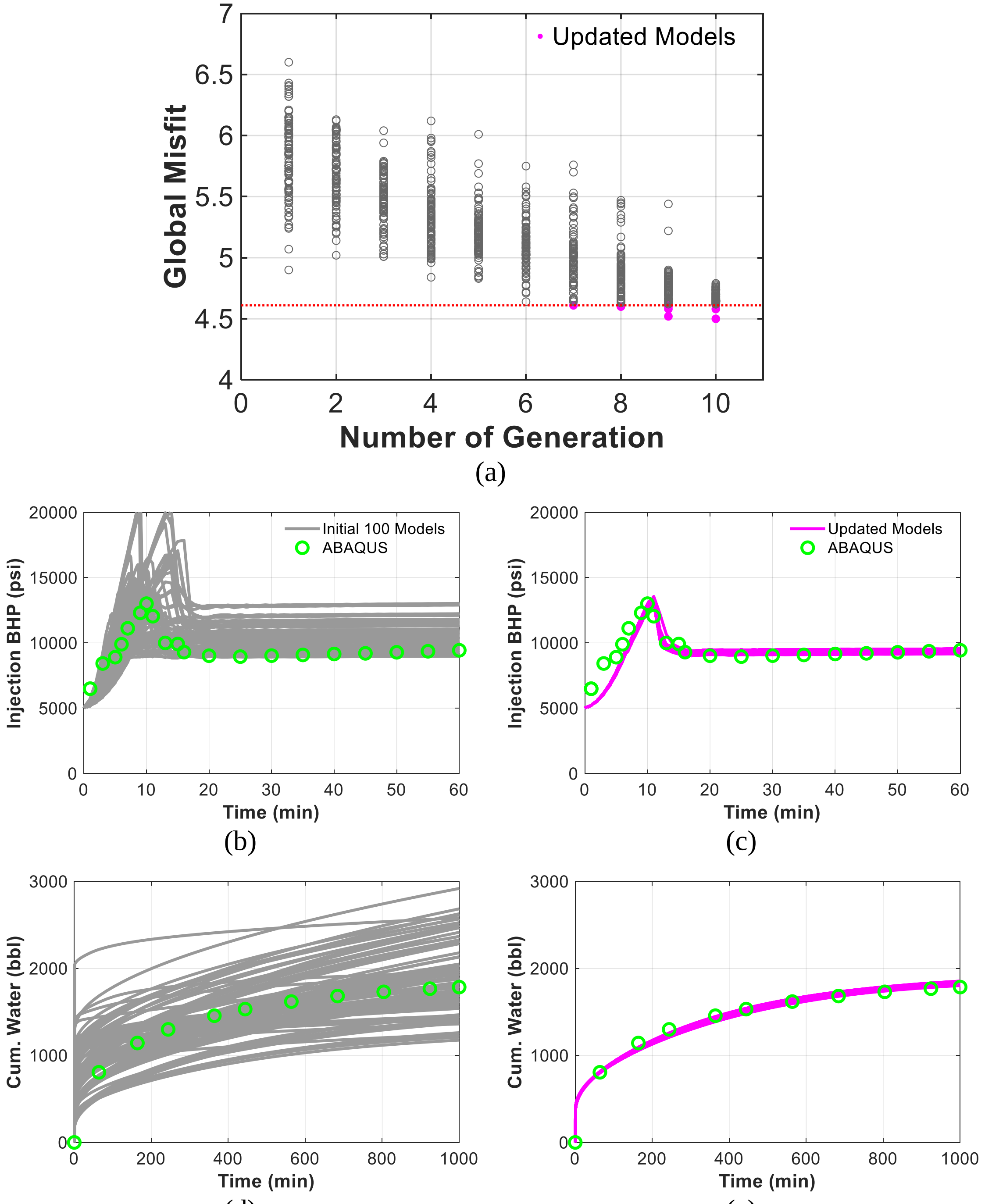

(a)

(b) (c)

(d) (e)

Figure 12. Calibration results for validation with ABAQUS: (a) global misfit vs. the number of generation, initial 100 models vs. ABAQUS (b) injection BHP and (d) cumulative water production, updated models vs. ABAQUS (d) injection BHP and (e) cumulative water production

To compare fracture geometry and BHP between ABAQUS and 3D FD in detail, one of the history-matched models is selected. In ABAQUS, the fracture opening is directly measured from the cohesive elements (Figure 13(a)). However, 3D FD does not explicitly calculate fracture opening of grid cells. Therefore, the square root of fracture permeability for the Eclipse model which is an equivalent quantity to fracture opening is presented (Figure 13(b)). Figure 13(c) shows the BHP comparison between two models. The 3D FD well captures the trend from ABAQUS model such as pressure build-up followed by breakdown pressure and fracture propagating pressure. From the detailed comparison, we can see that 3D FD results with the proposed pressure-dependent fracture properties model well emulates the fully-coupled fluid flow and geomechanical simulation results. More importantly, 3D FD simulation is highly efficient compared to ABAQUS simulation. The computation time for one 3D FD simulation run is around 20 seconds while one ABAQUS simulation takes around 1140 seconds. Thus, empirical fracture compaction/dilation model incorporated in 3D FD not only captures the fracture propagation mechanisms in ABAQUS but also provides efficient computation. This makes the proposed methodology well fitted to field applications as a good proxy of the fully-coupled fluid flow and geomechanical simulator.

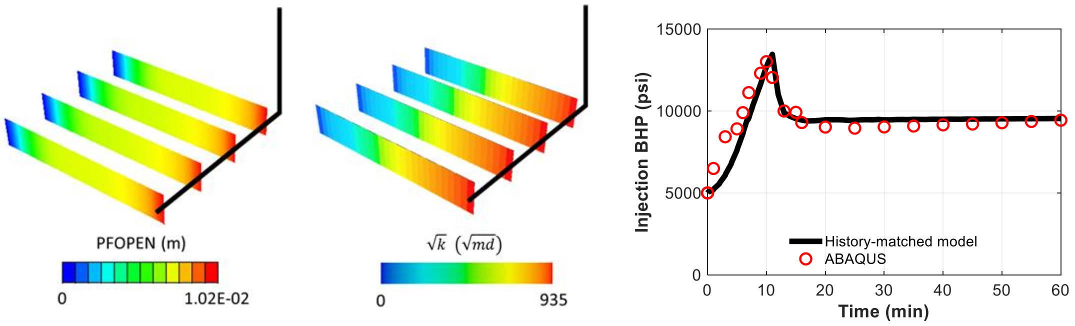

(a) (b) (c)

Figure 13. Detailed fracture geometry and BHP comparison: (a) ABAQUS fracture geometry, (b) 3D FD fracture geometry, (c) BHP comparison between two models

Field Application: History Matching and Completion Design Optimization

For the field application, the novel hybrid FMM-Sim workflow with empirical fracture compaction/dilation model is applied to history matching and completion design optimization. In the workflow, the injection phase is modeled in 3D FD simulation and the results from the injection phase modeling such as fracture geometry and properties are transferred to the subsequent production phase modeling. Next, the production phase is simulated with FMM-Sim which transforms a 3D simulation model into an equivalent 1D simulation model using the DTOF for efficient computation.

The reason of employing a hybrid FMM-Sim workflow, rather than extending FMM-Sim to the injection phase modeling, is that FMM-Sim is not well-suited for modeling flow simulation during fracture propagation. FMM-Sim constructs the 1D model based on the DTOF which is the solution of the Eikonal Equation. The underlying assumption is that the DTOF does not change much over time so that the constructed 1D model remains equivalent to the 3D model throughout the simulation. However, as fracture propagates in the injection phase modeling, the permeability field significantly changes, leading to the large variation in diffusivity term in the Eikonal equation. This means that in order to accurately capture the DTOF, we need to solve the Eikonal equation and update the equivalent 1D model accordingly at every significant permeability change. This compromises the efficiency of the original FMM-Sim workflow where we construct the 1D model once and use it throughout the simulation. Therefore, in the novel hybrid FMM workflow, we use 3D FD simulation to capture the fracture propagation in injection phase modeling. Next, the workflow seamlessly transitions to FMM-Sim for the production phase modeling. The detailed procedure will be discussed after the field history data and reservoir simulation model are reviewed.

Figure 14 shows field history data. For injection phase, the average BHP and pump rate were provided by the operator. The fluid injection lasted for 100 minutes and the breakdown pressure was observed at 15 minutes after the injection began. During the fracture propagation, injection BHP landed around 11,000psi and the pump rate was maintained at 65bpm. For production phase, smooth decline of production BHP was observed. Notable observations in the well production data include that Gas Oil Ratio (GOR) was recorded to be flat during history period implying that the reservoir remained under-saturated. The water cut trend also stayed constant except for initial stimulation water production.

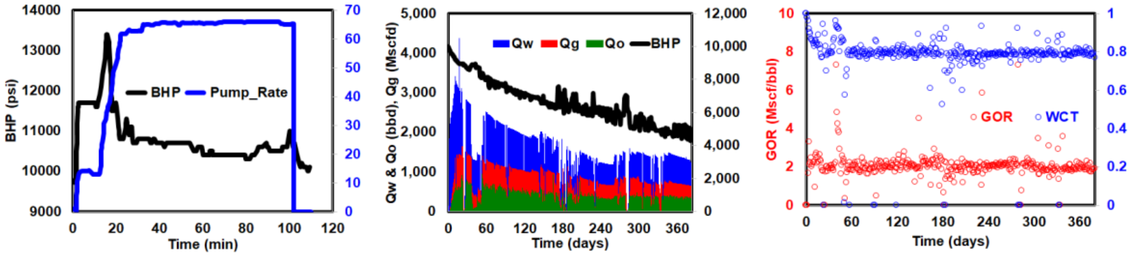

(a) (b) (c)

Figure 14. Field history data: (a) Injection BHP and pump rate, (b) production rates and production BHP, (c) GOR and water cut

The 3D reservoir simulation model used for the field application is presented in Figure 15. The reservoir is initially under-saturated. The initial reservoir pressure ranges between 9,000 – 9,500psi and the bubble point pressure is 3,950psi. The size of the model is 1,500ft in i-direction, 5,500ft in j-direction, and 465ft in k-direction and it comprises 0.4 million grid blocks (31×963×13 in i,j,k). The well has 28 stages and each stage has 5 clusters adding up 140 fractures in total. In order to describe hydraulic fractures, tartan gridding is utilized. The detailed configuration of the model around hydraulic fractures is shown in Figure 15. The red area represents the hydraulic fractures and cyan area represents the matrix. The matrix and the hydraulic fractures have different type of relative permeability curves. The relative permeability for the matrix follows Brooks-Corey type curve while straight lines are assigned to the hydraulic fractures based on Pieters and Graves (1994).

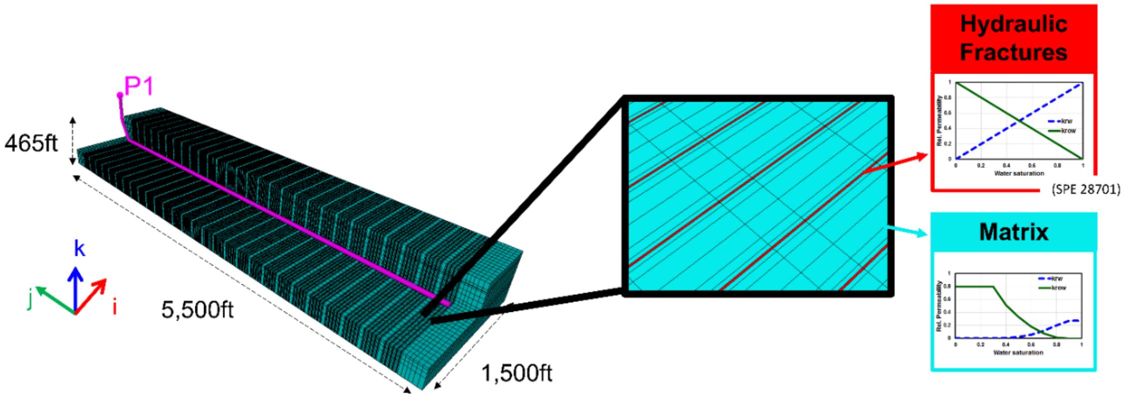

Figure 15. Reservoir simulation model for history matching

Figure 16 shows variations of properties in the reservoir simulation model along the depth where the dots indicate the boundary of layers. It is a layer-cake model which comprises three different zones. The target formation is Zone 2 and the well is perforated at lower Zone 2 which shows relatively high porosity and permeability with low water saturation.

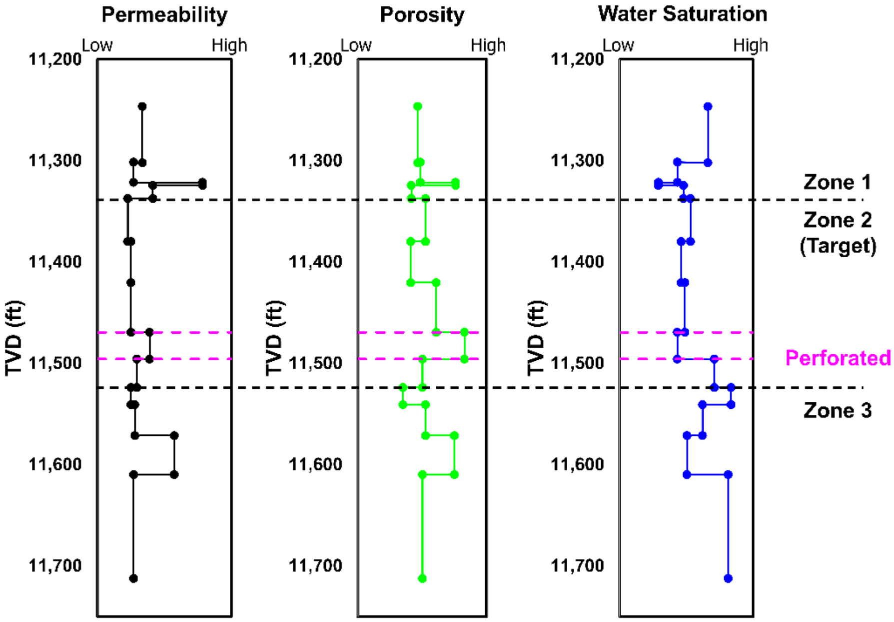

Figure 16. Variations of permeability (left), porosity (center), and water saturation (right) along depth

The detailed procedure for the field application is illustrated in Figure 17. The hybrid FMM simulation consist of two series of simulations: injection and production phase simulations. The injection phase is simulated in one-stage size of sector model using 3D FD providing fracture parameters such as fracture geometry and permeability. Next, conditions at the end of injection phase modeling including permeability, porosity, pressure and saturation distributions are transferred to the entire model as restart parameters. Therefore, for the subsequent, FMM-Sim can take on a simulation from at the end of injection phase modeling. Since both injection phase modeling and reconstructed 1D model simulation in FMM-Sim are performed in a FD simulator, the transition is seamless between injection and production phases without any additional effort such as reformatting or interpolation.

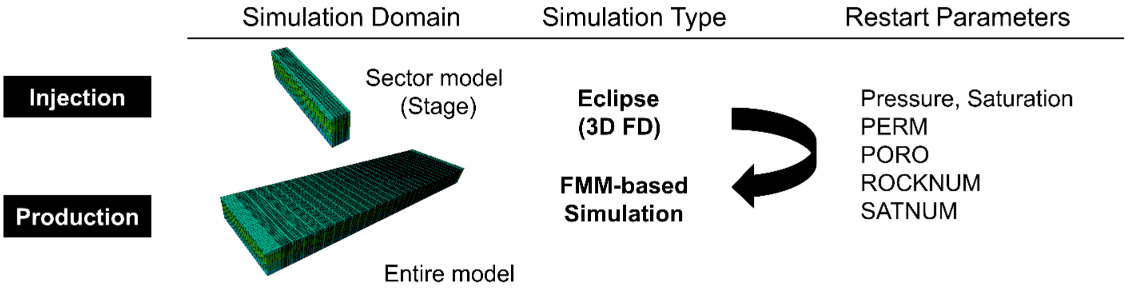

Figure 17. Hybrid FMM simulation procedure for the field application

Before moving forward, the results from 3D FD and FMM-Sim are compared in a single stage model to ensure FMM-Sim is a sophisticated proxy of a full 3D model (Figure 18). With liquid constraints, production BHP and water rate show good agreement between 3D FD and FMM-Sim. However, since FMM-Sim simulates an equivalent 1D model, it is much faster than the 3D FD simulation. For example, it takes about 870 seconds to run the entire model in 3D FD simulation whereas FMM-Sim only takes around 10 seconds. Therefore, FMM-Sim can be considered as sophisticated proxy model of full 3D model with high accuracy and efficiency which makes a good fit for field applications.

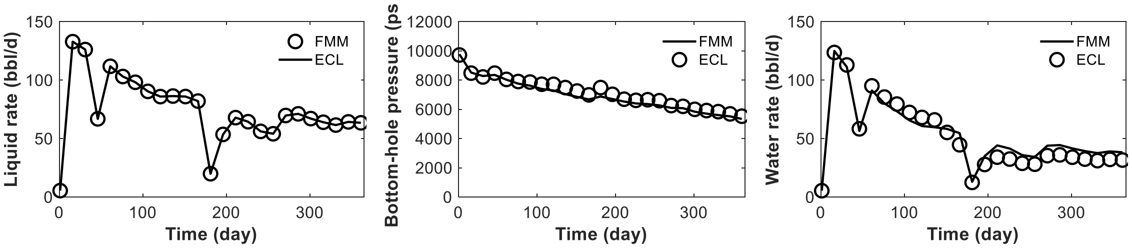

(a) (b) (c)

Figure 18. Comparison between Eclipse and FMM-based flow simulations in a single stage model: (a) liquid rate which is well constraints, (b) production BHP (c) water production rate

Table 4 presents a list of history matching parameters and their ranges. The history matching parameters are associated with dilation/compaction curves, completion cell properties, matrix permeability anisotropy and relative permeability. It should be emphasized that fracture parameters such as fracture geometry and permeability are not included in the table. This is because the fracture parameters are determined by the injection phase modeling and transferred to the subsequent production phase modeling in this workflow. The workflow does not directly manage fracture geometry and permeability. Rather, the workflow tunes dilation/compaction curve parameters to control fracture geometry and permeability during history matching such that the calibrated dilation/compaction curves can be used to investigate the impact of completion design (e.g., fluid injection volume) on production profiles.

illustrates parameters associated with the shape of dilation/compaction curves and relative permeability. Young's modulus and Poisson's ratio which are input to generate the dilation curve are assumed to be 5.6×10^6psi and 0.2, respectively (Kozlowski et al., 2018; Parker et al., 2015).

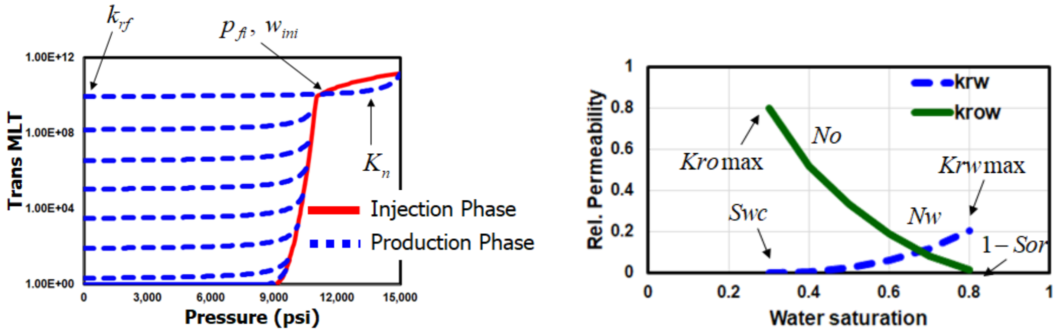

(a) (b)

Figure 19. History matching parameters related to (a)dilation/compaction curves and (b)relative permeability curves

Table 4. History matching parameters and parameters' ranges

Category	Uncertain Parameters	Low	Base	High
Dilation/Compaction Parameters	p_{fi}	1,500	2,000	3,500
	w_{ini}	0.001	0.025	0.1
	K_n	0.1	10	20
	k_{rf}	0.001	0.1	0.8
Completion Cell Properties	c_{pp}	30	40	80
	MLT_{PV}	0.5	1	2
	MLT_{TR}	1	2	10
Matrix Permeability Anisotropy	$kvkh$	0.05	0.1	0.2
Matrix Relative Permeability	$Krw\max$	0.15	0.25	0.5
	$Kro\max$	0.4	0.6	0.8
	Nw	1.5	2	3
	No	1.5	2	3
	Swc	0.1	0.15	0.3
	Sor	0.1	0.15	0.3

Table 5 summarizes the history matching methodology. The Matlab based in-house genetic algorithm program is used to minimize errors between history data and simulation results. In the injection phase, the well is controlled by injection rate and in the production phase, the well is constrained by total liquid production rate. It is worth noting that we have 365 days of production history data but we only take part of it (280 days) for history matching. The rest of data is used to test the predictive capability of history-matched models before the production forecast for next 20 years is carried on. The objective function to minimize during the history matching is aggregated summation of misfits in injection BHP, production BHP, and water rate. Each misfit is normalized by its own unit and weighted with coefficients so that the objective functions is dimensionless and fairly attributed to three different misfits.

Table 5. History matching methodology for the field application

History Matching Algorithm	Genetic algorithm (100 population/generation, total 10 generation)	
Well Constraints	Injection: pump rate	Production: liquid rate
Matching Period	Injection: 100 minutes	Production: 280 days
Objective Function	$f(\mathbf{m}) = \sum_{i}^{Inj\_steps}\left[\ln\left|\Delta inj\_BHP\right|_i\right] + \sum_{j}^{Prd\_steps}\left[\ln\left|\Delta prd\_BHP\right|_j + \ln\left|\Delta WRAT\right|_j\right]$	

Prior to history matching, it is important to identify influential parameters to efficiently history-match. In order to find heavy hitters in this history matching problem, a sensitivity analysis is performed where only one parameter is modified at-a-time while we freeze all other parameters. This shows how the change in a parameter affects the change in misfit. The high and low limits in the color code correspond to the high and low limits of parameter ranges in Table 4. Therefore, the parameters indicated with orange bar to the right and blue bar to the left have a positive relationship between the parameters and the misfit whereas the negative relationship between the parameters and the misfit is described with orange bar to the left and blue bar to the right.

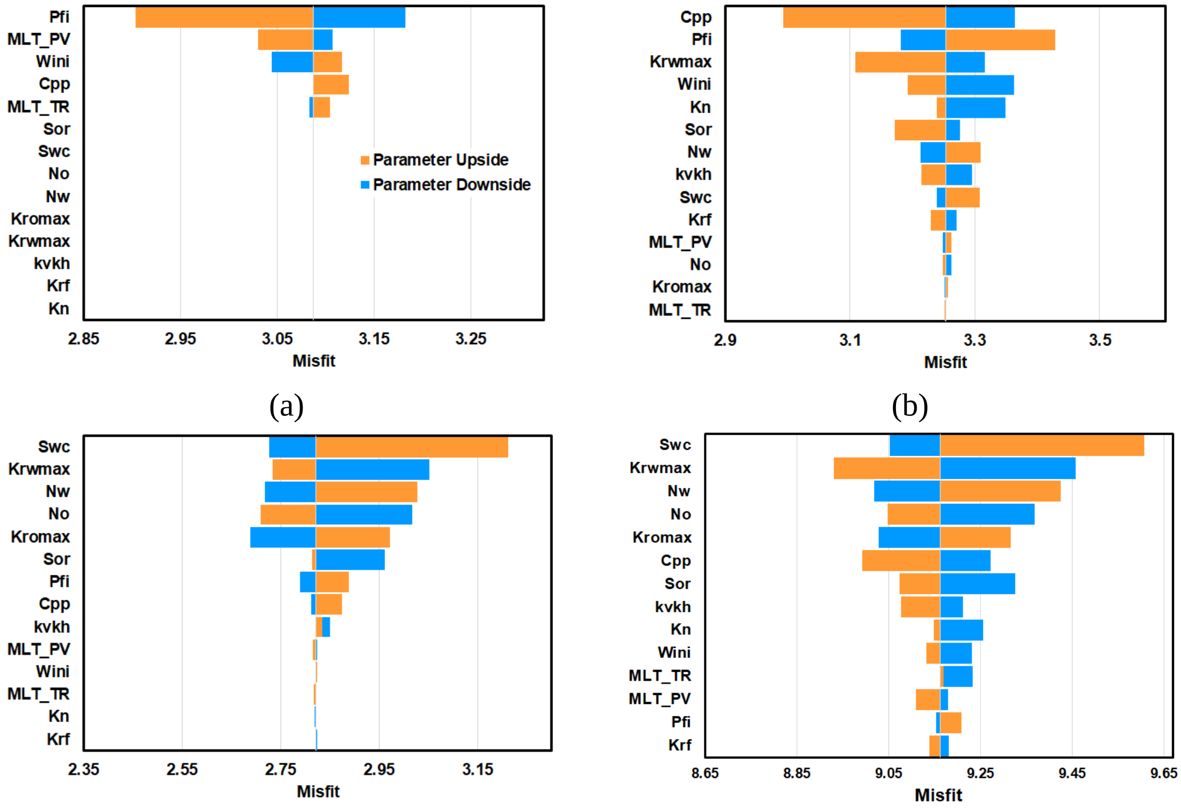

(a) (b)

(c) (d)

Figure 20. Tornado charts for sensitivity analysis before history matching: (a) Injection BHP misfit, (b) production BHP misfit, (c) water production rate misfit, (d) global misfit

From the tornado charts, the parameters associated with the dilation curve are found to be most influential to injection BHP misfit (Figure 20(a)). The production BHP misfit is mostly affected by parameters related to the dilation/compaction curves, porosity-permeability coefficient, and water relative permeability (Figure 20(b)). For water production, parameters associated with relative permeability are found to have huge impact (Figure 20(c)). The global misfit, weighted sum of misfit in injection and production BHP, and water rate production, is found to be dominated by relative permeability parameters and porosity-permeability coefficient (Figure 20(d)). In order to reduce the misfit efficiently during history matching process, the history matching is performed in two-stage. The first stage only includes more influential parameters based on Figure 20(d) (i.e., from s_{wc} to K_n) and after the first calibration, the second stage proceeds with the rest of the parameters.

The history matching results for the field application is presented in Figure 21. Figure 21(a) shows that the algorithm finds better solutions as history matching process proceeds. In the first calibration stage, the global misfit converged after the first five generations. After the rest of parameters were included in the second stage calibration, the global misfit started decreasing again. The models with smaller misfit were selected as updated models based on the red dotted-line in Figure 21(a) to compare with the initial population. Compared to the initial models, the updated models have substantially improved from the initial models and the comparisons show a good agreement in injection BHP (Figure 21(c)), production BHP (Figure 21(e)), and produced water rate (Figure 21(g)) during history matching period. The prediction after the history matching period well-captures the rest of production history which establishes its predictive capability and justifies the following production forecast for next 20 years.

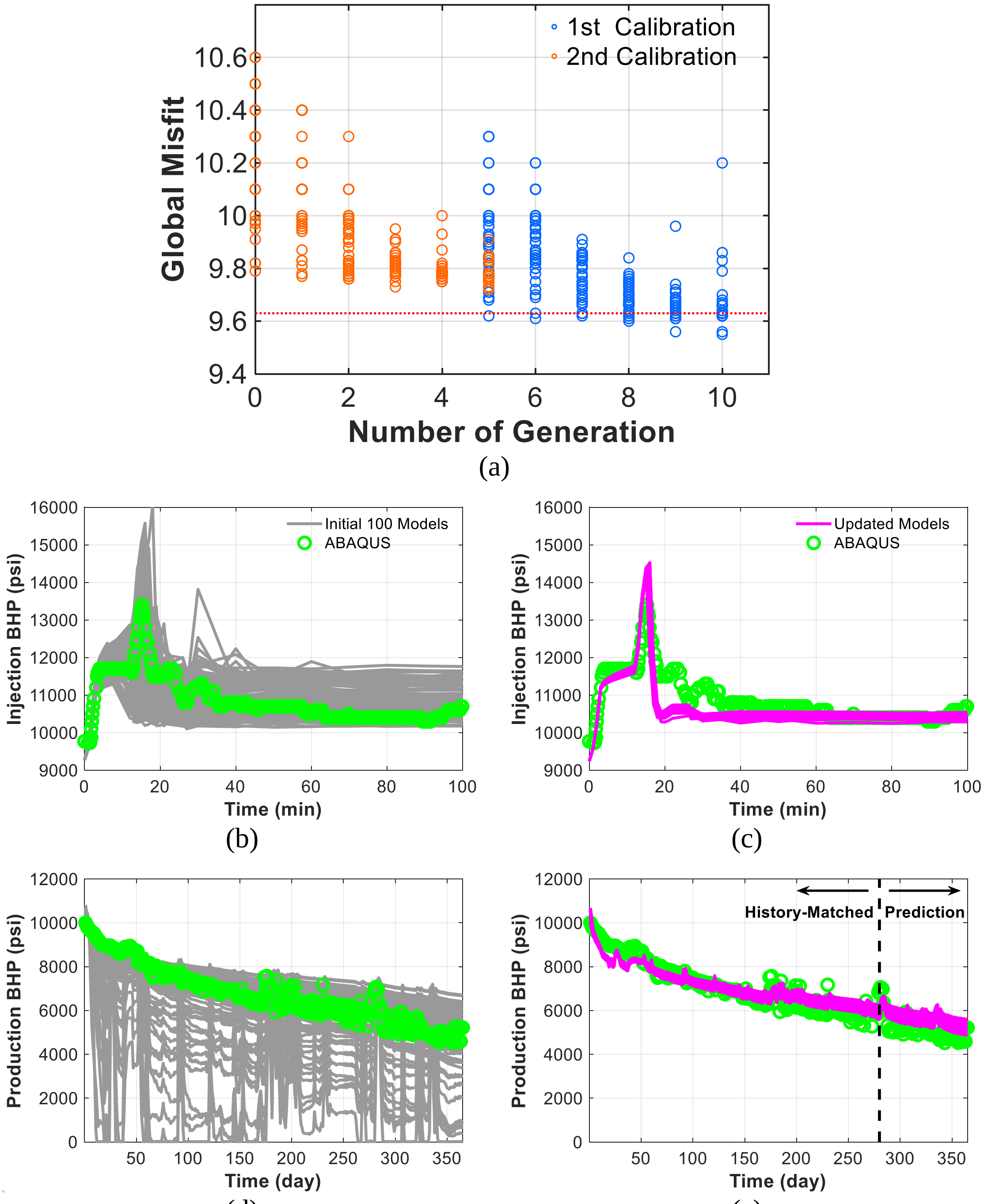

(a)

(b)

(c)

(d)

(e)

Figure 21. History matching results for the field application: (a) global misfit vs. the number of generation, initial 100 models vs. (b) injection BHP, (d) production BHP, (f) water rate history data and updated models vs. (c) injection BHP, (e) production BHP, (g) water rate history data

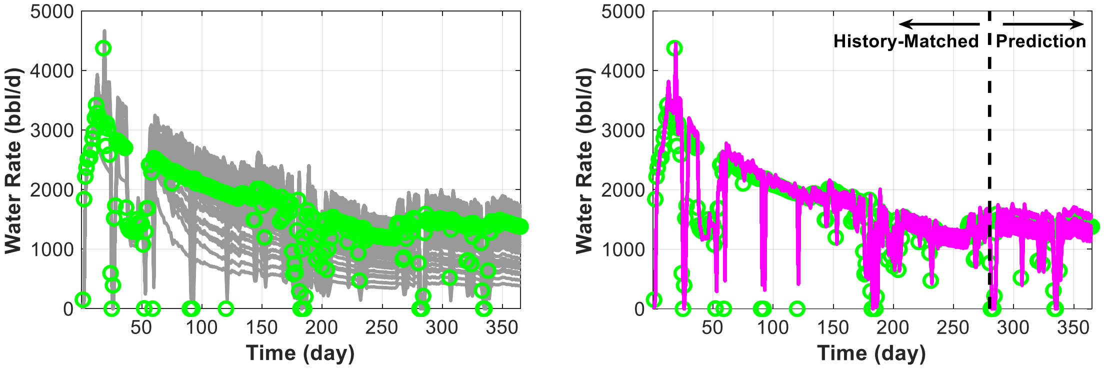

(f) (g)

Figure 21. Continued.

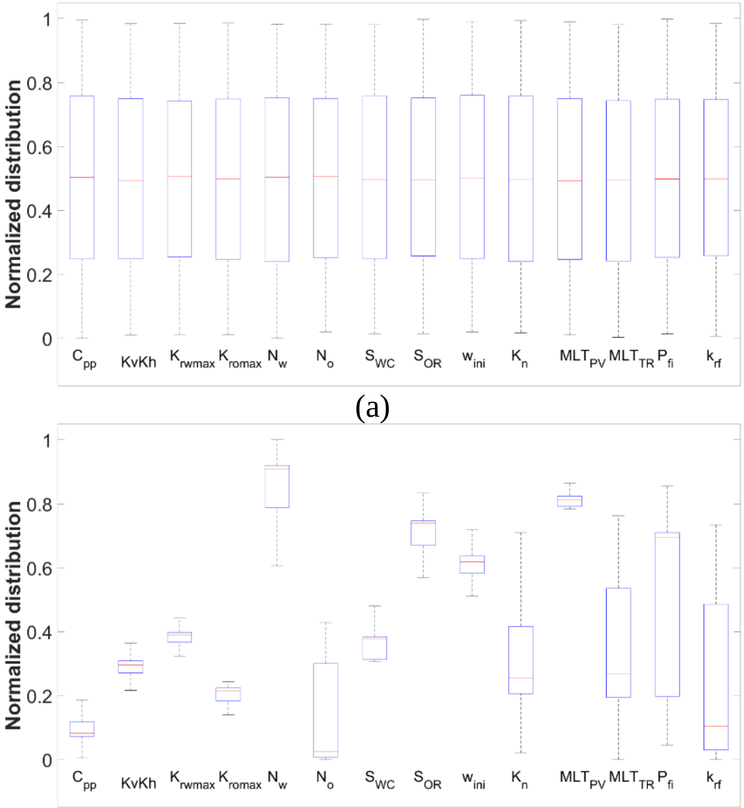

(a)

(b)

Figure 22. Normalized parameters distribution: (a) initial parameter distribution and (b) calibrated parameter distribution

The improvement after the model calibration also can be seen in parameter distribution (Figure 22). Before the model calibration, the parameters are uniformly distributed from the Latin hypercube sampling (Figure 22(a)). However, Figure 22(b) shows that the ranges of parameter have been reduced after the calibration which implies that uncertainties associated with the parameters are also reduced.

After the history matching, one of the history-matched cases is selected to show how permeability, water saturation, and pressure have changed from the initial state to the end of injection phase modeling. Figure 23 shows i-k cross-sectional view of permeability, saturation, and pressure in a fracture plane at the initial state and after the stimulation. In this history-matched model, the hydraulic fractures formed 450ft of the fracture half-length and 240ft of the fracture height after the stimulation (Figure 23(d)). The retained permeability after the stimulation is passed to the subsequent production phase modeling and during the production phase the permeability decreases based on the pressure-governed Barton-Bandis model as reservoir is depleted. The workflow not only provides the production phase with fracture geometry and permeability but also it transfers saturation and pressure distribution after the stimulation to the production phase modeling as initial conditions. For example, Figure 23(e) shows high water saturation around the wellbore. This naturally results in high water cut at early production, which is typically observed in hydraulically fractured shale reservoirs. This allows the early well response in the production phase modeling to demonstrate early production history data without separately calibrating fracture parameters or fracture saturation.

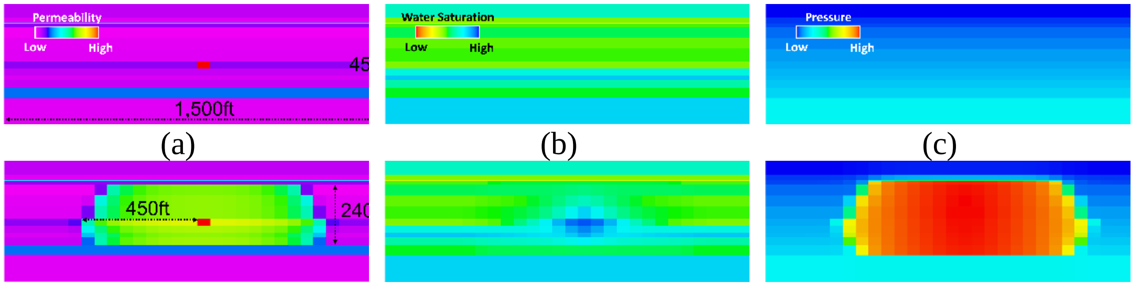

(a) (b) (c)

(d) (e) (f)

Figure 23. Permeability, water saturation and pressure at the initial state (a)-(c) and after the stimulation (d)-(f)

After the predictive capability of the history-matched models is confirmed (Figure 21), possible EUR and NPV range for the well are investigated. The population-based history matching algorithm finds the ensemble of history-matched models, which allows us to employ probabilistic analysis on EUR and NPV. The EUR is based on the cumulative oil production forecast for the next 20 years (Figure 24(a)). For the forecast period, the well is constrained by fixed BHP with the last history value. After the model calibration, EUR for this particular well ranges from 360 to 480Mbbl with P10 being 365Mbbl, P50 being 401Mbbl and P90 being 414Mbbl (Figure 24(b)). The NPV calculation is based on the assumptions summarized in Table 6. The economic assumptions also include 10% of discount rate, 0.4 of shrinkage ratio, and 120bbl/MMscf of NGL yield. The CAPEX includes drilling and completion costs and the OPEX includes fixed monthly costs and costs proportional to the production. The commodity prices are assumed to be flat for the entire period and working interest (WI) and net revenue interest (NRI) are assumed to be 75% and 100%, respectively. Given the assumptions, NPV ranges from 3MM$ to 6MM$ with P10 being 3.2MM$, P50 being 4.2MM$, and P90 being 4.5MM$ (Figure 24(c)).

Table 6. Assumptions used for net present value (NPV) calculation

Parameters	CAPEX	OPEX	Pricing (flat)	WI / NRI
Value	6.5 MM$	12,000 / month Oil: $2.4 / bbl Water: $0.5 / bbl Gas: $1.2 / Mscf	Oil: $50 / bbl Gas: $2.5 / Mscf NGL: $20 / bbl	75% / 100%

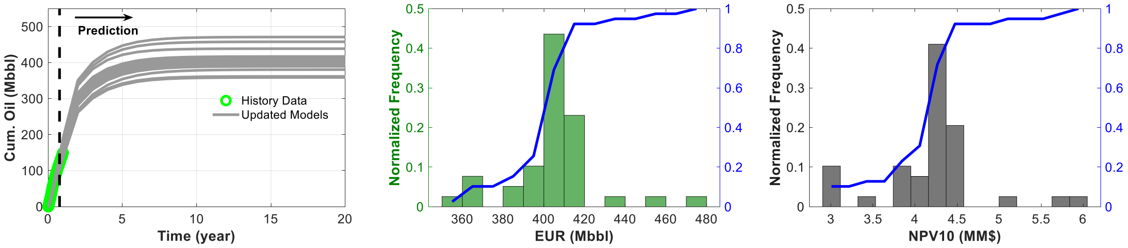

(a) (b) (c)

Figure 24. EUR prediction: (a) cumulative oil production for the next 20 years, (b) histogram and CDF of EUR, (c) histogram and CDF of NPV

After the model calibration, the sensitivity on completion design can be investigated to find the optimum completion design. Instead of directly calibrating fracture parameters to match production history data, the workflow calibrates the empirical dilation/compaction curves and the fracture parameters are resulted from injection phase modeling that incorporates the curves. This allows us to link completion design parameters to fracture parameters and corresponding production profile and NPV. If we explicitly tuned fracture parameters during the model calibration, different completion design sensitivity cannot be investigated because forward fracture propagation modeling is missing in the workflow. It is assumed that the curves do not change with different completion designs because the shape and physical parameters of the curves should depend on rock characteristics and in-situ stress which are independent of the completion design. The example presented in Figure 25 shows fluid injection volume sensitivity on fracture geometry and permeability. The fluid volume is changed from 50% to 150% of the current practice and the fracture parameters are obtained from the injection phase modeling using the calibrated dilation/compaction curves (Figure 25(a)-(e)). Note that other completion design parameters such as cluster and well spacing are fixed.

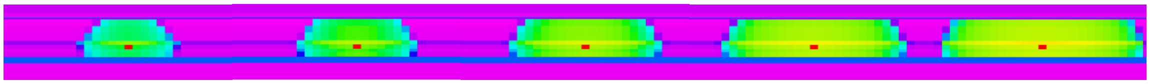

(a) (b) (c) (d) (e)

Figure 25. Completion design sensitivity on injection fluid volume: fracture geometry and permeability at (a) 50%, (b) 70%, (c) 100%, (d) 130%, (e) 150% of the current practice fluid injection volume

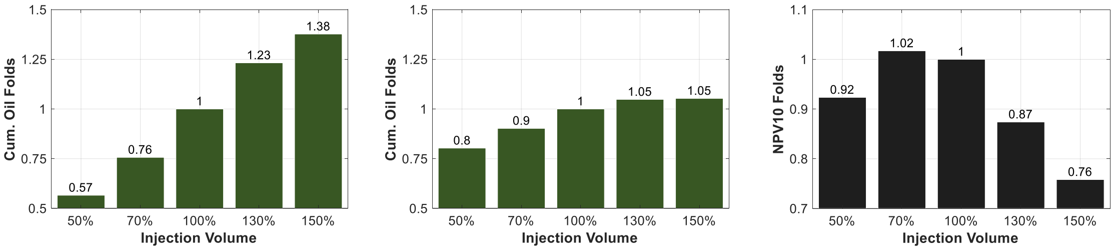

(a) (b) (c)

Figure 26. Cumulative oil production folds after (a) 1 year and (b) 20 years and (c) NPV10 folds compared to 100% injection fluid volume case

Given hydraulic fractures from different injection fluid volumes, the models were simulated with history BHP constrained. Their cumulative oil production and NPV10 are assessed to find the optimum fluid injection volume. NPV10 is calculated based on the economic assumptions in Table 6 while completion portion in CAPEX is assumed to be proportional to fluid injection volume. Figure 26(a) shows that 1-year cumulative oil production roughly follows the injection volume implying that larger fractures are beneficial to efficiently recover oil in early time. However, the difference in the oil recovery between the models is less substantial in 20-year cumulative oil production. For example, even fluid injection volume larger than the current practice does not benefit much cumulative oil production after 20 years. This implies the current practice is close to the optimum because the same oil volume can be recovered with smaller fluid injection volume. However, Figure 26(c) shows that little extra monetary value is possibly realized with slightly less injection volume than the current practice. This result should highly depend on the economic assumptions such as commodity price and CAPEX. However, the demonstration of the proposed workflow applied to the field case should be beneficial for unconventional field development planning and economic decision making and easily replicable to other completion design parameters such as cluster and well spacing.

Conclusion

Previous FMM-Sim studies, which transform a 3D reservoir model into an equivalent 1D model using the DTOF, have shown its efficiency in reservoir modeling and history matching of hydraulically fractured shale wells. However, the fracture parameters such as fracture permeability and geometry were directly calibrated during history matching that the calibrated models were only valid at given completion designs.

Therefore, we extended the workflow to the injection phase so that completion design can be tied to fracture parameters to investigate the impact of completion design on production profiles. In the proposed workflow, the fracture propagation is simulated using a simplified physical model for pressure-dependent fracture compaction/dilation curves in 3D FD. The compaction/dilation curves rely on physical parameters to represent permeability and porosity modification as function of pressure and the model was validated with ABAQUS. The results of injection phase which include fracture parameters, pressure and saturation distribution are seamlessly transferred to FMM-Sim as input for the subsequent production phase. The proposed workflow was applied to a field case to injection and production history matching, calibrating the compaction/dilation curves for fracture parameters. With multiple history-matched models, possible ranges for NPV10 and EUR for the well were assessed and the calibrated curves were used to investigate the impact of the fluid intensity on production profiles and NPV10.

The workflow has been proposed in practical and efficient manner in the sense that the entire workflow, from the fracture propagation to the following production, can be performed in any FD simulator. Even with a room for improvement in the presented workflow, including interaction between multi-wells and fracture propagation in depleted reservoirs, the efficient computation from the fracture propagation to the production would be beneficial for field operation in unconventional field development planning and economic decision making.

CHAPTER III

HYBRID PHYSICS AND DATA-DRIVEN MODELING FOR UNCONVENTIONAL FIELD DEVELOPMENT[*]

Chapter Summary

The objective of this study is to develop a hybrid model by combining physics and data-driven approach for unconventional field development planning. We used physics-based reservoir simulations to generate training datasets. These simulation results were incorporated into data-driven machine learning (ML) algorithms so that the algorithms can learn the underlying physics from reservoir simulation input and output. The ML model is trained such that it provides fast and scalable applications with good accuracy to find optimum unconventional field development, accounting for geological properties, completions design, well spacing and child well timing.

We trained ML models with reservoir simulation inputs and cumulative oil production for parent and child wells. A single half-cluster reservoir model was built where fracture propagation is simulated with pressure-dependent fracture properties and a child-well is introduced with different timing and well spacing. After performing a

---

[*] Part of this chapter is reprinted from Park, J., Datta-Gupta, A., Singh, A. and Sankaran, S., 2020a. Hybrid Physics and Data-Driven Modeling for Unconventional Field Development–Onshore US Basin Case Study. Unconventional Resources Technology Conference (URTEC) with permission from URTeC, whose permission is required for further use.

sensitivity analysis to reduce the number of training inputs, more than 20,000 simulations results were generated as the training data. The best accuracy, R2=0.94, was achieved with the neural network model after tuning hyper-parameters. Then, we incorporated the trained model with the genetic algorithm to perform efficient history matching to calibrate model parameters.

The hybrid model, physics-embedded machine learning model, is extremely efficient that it takes several minutes to complete a single well history matching. The prediction from the history-matched hybrid model is physically meaningful showing that it properly captures the impact of fracture geometry, child well spacing, and timing on production. With the multiple history matching results, we populated spatial distribution of estimated ultimate recovery (EUR) and calibrated model parameters. To validate the workflow, a blind test was conducted on selected areas from US onshore field. The model prediction with the populated parameters was found to be in good agreement with the actual production history indicating the predictive capability of the hybrid approach.

The proposed model can provide quick and scalable solutions that honors underlying physics to help decision making on unconventional field development. The model can capture interactions between wells including production degradation due to child-well effect. By calibrating model input parameters over the entire basin, we can predict EUR, yearly cumulative oil followed by economic metrics such as NPV10 at any location in the basin. The impact of different completion design (e.g., fluid intensity, cluster spacing) on production profile and economic matrices is also quickly assessed.

Introduction

One of the challenges in unconventional field development is to find the optimum number of wells to place in a section or a given area to efficiently recover hydrocarbon. However, finding the optimum field development strategy is a complex problem associated with multiple variables including geologic properties, completion design, well placement, and initial reservoir condition. Therefore, it is not straightforward to tackle the problem and establish a predictive model for optimum field development. Moreover, we occasionally need to place a parent well first to secure operatorship or for appraisal purposes and come back later to place a child well next to the parent well. If this is the case, it is possible that the reservoir of the child well is partially depleted by the parent well. Thus, the child well performance might not be as good as the parent well performance. This production degradation is called child well effect and the production degradation is a function of the child well spacing and timing. Quantifying the child well effect would be also beneficial to field development planning. For example, tighter spacing should not be necessary for a child well that is introduced long time after a parent well. The optimum spacing for a child well should become larger with longer child well timing.

For unconventional field development, the oil and gas industry has been mainly using decline curve analysis (DCA) (Kanfar and Wattenbarger, 2012; Valkó and Lee, 2010), multivariate analysis (MVA) (Maucec et al., 2015; Schuetter et al., 2018; Singh, 2016), rate transient analysis (RTA) (Baek et al., 2019; Song and Ehlig-Economides, 2011), and reservoir simulation (Kim et al., 2019; Liang et al., 2019; Park and Janova, 2020). All of them can be suitable tools with advantages and disadvantages, depending on a problem type and approach that a practitioner wants to take.

To briefly mention each method, DCA is based on pure curve fitting without consideration of geologic properties or operating conditions. It is a simple and powerful tool to forecast production and estimate ultimate recovery which makes DCA the most popular tool for unconventional reservoirs. However, DCA cannot predict the production for a potential incoming well because DCA is only applicable if production data is available (i.e., after the production started). Also, with few data points, the prediction might be uncertain and yield multiple interpretations.

Multivariate analysis (or data analytics, machine learning) is a purely data-driven approach which can draw insights from large data sets. It efficiently processes large data sets and is powerful to capture complex and indistinct interactions between the data. However, the limitation of the method is that the analysis is only effective within the acquired (or trained) data range. In other words, it can effectively interpolate between data points but its extrapolation is not credible. Besides, these are pure data-driven methods that cannot be often physically interpreted or used to explain the outcomes.

RTA is based on simplified physics, incorporating bottom-hole pressure and fluid production rates data. It can identify flow regimes assuming simple fracture geometry and reservoir configuration to help characterize stimulated fracture surface and enhanced formation permeability (Wattenbarger et al., 1998). Also, it can efficiently forecast production and estimate oil recovery. However, it is not sufficient to account for complex dynamics in unconventional reservoirs such as interaction between parent-child wells.

Reservoir simulation is the most robust method based on numerically discretized physics which can solve challenging problems including hydraulic fracture propagation, multi-phase fluid flow in subsurface and interaction between multiple wells. However, it is not easily scalable to the entire acreage or basin because of demanding resources and manpower compared to the other methods. The number of drilled and completed wells in unconventional reservoirs outpaces the number of wells that can be analyzed with reservoir simulations. Starting from integrating high resolution geologic data followed by upscaling and upgridding to build a model and the model calibration might take up to months.

In general, it is fair to say that the aforementioned methods are faster and more scalable leftward in Figure 27, and toward right, the methods provide more accurate results, adding up more complexity. It would be the best practice to adequately utilize all the methods balancing their advantages and limitations. There also have been efforts to develop new methodologies and models for unconventional reservoirs other than the listed methods such as rapid fast marching-based reservoir simulation techniques (Iino et al., 2017b; Zhang et al., 2016), novel model-free production data analysis methods (Xue et al., 2019b; Yang et al., 2017a), and models combining data and physics (Molinari et al., 2019; Zhang et al., 2018).

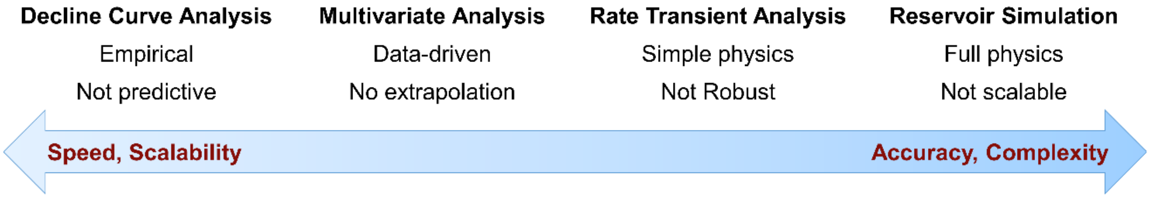

Figure 27. Common industry practices for unconventional field development

The objective of the current study is to build a hybrid model by combining strength of current practices in the industry. Thus, the proposed model can provide fast and scalable applications with high accuracy to address challenges in unconventional field development. Specifically, we tried to combine physics and data-driven approach at field scale to find the optimum field development strategy (Figure 28). We used physics-based reservoir simulations to generate training materials and incorporate them into machine learning algorithms to embed physical meaning between the reservoir simulation input and output. Therefore, the hybrid model proposed in this study can achieve high accuracy in well performance prediction with scalability. The hybrid model is designed to be practical and efficient to address challenges in unconventional field development. Specifically, this study aims to address the optimum well spacing and production degradation of child well using the hybrid model and provide a practical solution for field development planning and economic decision making.

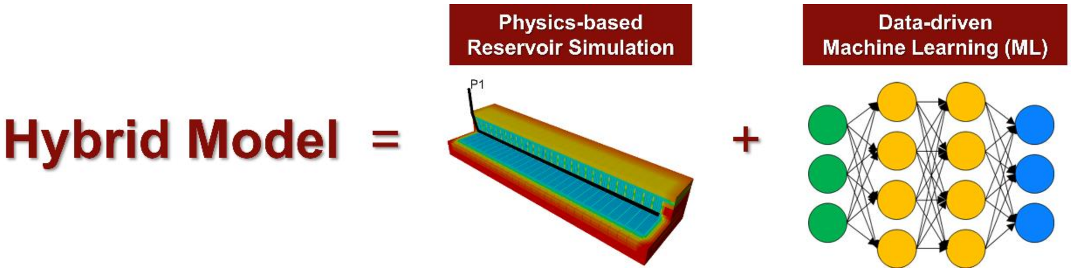

Figure 28. Schematic of hybrid modeling, combining physics-based reservoir simulation and data-driven machine learning algorithms

Methodology

The hybrid model is built by combining physics-based reservoir simulation and data-driven machine learning algorithms. First, multiple reservoir models with different reservoir and completion parameter combinations are simulated to generate production profiles. Next, the machine learning algorithms are trained with simulation input parameters and production profiles such that the machine learning models can pick up the physical interaction between the simulation input and the output. We ensured that when production profiles are generated, simulation input covers all plausible parameter ranges that can be foreseen within the basin or acreage. Thus, when it comes to the application, well performance is predicted within the trained parameter ranges.

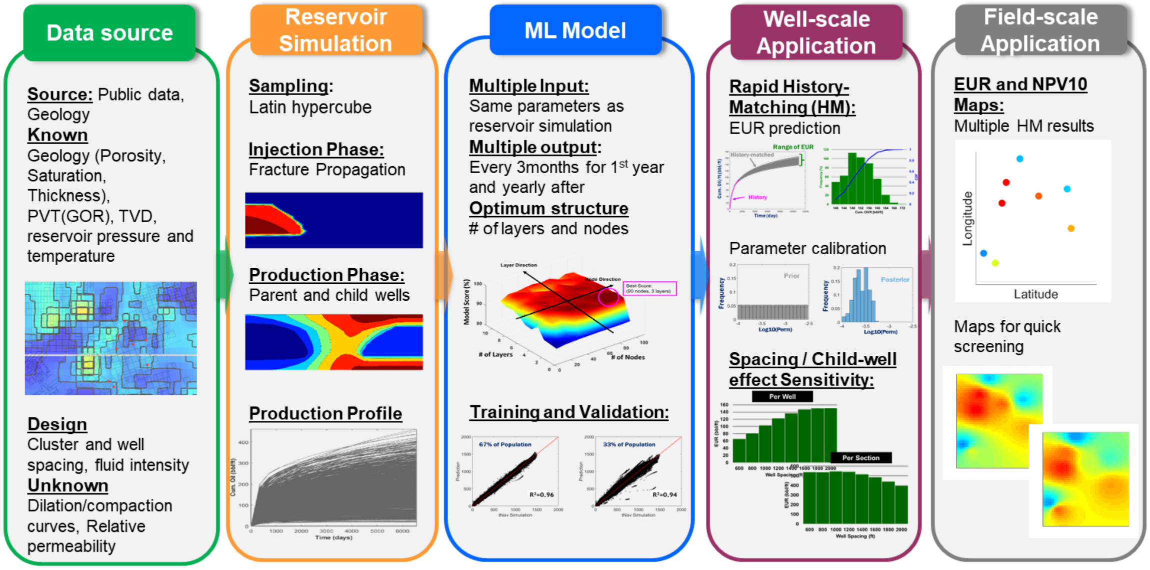

Figure 29. Hybrid modeling workflow, from data gathering to field-scale application

Figure 29 shows the hybrid modeling workflow. A brief introduction of each step is given below and will be revisited in detail later.

1. Data Source: First, the available data is gathered from public sources and database including geologic properties, reservoir properties, initial reservoir conditions, completion designs and production data. We categorize input data into three groups: 1. known parameters, the parameters that we already know, 2. design parameters, the parameters that we have control of, and 3. unknown parameters, the parameters we do not know yet to calibrate. For finding the best field development strategy, the design parameters, which are mainly associated with completion design, will be varied and corresponding production and economic metrics will be investigated.

2. Reservoir Simulation: With the selection and categorization of the simulation inputs, we proceed to reservoir simulations. The reservoir simulation is comprised of injection and production phases of hydraulically fractured wells. The pressure-dependent fracture dilation/compaction curves are utilized to mimic fracture propagation and closure in flow simulations. Therefore, the injection phase emulates the fracture propagation and subsequently, the production phase is simulated with the retained fracture geometry and permeability. Note that the injection and production phases are simulated using the same simulator that lends itself to facilitate an automatic workflow. During the production phase, a child well is introduced with the well spacing and timing as parameters. As a result, production profiles for parent and child wells are obtained.
3. Machine Learning Model: Next, machine learning (ML) algorithms take reservoir simulation input parameters and production profiles for training. Multiple ML algorithms are tried to find the best fit for this particular problem. In this process, the focus is to improve accuracy of the model by tuning hyper parameters (or structure of ML model) without modifying the loss function. The trained models need to be cross-validated and the model with the best accuracy is selected.
4. Well-scale Application: After the hybrid model is built, the model is applied at the well-scale. The hybrid model is incorporated with a history matching algorithm. This is a shift in paradigm: usually, a reservoir simulator is used for history matching and yet we utilize the hybrid model to history-match that we largely benefit from computation time. By incorporating the history matching algorithm

with the hybrid model, we can forecast production and calibrate unknown parameters with great efficiency. After the model calibration, sensitivity of design parameters (e.g., completion design, lateral well spacing and child well timing) can be investigated.

5. Field-scale Application: With multiple history matching results, value acreage maps such as EUR and NPV10 can be generated to help the field development planning and economic decision making in the area of interest. Calibrated unknown parameters at multiple locations can be interpolated to locations where we do not have drilled wells. Thus, we are able to assess well performance with modified design parameters at potential well locations for the development plan.

The significance of the proposed hybrid modeling workflow is that underlying physics in reservoir simulator including hydraulic fracture propagation and subsequent production are embedded into the machine learning algorithm. This allows design parameters such as completion design and well spacing to link to well performance which helps optimize field development with significant speed up in computation time. To mimic the geomechanical behavior of hydraulic fracture in a flow simulator, we employed pressure-dependent fracture dilation/compaction curves and assigned the curves to potential fracture paths. For example, Figure 30(a) shows potential fracture propagation paths. Along the paths, transmissibility (Figure 30(b)) and pore-volume (Figure 30(c)) multipliers are assigned as function of pressure. The curves are motivated by laboratory experiments, numerical modeling of fracture property modification due to stress and pressure change in rocks, and theoretical background including linear elastic fracture mechanics. The previous study (Park et al., 2020c) parameterized the shape of the curves by introducing physical parameters so that the curves can be calibrated during history matching and used for completion design optimization. The simplified pressure-dependent curves were validated with the cohesive zone model in ABAQUS, a fully coupled fluid flow and geomechanical simulator, and also applied to a field case. This study takes the same approach to emulate geomechanical behavior of the hydraulic fractures in a flow simulator.

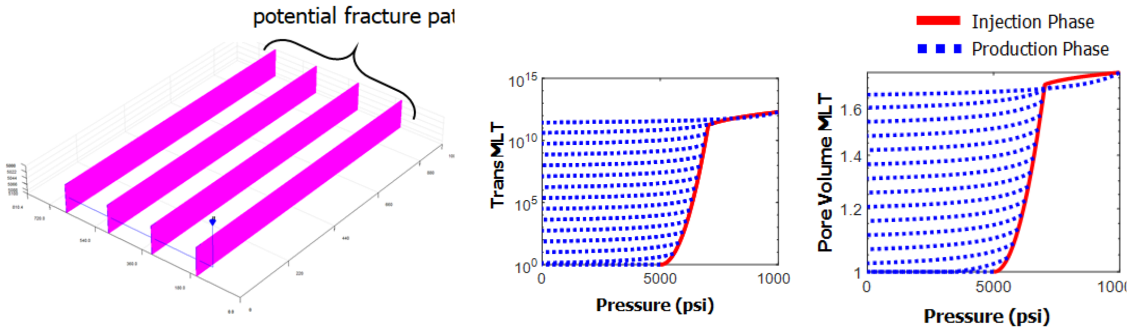

(a) (b) (c)

Figure 30. Pressure-dependent fracture property curves to mimic fracture propagation in a flow simulator: (a) potential fracture paths, (b) transmissibility multiplier curves, and (c) pore-volume multiplier curves (after Park et al. (2019b))

The hybrid model is a forward simulator with high efficiency and we incorporated it with a genetic algorithm for history matching. The population-based optimization algorithm provides an ensemble of history-matched models to forecast oil production and calibrated history matching parameters. This enables probabilistic analysis and uncertainty assessment of the well performance and the calibrated parameters. Given the calibrated unknown parameters, we can investigate the sensitivity of the design parameters on oil production and economic metrics. More importantly, the parameters in the area without wells can be spatially interpolated with the history matching results. Therefore, the interpolated unknown parameters can be used to assess potential new well performance. This implies that the hybrid model is applicable to find the optimum development strategy in the area even without sufficient input data. The details of the hybrid modeling application with history matching will be revisited.

Data Gathering and Range

Data are collected from public sources and database including geologic properties, initial reservoir conditions and completion design to provide input parameters for reservoir simulations. The input parameters for the reservoir simulations are categorized into three groups. Known parameters are the input parameters that we already have access to the information from the database. Design parameters are the input parameters that we have control of, mainly including completion design parameters. Unknown parameters are the input parameters that we do not have information and yet they are going to be calibrated after history matching. The known parameters include initial reservoir condition, geologic properties (porosity, water saturation, and thickness of each formation), and fluid PVT. The design parameters include well configuration and completion design: fluid intensity, cluster and well spacing and child-well timing. Note that well spacing in this study refers to lateral well spacing. The unknown parameters include permeability of each formation, dilation/compaction curves for hydraulic fractures, and relative permeability. Figure 31 illustrates parameters associated with compaction/dilation and relative permeability curves, respectively. The dilation/compaction curves are for hydraulic fractures. The assumption that we can simply express fracture properties as function of pressure enables to mimic fracture propagation and closure in reservoir simulations. The relative permeability curves follow a typical Brooks-Corey model. The bottom-hole pressure trend could be one of the design parameters (e.g., aggressive choke for large drawdown or less aggressive choke for small drawdown) to operate a well. However, in this study, the bottom-hole pressure trend is fixed by taking the average of available bottom-hole pressure trends.

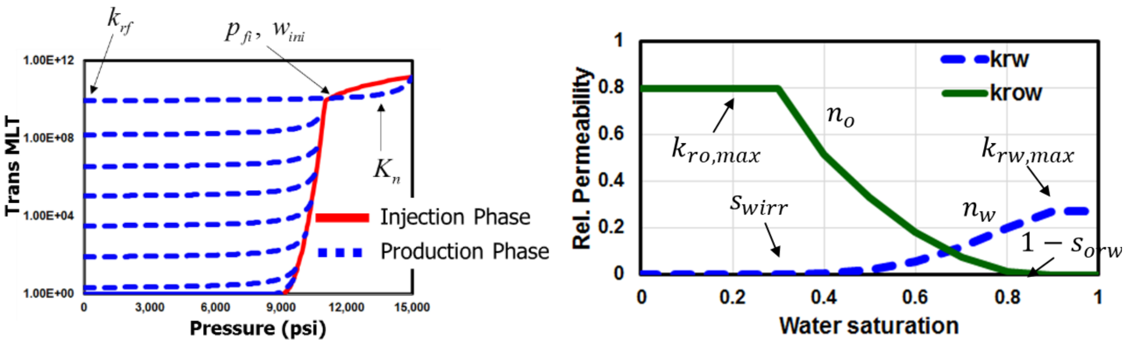

(a) (b)

Figure 31. Schematics of (a) dilation (injection)/compaction (production) curves, (b) Corey-type relative permeability curves and associated parameters

Table 7 lists reservoir simulation input parameters and their ranges. Parameters with an asterisk indicate that these parameters have values for formation A, B and C. In Table 7, there are 34 parameters in total. However, the number of unknown parameters will be reduced after performing sensitivity analysis. The purpose of sensitivity analysis is to identify influential parameters and reduce the number of parameters by excluding less influential parameters. While gathering data, it should be emphasized that the data-driven approach is not effective with parameters beyond the training ranges. Therefore, input parameters range should be appropriately setup such that it covers the entire possible ranges for applications.

Table 7. Input parameters for reservoir simulations and their range

Parameter Type	**Category**	**Parameters**	**Range**	
			Min	**Max**
Known Parameters	Initial Reservoir Conditions	Reservoir Pressure (psi)	8,000	10,000
		Reservoir Temperature (°F)	150	200
	Geologic Properties	Porosity*	0.05	0.1
		Water Saturation*	0.2	0.75
		Thickness* (ft)	100	340
	Fluid PVT	API	39	54
		Gas Gravity	0.72	0.81
		Gas Oil Ratio (Mscf/bbl)	0.95	5.5
		Bubble point pressure (psi)	3,000	3,500
	Well Configuration	True Vertical Depth (TVD) (ft)	9,500	13,000
Design Parameters	Well Configuration	Fluid Intensity (bbl/ft)	25	60
		Cluster Spacing (ft)	20	40
		Well Spacing (ft)	200	3,000
		Child Well Timing (year)	0	3
Unknown Parameters	Geologic Properties	Permeability* (md)	0.003	0.0002
	Dilation Curve	Fracture initiation pressure, p_{fi} ,(psi)	1,500	2,000
		Initial fracture width, w_{ini} ,(ft)	0.001	0.005
		Permeability-porosity coefficient, c_{pp}	20	40
	Compaction Curve	Fracture stiffness, K_n , (MPa/mm)	1	10
		Fracture residual perm ratio, k_{rf}	0.005	1
	Relative Permeability	k_{romax}	0.6	0.8
		k_{rwmax}	0.5	1.0
		n_o	1.5	5
		n_w	1.5	5
		s_{wirr}	0.1	0.4
		s_{orw}	0.1	0.4

Reservoir Simulation Setup

After reservoir simulation input is set, we built a reservoir model to run simulations. Figure 32(a) shows the schematic of a two-well pad and we modeled a part of the two-well pad, highlighted with a magenta box. The model has two wells and each well has half-fracture. The model consists of formation A, B and C and the formation B is the target formation where the hydraulic fractures propagate (Figure 32(b)). Each formation is assumed to be homogenous. Therefore, one representative value for porosity, water saturation, and permeability is assigned for each formation. In order to take cluster and well spacing as well as formation thickness into simulation input, we allow DX, DY and DZ to change accordingly while the total number of cells in the reservoir simulation model is fixed. The total number of cells in the model is 8,800. There are 11, 40 and 20 cells for NX, NY, and NZ, respectively. Thus, the model size can change in x, y, and z-direction depending on cluster and well spacing and formation thickness by adjusting DX, DY and DZ, respectively. Tartan gridding is used to describe hydraulic fractures and two different relative permeability curves are assigned for the fractures and matrix. While the matrix relative permeability curves vary according to the range in Table 7, the relative permeability for hydraulic fractures is fixed to be straight line (Pieters and Graves, 1994). Given the initial reservoir pressure and TVD parameters, the pressure gradient is calculated and the initial pressure values are assigned with the depth in the reservoir model.

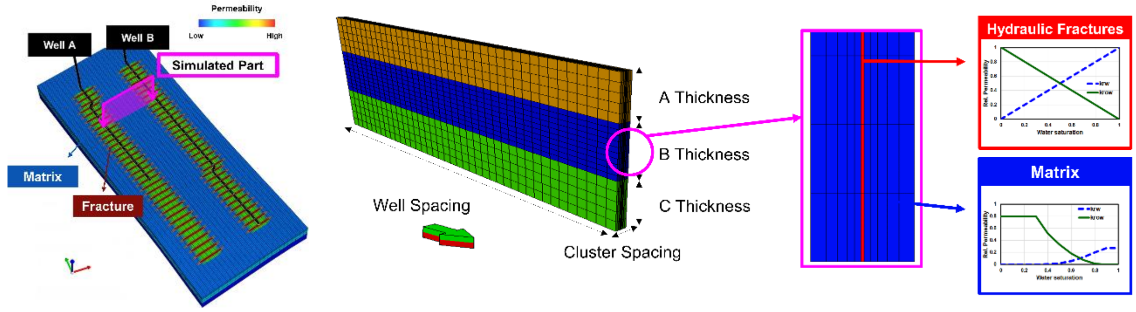

(a) (b)

Figure 32. Reservoir simulation model: (a) schematic of two-well pad (after Park and Janova (2020)) and (b) single half-cluster reservoir model

The reservoir simulation consists of two consecutive steps – namely, injection and production phase simulations. Figure 33 and Figure 34 show pressure maps at different timing in injection and production phases, respectively, to help better understand how the simulation proceeds. First, the injection phase of the parent well is simulated (Figure 33). Given the dilation curve, fracture permeability increases as function of pressure so that it mimics hydraulic fracture propagation. During injection phase, the well is constrained by injection rate. The injection rate is calculated based on fluid intensity and cluster spacing which are the design parameters in Table 7. These two parameters determine the total fluid injection volume and the rate is calculated accordingly, fixing the total injection time of 1-hour.

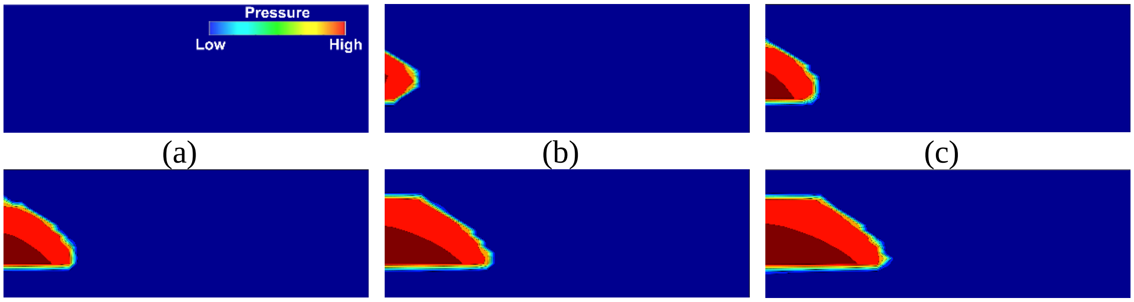

(a) (b) (c)

(d) (e) (f)

Figure 33. Pressure maps at different timings during injection phase

Next, the simulation proceeds to the production phase (Figure 34). The initial conditions for the production phase such as pressure, saturation as well as fracture geometry and permeability are inferred from the result of the injection phase as restart parameters. During production phase, the parent well starts producing first and the child well is introduced with a time gap. The introduction timing is one of design parameters which varies from 0 to 3 years. In this study, the fracture parameters such as fracture geometry and permeability for the child well are assumed to be identical as the parent well. The parent and child wells are constrained with the bottom-hole pressure where the decline starts from the initial reservoir pressure parameter and converges to the bubble point pressure parameter in 1-year, following a typical drawdown trend in the target basin. Therefore, production operation is also depending on sampled initial reservoir pressure and bubble point pressure. After the simulation, the cumulative oil production profiles for both parent and child well are obtained as output. The frequency of production output is every 3 months for the first year and every year afterward for 30 years. Hence, there are 34 points in the cumulative production profile.

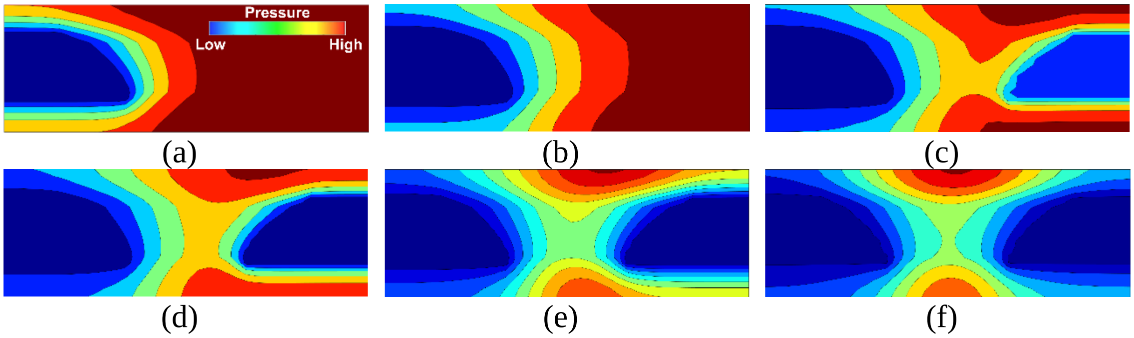

Figure 34. Pressure maps at different timings during production phase

After the reservoir simulation is setup, we performed sensitivity analysis. The purpose of sensitivity analysis is to find the heavy hitters. Heavy hitters are parameters that are more influential than others to simulation results. Once we identify heavy hitters based on their influence on the results, we can screen-out less influential parameters to reduce the number of unknown parameters for history matching. To identify influence of each parameter, we used the Distance-based Generalized Sensitivity Analysis (DGSA) (Fenwick et al., 2014; Park et al., 2016). DGSA first classifies the output response by clustering and finds variations of parameter distribution in each class to indicate parameter sensitivity. Figure 35 shows the procedure for DGSA. First, we sample parameters using Latin hypercube sampling method from predefined parameter ranges, listed in Table 7. Given the parameters, multiple reservoir models are setup and simulated, and cumulative oil production profiles are obtained. Next, the production profiles are clustered based on the optimum L1 distance between the profiles. For example, in Figure 35, the cumulative oil production profiles are classified into two groups. For each parameter, the cumulative distribution function (CDF) for the entire sample set and samples within each cluster are calculated. The underlying logic is that if parameter distributions are distinct between clusters, that parameter is considered to be influential. This is because a large difference in the parameter distributions drives dissimilarity in output responses.

Figure 36 shows a tornado chart after performing sensitivity analysis, indicating the influence of each parameter. Based on the tornado chart, insensitive parameters among the unknown parameters: n_o, k_{romax}, k_{rwmax}, Formation A and C permeability, initial fracture width, fracture stiffness, and fracture initiation pressure are excluded. This reduces the number of parameters from 34 to 26. The finalized parameters to train in machine leaning algorithms are as follows. There are four design parameters including cluster and well spacing, fluid intensity, and child well timing. Known parameters include porosity, water saturation and thickness of Formation A, B and C, initial reservoir pressure and temperature, True Vertical Depth (TVD), Gas Oil Ratio (GOR), oil API, and gas gravity. We have six unknown parameters and two of them are associated with dilation/compaction curves (permeability-porosity coefficient and fracture initiation pressure), three of them are associated with relative permeability (s_{wc}, s_{or}, n_o) and there is the permeability for Formation B. The six unknown parameters need to be calibrated by history matching and the calibration of Formation B permeability will be presented as an example.

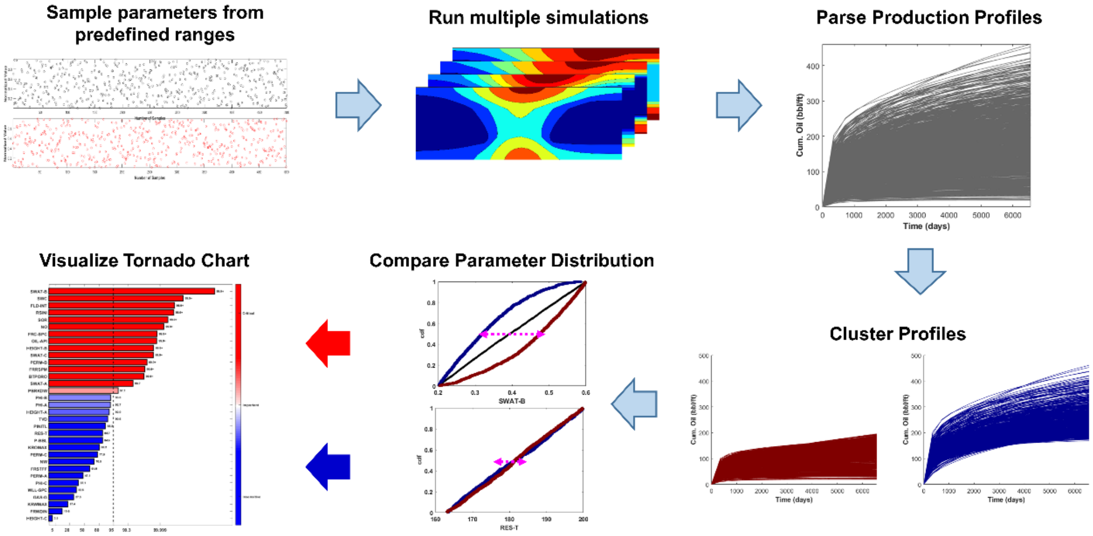

Figure 35. Distance-based generalized sensitivity analysis procedure

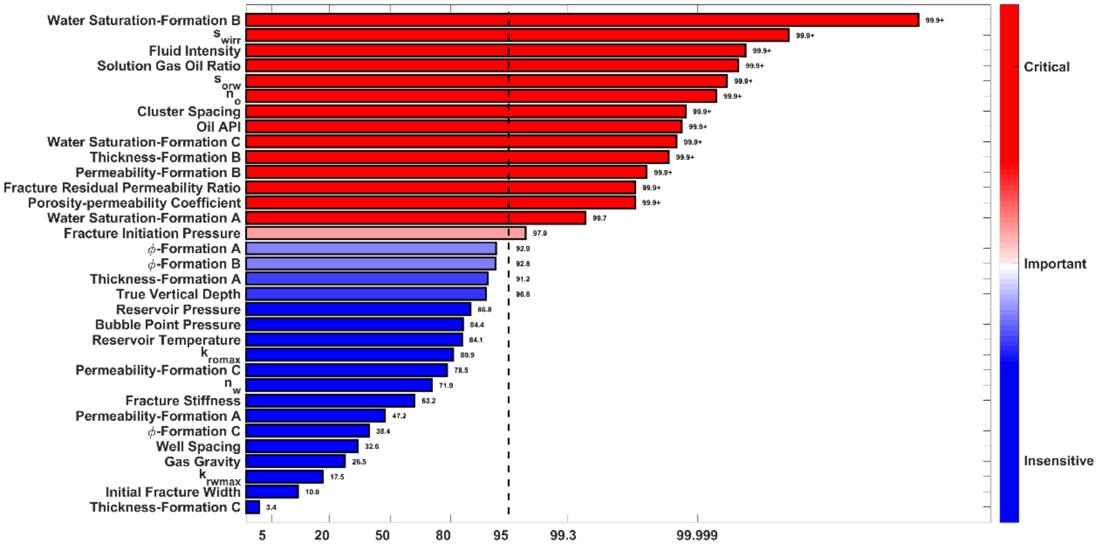

Figure 36. Tornado chart for the sensitivity analysis results

Machine Learning Model Selection and Training

In order to build machine learning models, more than 20,000 reservoir simulation results were generated. We took 2/3 of the simulation results for machine learning algorithm training and 1/3 for model validation. We tried four different machine learning algorithms in *scikit-learn* package in *Python* (Pedregosa et al., 2011) to find the best fit for this particular problem. The algorithm types are summarized in Table 8. We followed the default algorithm setting for preliminary training and validation. For polynomial regression, ordinary least squares linear regression with 2nd degree polynomial features was used. For gradient boosting and random forest regressor, 100 boosting stages and 10 trees were used as number of estimators, respectively. The default setting for multi-layer perceptron regressor was one hidden layer with 100 nodes.

Table 8. Machine learning algorithm types and their default setting

ML algorithms	Regressor type (*sklearn.*)	Regressor setting
Polynomial	*linear_model.LinearRegression*	*PolynomialFeatures(2)*
Gradient boosting	*ensemble.GradientBoostingRegressor*	*n_estimator = 100*
Neural network	*neural_network.MLPRegressor*	*1 hidden layer with 100 nodes*
Random forest	*ensemble.RandomForestRegressor*	*n_estimator = 10*

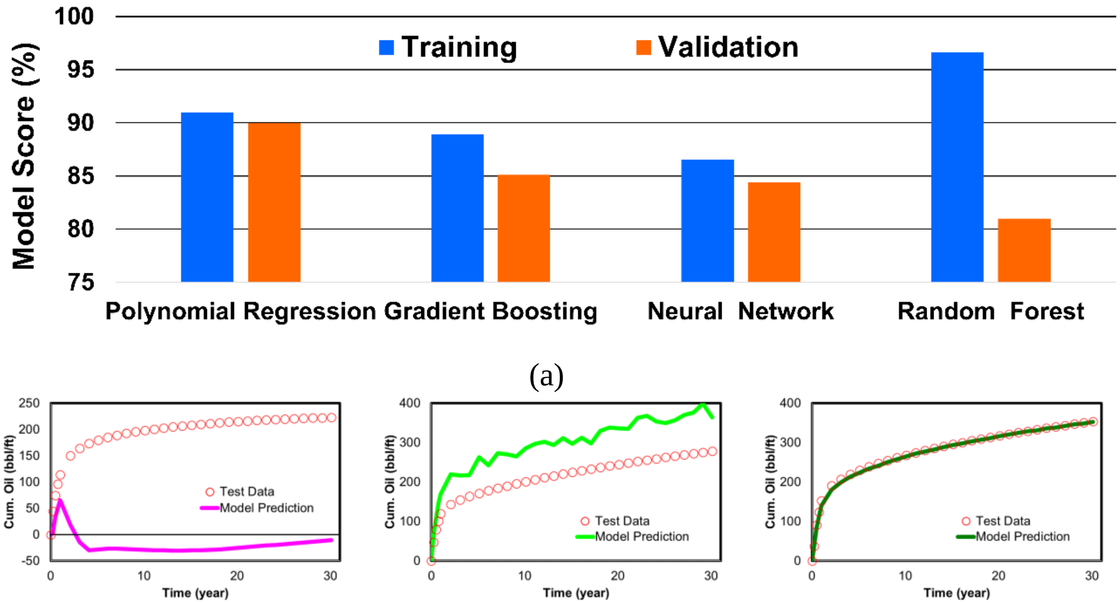

(a)

(b) (c) (d)

Figure 37. Preliminary results of machine learning algorithms: (a) model score comparison and examples of (b) polynomial regression, (c) gradient boosting regression, and (d) neural network regression

Figure 37(a) shows preliminary model scores for training and validation between the algorithms. The model score in y-axis roughly tells the accuracy of the models. The 2nd order polynomial regression shows good results in both training (91%) and validation (90%). However, as Figure 37(b) shows, there are cases showing unrealistic production behavior: cumulative oil production should not be negative. This could happen because the data-driven regression is purely data fitting where underlying physics could be missing. Therefore, in spite of the good model score, the polynomial regression might not be the best fit for this particular problem because it does not adequately reflect the underlying physics in the reservoir simulator. Gradient boosting regression also provides decent scores for training (89%) and validation (85%). However, the predicted production does not increase monotonically (Figure 37(c)). This is because

GradientBoostingRegressor in *sklearn* package only supports multiple-input-single-output type of regression. This means that if we are to predict 30 outputs (e.g., yearly cumulative oil production for 30 years), we need 30 regressors (e.g., one regressor for each year) where each regressor does not necessarily depend on each other. Therefore, it might capture the overall increasing trend but cannot capture the monotonic increasing trend over the period. Random forest regressor shows the highest score in the model training (96%). However, it has an overfitting issue, indicating that there is large discrepancy between training and validation score. Therefore, even though the neural network regressor does not show the best accuracy in the preliminary results, we selected the algorithm because at least it does not show unrealistic behavior. This implies that the neural network algorithm in this case can be potentially used to embed underlying physics between reservoir simulation input and output.

After the neural network algorithm was selected as the machine learning model to train, we tried to find the optimum structure of neural network to improve the model accuracy. Figure 38(a) shows the schematics of neural network structure. The optimum structure was investigated by changing the number of hidden layers and the number of nodes per layer. There is flexibility to assign different number of nodes for each hidden layer and yet in this study, we fixed the number of nodes for each hidden layer. *GridSearchCV* in *sklearn.model_selection* package was used to find the optimum structure of the neural network algorithm. It performs an exhaustive search over specified parameter values for an estimator to help model selection. It involves *k*-fold cross-validation process which means that the entire training dataset (i.e., 2/3 of 20,000+ reservoir simulation results for this study) splits into *k* groups and each group is kept as validation data while the remaining *k*-1 groups are used for training dataset (Schuetter et al., 2018). Thus, the model score after the cross-validation reflects comprehensive evaluation of the model with *k* times of sub-training and validation. In that way, the model is less biased or less optimistic than one-time split for training and validation. Figure 38(b) shows the exhaustive search result for the optimum neural network structure. With all possible combinations of number of hidden layers and nodes, it was found that the best model score comes with 3 layers and 90 nodes per layer for this particular problem.

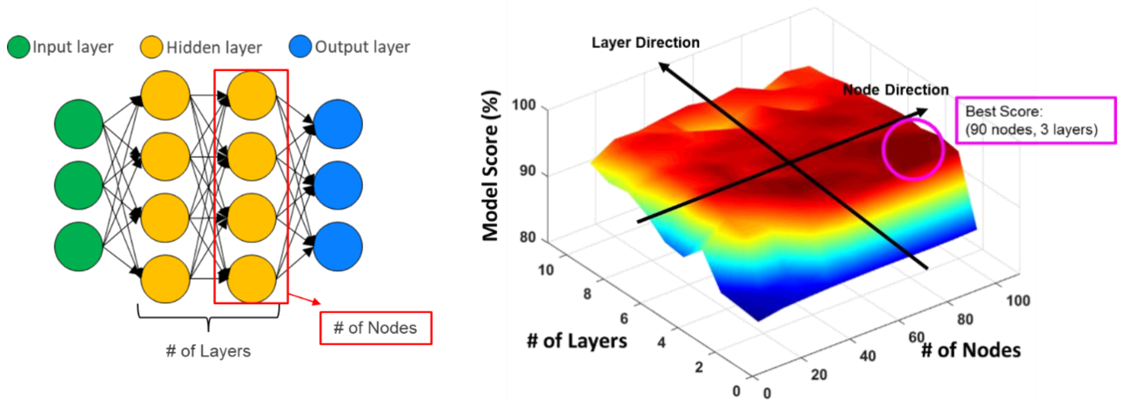

(a) (b)

Figure 38. Neural network model and its score: (a) schematic of neural network structure and (b) neural network model scores with different number of hidden layers and nodes combinations

The exhaustive search is an essential process to improve model accuracy because simply increasing the complexity of neural network structure does not guarantee higher accuracy. For example, Figure 39(a) shows the model score with the number of nodes at six hidden layers. The model score increases rapidly and yet there is not much variation after 30 nodes. Similarly, given 60 nodes per layer, the increase in the number of hidden layers does not provide higher model score (Figure 39(b)). Therefore, the effort should be made to find the optimum structure of neural network model to achieve higher model accuracy.

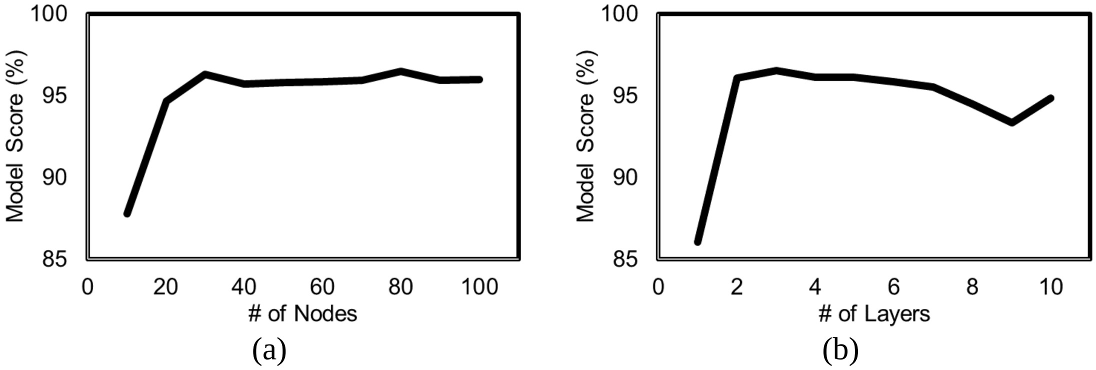

Figure 39. Neural network model score with (a) the number of nodes with 6 hidden layers and (b) the number of layers with 60 nodes

Given three hidden layers and 90 nodes per hidden layer, the model achieved R^2 of 0.96 in the training (Figure 40(a)) and R^2 of 0.94 in validation (Figure 40(b)). Note that all 34 points in the cumulative production profile are included in R^2 calculation and visualization in Figure 40(a)-(b). This means that with the same reservoir simulation input, the trained machine learning model is able to closely reproduce the overall reservoir simulation output, the cumulative production profile. More importantly, we largely benefit from computation time. Figure 40(c) shows the simulation time comparison between the reservoir simulator and the trained machine learning model with y-axis in log-scale. Note that the reservoir simulations were performed with three simultaneous runs using two cores per simulation. We found that the simulation time for the reservoir simulator increases linearly with the number of simulations. However, the simulation time for the machine learning model does not seem to be affected much by the number of simulations. This is because most of simulation time for the neural network model takes in accessing input and writing output. The pure computation for the neural network model is simply a series of multiplication and addition which takes only little time regardless of the number of simulations. With the large number of simulations, the benefit becomes even more magnified. For example, simulating 3,000 cases takes approximately 10 seconds with the machine learning model whereas the reservoir simulator takes about 37 hours. The difference is about four-order of magnitudes. The trained machine learning model is very fast and efficient compared to the reservoir simulator and yet it still provides accurate results which makes the hybrid modeling approach well-suited for field applications.

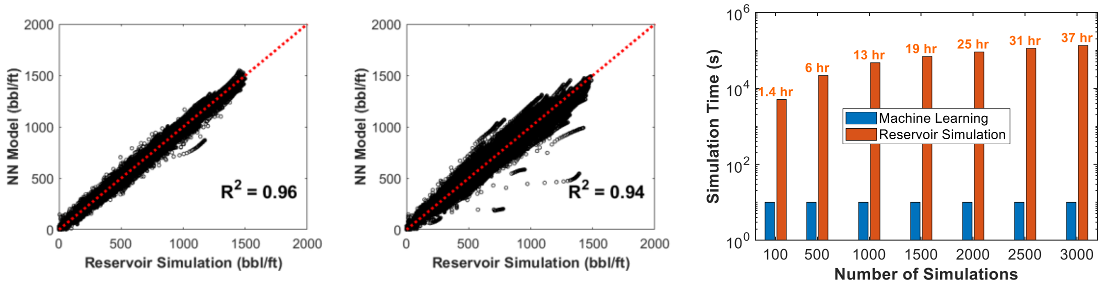

(a) (b) (c)

Figure 40. Comparison between the reservoir simulation results and the trained neural network model: (a) the training result of the neural network model, (b) the test result of the neural network model, and (c) computation time

Well-scale Application

After the hybrid model is built combining physics-based reservoir simulation and data-driven machine learning algorithm, the model was applied at well-scale. The main objective of the well-scale application is to efficiently predict well performance (i.e., cumulative oil production for 30 years). The hybrid model requires three input groups to predict oil production: known parameters, design parameters, and unknown parameters. In order to assess the well performance, unknown parameters need to be identified. Then, we have full control of well performance prediction. After unknown parameters are identified, design parameters sensitivity can be studied which helps field development planning.

To identify unknown parameters, we incorporated the genetic algorithm for history matching so that we can calibrate unknown parameters as history matching parameters. The genetic algorithm is a robust algorithm in the sense that it broadly explores parameter space and it has been widely used for optimization (Iino et al., 2019; Yang et al., 2017b) and history matching (Chen et al., 2020a; Hetz et al., 2017) in oil and gas applications. However, a major bottle neck of the genetic algorithm application is that it requires extensive computation, which is not an issue in the hybrid model. The fundamental idea in the genetic algorithm is the survival of the fittest: models with small misfit (and hence, high fitness) are kept and models with large misfit are discarded so that the entire population moves toward reducing the misfit. In history matching process, the initial population is generated using Latin-hyper cube sampling method. Next, the misfit of each model is evaluated, and the models are sorted by the misfit. The next generation is populated among “good models” from the previous generation with some random input based on cross-over and random mutation. Therefore, as the algorithm evolves, the better solutions are expected so that the misfit gradually decreases. Another advantage of utilizing the genetic algorithm in history matching is that it is a population-based optimization algorithm. Therefore, the genetic algorithm provides an ensemble of history-matched models rather than one deterministic history-matched model. This allows us to assess uncertainty ranges associated with history matching parameters and ultimate oil recovery.

We applied the method to a well in US onshore basin as an example. The history matching was performed, fixing the known parameters and the design parameters for the well. Only unknown parameters are adjusted to minimize the error between history oil production data and cumulative oil production predicted by the hybrid model. Because of the efficiency of the hybrid model, the computation time to complete this single well history matching only takes several minutes with 10 generations where most of time is consumed in mutation and cross-over to populate next generations. The detailed calibration methodology for the sampled well is summarized in Table 9. The history matching parameters are unknown parameters and their ranges are the same as the ranges of reservoir simulation input parameters (Table 10).

Table 9. History matching methodology for the example well

Calibration Algorithm	Genetic algorithm (100 population/generation, total 10 generations)
Calibration Period	1492 days (4 years))
Objective Function	$f(\mathbf{m}) = \sum_{j}^{steps} \left[\ln \lvert \Delta Cum.oil \rvert_{j} \right]$

Table 10. History matching parameters and their ranges for the example well

Category	History Matching Parameters	Parameter Ranges
Dilation/Compaction Curves	Permeability-porosity Coefficient:	20 – 50
	Fracture residual permeability ratio:	5×10^{-3} – 1.0
Relative Permeability	n_o	1.5 – 5.0
	s_{wc}	0.1 – 0.4
	s_{wc}	0.1 – 0.4
Geologic Property	Formation B permeability	1×10^{-4} – 3×10^{-3}

The single well history matching results are presented in Figure 41. Figure 41(a) shows that as the history matching proceeds, the misfit gradually decreases with generations. The models with smaller misfit were selected as updated models based on the horizontal red line. The updated models (Figure 41(c)) show significant improvement compared to the initial models (Figure 41(b)) and closely reproduce the history data. With an ensemble of history matched models, we assessed EUR range for the well and visualized with histogram and cumulative distribution function (CDF) (Figure 41(d)). The EUR ranges from 144bbl/ft to 168bbl/ft with P10 being 157bbl/ft, P50 being 153bbl/ft, and P90 being 143bbl/ft.

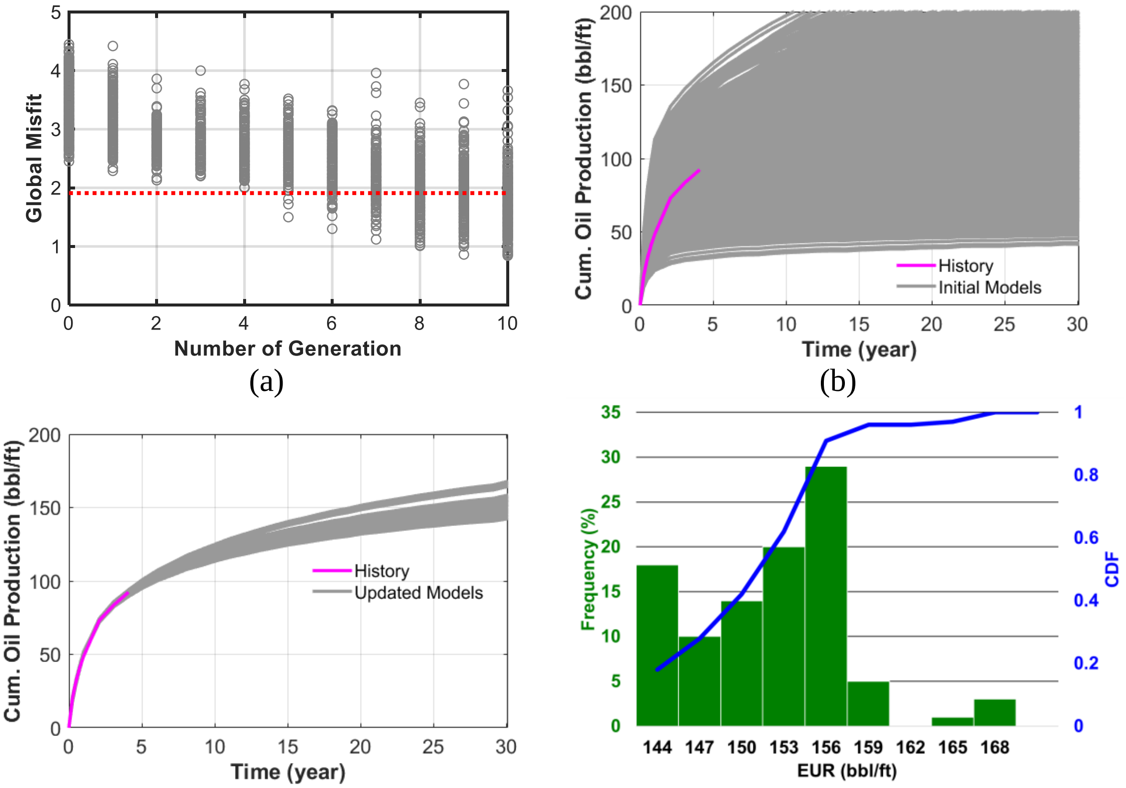

(a) (b)

(c) (d)

Figure 41. Single well history matching results: (a) global misfit vs. number of generations, (b) initial model vs. history data, (c) updated models vs. history data, and (d) histogram and cumulative distribution function of the estimated ultimate recovery

By conducting history matching, we can also calibrate unknown parameters. Figure 42 shows prior and posterior distributions of formation B permeability as an example. Initially, the permeability was uniformly distributed but after history matching, the permeability range is reduced, which means that the uncertainty associated with the permeability decreases. Given calibrated unknown parameters, we have full control of the hybrid model to investigate the optimum field development strategy for this history-matched well. Among three required groups of input parameters (known, design, and unknown parameters), for the optimum field development strategy, known parameters stay identical and we take the calibrated unknown parameters while varying design parameters to investigate the sensitivity of the design parameters on oil recovery and economic matrices.

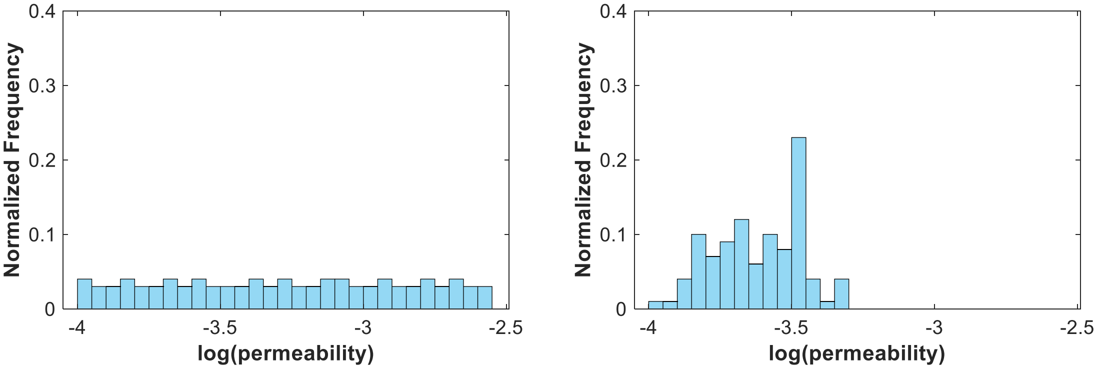

(a) (b)

Figure 42. Formation B permeability distribution for the example well: (a) prior distribution and (b) posterior distribution

We took one of the history-matched models to investigate sensitivity of lateral well spacing and child well effect on oil production. Figure 43(a) shows that the EUR per well increases with larger well spacing. This is because with larger well spacing, the well can drain more reservoir volume and recover more oil. However, EUR per section (Figure 43(b)) suggests that tighter spacing is beneficial in oil recovery while there is no significant difference in the oil recovery until 1,200ft well spacing. This implies that the well spacing tighter than 1,200ft in this area is less effective in terms of oil recovery. This is because given 1,200ft spacing, we can still recover the same amount of oil with a less number of wells.

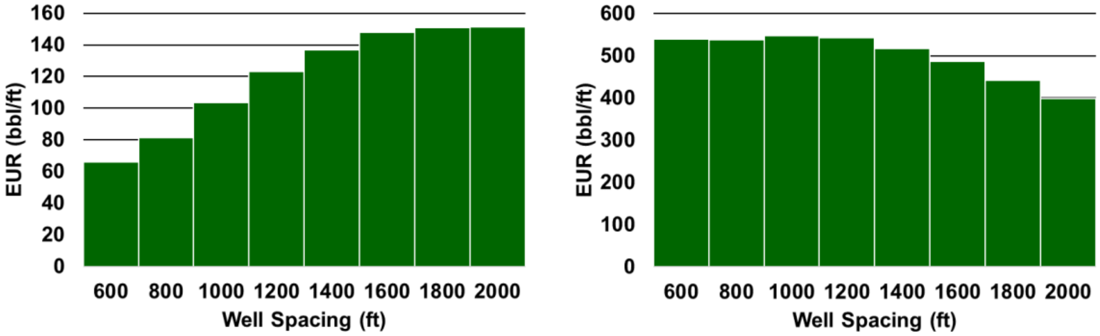

(a) (b)

Figure 43. Lateral well spacing sensitivity on oil recovery: (a) EUR per well and (b) EUR per section

We compared the predictions from the hybrid model with pressure maps from actual reservoir simulations to make sure the predictions are physically making sense. Figure 44 shows cross-sectional pressure maps after 1-year of production from the reservoir simulator at different well spacing. In the case of 600ft spacing (Figure 44(a)), fractures from the parent and child wells are overlapping. In the case of the 2,000ft spacing case (Figure 44(c)), there is large reservoir volume that is not even touched or covered by hydraulic fractures from the wells. However, 1,200ft spacing case ((Figure 44(b)) shows that the fractures are optimally placed in terms of fracture geometry and well spacing. Comparing the hybrid model prediction with the pressure maps from the reservoir simulator, the hybrid model prediction is physically meaningful, capturing the impact of fracture geometry and well spacing on the oil production. This is the significance of the hybrid model and distinguishes itself from pure data-driven approach where underlying physics might be missing.

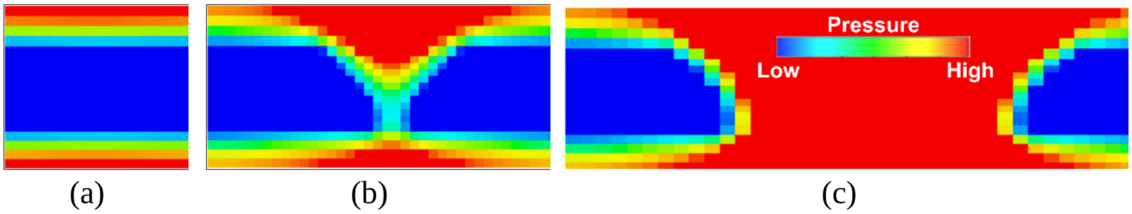

(a) (b) (c)

Figure 44. Cross-section pressure maps from the reservoir simulations at different well spacing: (a) 600ft, (b) 1,200ft, and (c) 2,000ft

Since the hybrid model predicts cumulative oil production as function of time, we can readily calculate economic metrics. The economic assumptions we used for NPV10 calculation are based on typical values of capital expenditure (CAPEX), operational expenditure (OPEX), working interest (WI), and net revenue interest (NRI) in the target basin and summarized in Table 11. Figure 45 shows lateral well spacing sensitivity on NPV10 per well and per section. Figure 45(a) shows that NPV10 per well is basically proportional to EUR per well. However, NPV10 per section suggests the optimum well spacing in the area is around 1,200ft which is consistent with the optimum well spacing for EUR (Figure 45(b)). It should be noted that NPV10 dramatically decreases with the spacing tighter than 1,200ft because tighter spacing means more wells to be drilled and completed which adds up more costs with the same oil recovery volume.

Table 11. Economic assumptions for NPV10 calculation

Parameters	CAPEX	OPEX	Pricing (flat)	WI / NRI
Value	6.5 MM$	12,000 / month Oil: $2.4 / bbl Water: $0.5 / bbl Gas: $1.2 / Mscf	Oil: $50 / bbl Gas: $2.5 / Mscf NGL: $20 / bbl	75% / 100%

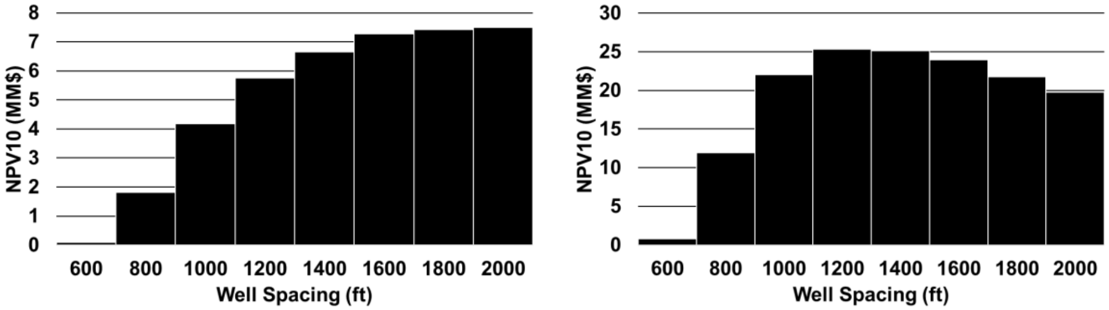

(a) (b)

Figure 45. Lateral well spacing sensitivity on NPV10: (a) NPV10 per well and (b) NPV10 per section

With the history-matched model, we also investigated the sensitivity of child well timing and spacing on oil production degradation. Figure 46 shows performance degradation at different child-well timing and spacing. Given 600ft spacing, the child well performance decreases to 44% with 1-year time lag, 35% with 2-year time lag, and 32% with 3-year time lag compared to the case without time lag (Figure 46(a)). This is because as time lag increases, the reservoir for the child well is more drained by the parent well. Pressure maps from the reservoir simulator confirm that the reservoir for the child well depletes more with longer time lag (Figure 47). Figure 46(b) shows that given 3-year time lag, the performance is less compromised with larger well spacing. With this exercise, the hybrid model demonstrates that the degradation of the child well performance magnifies with longer time lag and tighter well spacing, which is physically reasonable. This implies that the hybrid model captures the child well performance degradation as function of child well timing and well spacing.

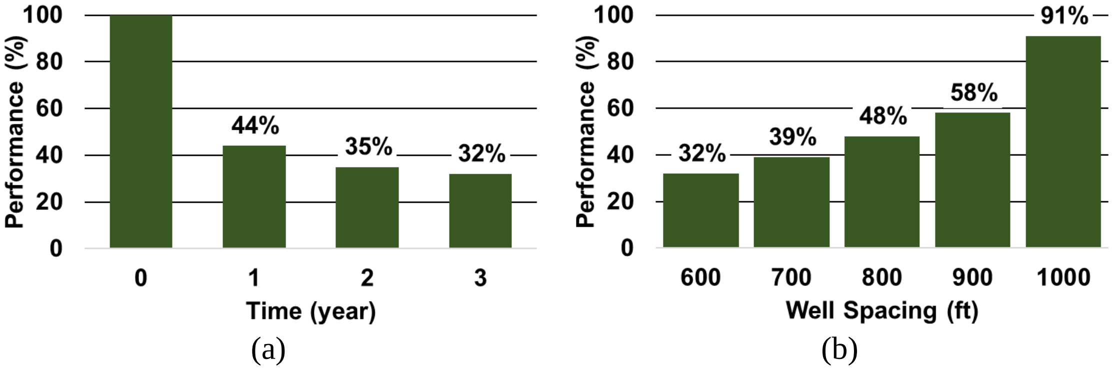

Figure 46. Performance degradation due to child well effect: (a) child well timing sensitivity and (b) child well spacing sensitivity

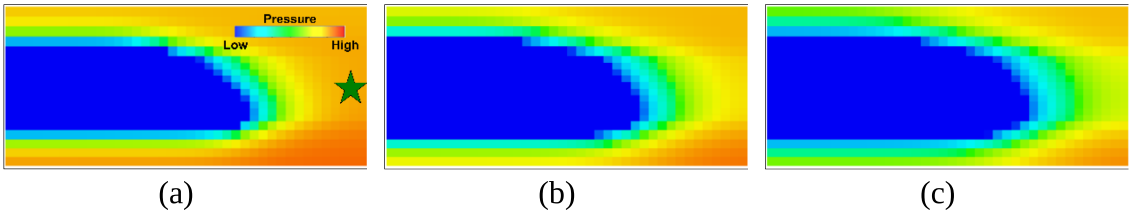

Figure 47. Pressure maps of 600ft spacing case from the reservoir simulations with green star indicating the child well location: after (a) 1 year, (b) 2 years, and (c) 3 years

Lastly, we investigated the sensitivity of completion design on oil production. The fluid intensity indicates the amount of fluid volume to inject to stimulate tight oil reservoirs. Given well spacing, larger injected fluid volume stimulates more reservoir volume, creating larger fracture surfaces area which leads to greater oil recovery. As shown in Figure 48(a), the hybrid model predicts higher EUR per well with larger fluid intensity with 1,500ft well spacing.

Figure 48(b) and Figure 48(c) show pressure maps from the reservoir simulator with the fluid intensity of 30bbl/ft and 50bbl/ft, respectively. With 1,500ft well spacing, 30bbl/ft fluid intensity leaves unstimulated reservoir volume whereas 50bbl/ft fluid intensity stimulates most of the reservoir. This physical interaction between well spacing, fracture size, and fluid intensity is embedded in the hybrid model. The hybrid model suggests that with 30bbl/ft fluid intensity, the maximum EUR per section can be achieved at well spacing around 1,000-1,200ft (Figure 49(a)). This is consistent with the reservoir simulation result that the well spacing tighter than 1,500ft is more effective with 30bbl/ft in terms of oil recovery per section (Figure 48(b)). With 50bbl/ft, the hybrid model indicates the optimum well spacing is around 1,400ft which is close to the reservoir simulation results (Figure 48(c)).

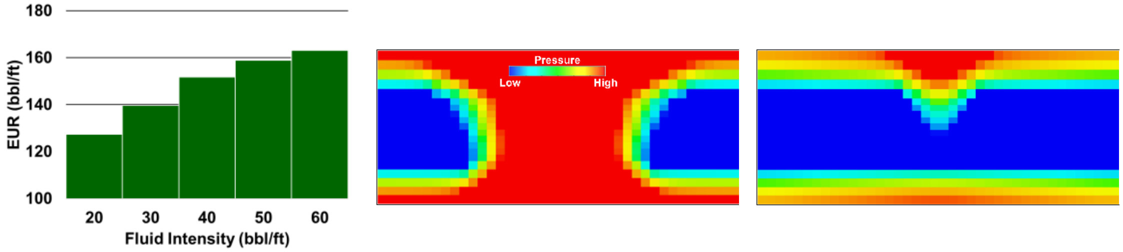

(a) (b) (c)

Figure 48. Fluid intensity sensitivity given 1,500ft well spacing: (a) EUR per well at different fluid intensity, (b) pressure map of 30bbl/ft case, and (c) pressure map of 50bbl/ft case

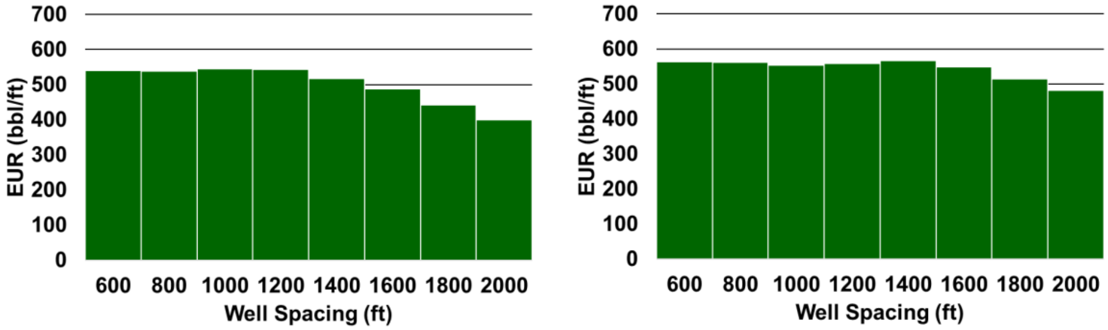

(a) (b)

Figure 49. EUR per section at different fluid intensity completion: (a) 30bbl/ft and (b) 50bbl/ft

Field-scale Application

For field-scale application, the hybrid model generates value acreage maps (e.g., EUR and NPV10) to prioritize well selection in the area of interest and predict well performance in areas where we have not placed a well yet. In order to generate value acreage maps, handful of wells were history-matched. Figure 50(a) shows the locations of the history-matched wells in the area of interest. The EUR and NPV10 for each well were assessed with single-well history matching, discussed in the previous section. Given EUR and NPV10 at multiple locations, values were populated over the area of interest. In this study, inverse distance weighted average was used to populate values in demonstrating the workflow. However, other geostatistical methods such as Kriging can be utilized to improve generating the value acreage maps. The area of interest (11km×20km) is meshed with 100×100 and value for each cell is calculated by

$$x^* = \sum_{i}^{n-locations} \frac{w_i x_i}{w_i}, \tag{10}$$

where x^* is the unknown value at a location to be determined, x_i is known value at i^{th} locations, and w_i is the weight which is inverse distance, $w_i = 1/\left|d_{ix^*}\right|^p$. The variable p is for the power function to account for the decrease in weight with distance.

Figure 50(b) and Figure 50(c) show populated EUR and NPV10 maps, respectively. These maps would be helpful as a screening process if a quick decision needs to be made for the field development in this area. For example, if EUR or NPV10 need to be maximized in this area, these maps can help prioritize locations to place wells for future development.

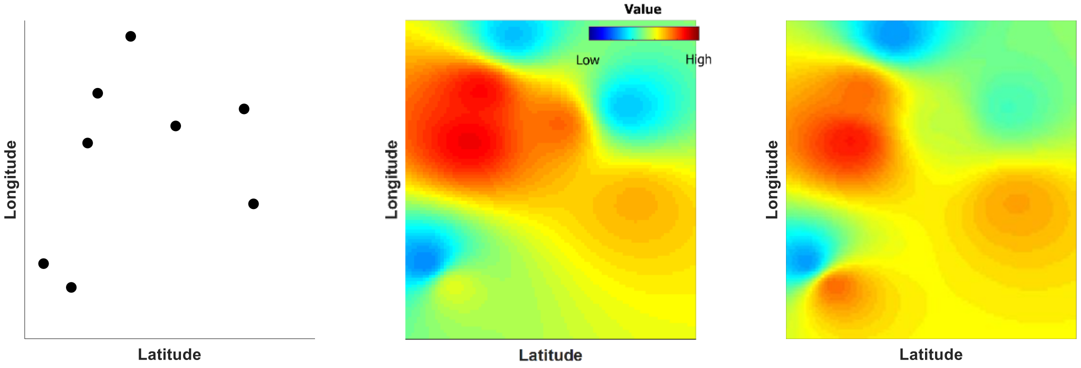

(a) (b) (c)

Figure 50. Examples of value acreage map (11km×20km): (a) history-matched well locations, (b) populated EUR map, and (c) NPV10 map

Another field-scale application of the hybrid model is to predict oil production at potential well locations. The ultimate goal of utilizing the hybrid model is to assess well performance of incoming well by changing design parameters so that the model can suggest the optimum development and completion strategy in the area. Like any kind of reservoir simulators, the hybrid model is a forward-simulator and can provide well response (i.e., cumulative oil production) as long as input is prepared. The challenge here is to obtain unknown parameters in the input. Previously, single-well application showed that unknown parameters can be calibrated by history matching if production history data is available. However, constraining unknown parameters at locations without the well response is not straightforward. In the current study, we use calibrated unknown parameters at history-matched well locations and take inverse distance-weighted average to calculate unknown parameters at potential well locations where we want to predict the well performance.

To validate the idea, we conducted a blind test. The purpose of the blind test is to demonstrate if the hybrid model can provide a reasonable prediction for the area that we do not have wells, specifically for the area that we do not have unknown parameters. Figure 51(a) highlights the blind test location with the magenta star. Note that the location is encompassed with the adjacent history-matched wells. The known parameters in the locations such as initial reservoir conditions, geologic properties and fluid PVT are given. The design parameters are extracted from the blind-tested well completion. The unknown parameters for this location are interpolated using the history matching results from the adjacent wells. Figure 51(b) shows the comparison between production history of the blind-test well and predicted oil production by the hybrid model. It is shown that the hybrid model closely reproduces the history data. This means that if we can identify unknown parameters of any location in the basin from the history matched results of adjacent wells, then we have a full control of well performance prediction over the entire basin. Referring to Figure 40(c), we can simulate 3000 cases at different completion designs for only 10 seconds which eventually help us to find the optimum field development strategy with great efficiency. Also, this is meaningful in cost saving manner. We spend a lot of resources and effort for data acquisition to better predict well performance. However with this workflow, we can still predict well performance in the area that we do not have sufficient data to make prediction. This is because we can measure the input parameters but we can also calibrate the parameters by history matching.

The EUR predicted by the hybrid model is about 129bbl/ft. We tried DCA to predict EUR as a reference. The predicted EUR by DCA is about 140bbl/ft which is close to the hybrid model prediction (Figure 51(c)). However, the critical difference between the hybrid model and DCA is that DCA requires production data to fit whereas the hybrid model can predict well performance even before the production starts. The blind test demonstrates that once we identify unknown parameters at any location using adjacent history matching results, and we know how a well is going to be completed, then we can predict yearly cumulative oil production.

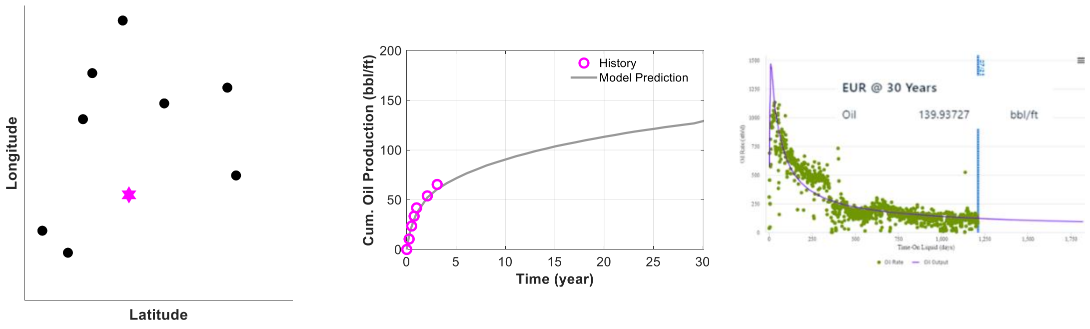

(a) (b) (c)

Figure 51. Blind test for the hybrid model: (a) location of the blind test well, (b) comparison between the history data and the hybrid model prediction, (c) DCA for the blind-test well

Discussion

With a growing interest in data-driven approach, there have been many efforts to apply machine learning models to predict well performance in unconventional reservoirs. As Schuetter et al. (2018) well-established, the data-driven modeling is efficiently used to predict unconventional reservoir performance and the industry has been adopting it especially for the last several years. However, there are critical questions to be addressed for a pure data-driven model, a black box model without underlying physics, to be genuinely effective. First of all, the data quality needs to be insured. This might not be always the case in the oil and gas applications where most of the data is from subsurface with inevitable noise and uncertainty. Also, the data used in the training process should be representative for application. For example, it is questionable that a machine learning model based on well data from 5-10 years ago would be useful to evaluate well performance that is recently completed, as the completion practice and well configuration have been dramatically changing. This is not an issue of the number of training data points and yet a matter of the fact that the training data points should have adequate coverage. As Ertekin and Sun (2019) pointed out, the validity of the extrapolation results would become diminished, if the input data outranges the training dataset, also observed in other subsurface engineering applications (Jo et al., 2020; Santos et al., 2020). In reality, it is difficult to obtain a large volume of field data with fairly uniform parameter distributions to build a powerful and universal data-driven model. Moreover, a data-driven model needs to honor physics to some extent and be interpretable in a physical way such that users other than the developers can utilize.

The presented hybrid modeling tries to address those challenges while taking advantage of efficient computation in the pure data-driven approach. In the hybrid modeling, the training data set is generated based on physics-based reservoir simulations. The simulation input parameters are sampled using Latin hypercube sampling to cover parameter spaces effectively. We tried to maximize the accuracy of the machine learning model by exhaustive search of the optimum structure thus the hybrid model can naturally capture physical phenomenon, closely reproducing the reservoir simulations. This is similar to how Lu et al. (2017) embeds physics in their neural network model. They modified the structure of the neural network model to feature physical interaction between input and output based on the domain knowledge, improving the accuracy of the neural network model.

The potential improvements in the current hybrid modeling includes the flexibility of well constraints. The current model fixes the BHP decline trend. Therefore, the applications might be limited to wells without long-term shut-in. In order to have pressure and saturation distributions with flexible well constrained and responses (e.g., water cut and gas oil ratio), physics-informed machine learning approach can be considered in the future, where the lost function in machine learning models combines mean squared error and physical constraints from the governing process (Tchelepi and Fuks, 2020). The assumption of identical fracture geometry and permeability for parent and child wells can be potentially relaxed as the fracture propagation of the child well can be different than that of the parent well due to the stress field change after the reservoir of the parent well is depleted (Guo et al., 2019; Liu et al., 2020).

Conclusion

Unconventional field development and the pace of operations require new ways of modeling well performance beyond traditional tools. Lack of understanding of underlying physical mechanisms, limited availability and high cost of inputs required to characterize the reservoirs and the speed of the model-based decision support are some of the key problems that must be overcome. There are no viable options in current practices in unconventional field developments that can serve both fidelity and speed simultaneously.

Considering limitations in practices, a hybrid model combining physics-based reservoir simulations and data-driven machine learning algorithms has been developed for unconventional field development. More than 20,000 reservoir simulation cases which include both injection and production phases of hydraulically fracture wells were generated to train the machine learning algorithms. Among multiple machine learning algorithms, the neural network model was found to be a good fit for reflecting underlying physics in reservoir simulations. We maximized the neural network model accuracy, R^2 of 0.94 for the model validation, by exhaustive search for the optimum neural network structure. The hybrid model, underlying physics-embedded machine learning model, was incorporated with history matching algorithm for production forecasting and unknown parameter calibrations. After the model calibration, the hybrid model assessed well performance at different design parameters to help find optimum development strategy. It was shown that the model captures the interaction between wells including parent-child and the impact of completion design and well spacing on oil production. For the field-scale application, value acreage maps which can help prioritize well selection, were generated with multiple history matching results. To show that the hybrid model is predictive in the area of interest, the blind test was conducted, demonstrating that interpolated unknown parameters from multiple history-matched locations can be used to assess potential incoming well performance. The proposed workflow can be extended to a larger area with other aspects in unconventional field development such as stacked well configuration with multi-well history matching.

The proposed method is a pragmatic way to achieve speed while still keeping the method physically intuitive and interpretable and of high fidelity. On top of that, the method seamlessly scales from the well level to the field level and keeps up with the pace of operations of the unconventional field development, even in the absence of ubiquitous data collected for each well. Therefore, the method maximizes the return on investment on data acquisition programs and also reduces CAPEX for new well costs.

CHAPTER IV

DETAILED FAULT MODELING AT AZLE AREA AND SITE-SPECIFIC SEISMOLOGICAL MODEL TO ASSESS POTENTIAL INDUCED SEISMICITY

Chapter Summary

The objective of this study is to investigate the mechanisms of earthquakes observed in Azle, North Texas in 2013-2014 using one-way coupled fluid flow and goemechanical simulations. The simulation results then were compared with observed earthquakes to quantitatively assess potential seismicity in the area, given operating conditions of produced water disposal and hydrocarbon production. The detailed fault modeling was realized by representing the faults as discontinuous surfaces in the geomechanical simulation model and incorporating seismic interpretation of the faults by the operator. A wide range of data has been incorporated to build the simulation models with geologic features of the area, including formation horizons, fault picks from seismic survey by the operator and 72 injectors/producers. The flow model was first calibrated by history matching injectors' bottom-hole pressure, producers' tubing head pressure and gas production rates. The calibrated pressure distributions were updated into the geomechanical simulation model to assess fault slips and resulting fault frictional energy. We used the alternating conditional expectation (ACE) algorithm to build a correlation between the incremental frictional energy and observed earthquakes with the magnitude larger than 1.5. The correlation is used to examine potential induced seismicity events

given the operating conditions. The calibrated simulation results showed that the pressure change in the reservoir did not propagate to the basement, while fault slips propagated to the deep basement. This suggests that the poroelastic effect was the driving mechanism of the earthquakes in the basement. The ACE algorithm found the maximum correlation between the energy and the earthquake frequency and suggested that frequent earthquakes are not expected with current operating conditions. This is mainly because the production will keep decreasing as the reservoir gets depleted and the disposal well will be managed to maintain the injection level low. The presented workflow which integrates large volume of field data provides a systematic and robust analysis of earthquake frequency prediction to assess and manage potential risks associated with fluid-induced seismicity.

Introduction

Anthropogenic fluid activity might induce or trigger earthquakes, changing pore pressure and/or stress on faults plane. Although the change in pressure and stress is not independent, it is commonly understood that there are two main mechanisms associated with such earthquakes (Bao and Eaton, 2016; Ellsworth, 2013; Elsworth et al., 2016; Keranen and Weingarten, 2018; McGarr et al., 2002). The first mechanism is the decrease in effective (grain) normal stress with pore pressure increase on the fault plane. This is the case when pressurized fluid directly interacts with the fault and the effective normal stress decreases by Terzhaghi effective stress law. The other mechanism is so called poroealstic effect based on Biot's theory of linear poroelasticity. The fluid injection or extraction away from faults can alter loading conditions on the faults without direct hydrologic connection, which can explain seismicity events beyond direct fluid injection or extraction zone (Segall, 1989). While the first mechanism has been dominant as the primary mechanism to destabilize pre-existing faults due to fluid interaction (Goertz-Allmann et al., 2011; Keranen et al., 2013; Langenbruch et al., 2018; Raleigh et al., 1976), there is a growing understanding and investigations of the second mechanisms to bring more insights into fluid-induced seismicity (Chang and Segall, 2016a; Chang and Segall, 2016b; Segall et al., 1994; Segall and Lu, 2015).

There has been an increase in seismic event frequency in the Fort Worth Basin (FWB) for the last decade which could be linked to anthropogenic fluid activity. The frequency of earthquakes with magnitudes greater than 3 escalated about six times since 2008 (Frohlich et al., 2016). The seismic events in the metropolitan area attracted attention because there has been active fluid extraction from the Barnett, a hydrocarbon-rich shale formation, and disposal water injection to the Ellenburger, a huge carbonate aquifer below the Barnett. There is an existing body of studies to investigate the causal factors of the earthquakes and the most draw conclusion that there is possible relationship between the disposal water injection and the seismic events. For example, Hornbach et al. (2016) made statistical comparisons between wastewater injection, time, subsurface pressure and seismicity in FWB, incorporating more than 24,000 monthly injection volume and pressure measurements for Ellenburger formation. They showed a correlation with large injection volume and seismicity events in space and time, which is consistent with observations in previous seismicity studies associated with wastewater injection in DFW (Frohlich, 2012; Frohlich et al., 2016; Gono et al., 2015). Some studies included stress components in the analysis. Zhai and Shirzaei (2018) employed coupled linear poroelastic model to simulate the spatiotemporal evolution of pore pressure and poroelastic stress. They found that the contribution of poroelastic stresses is less (~10%) compared to pore pressure in Coulomb failure stress change, a criteria for fault slip. Hennings et al. (2019) used updated stress maps from Snee and Zoback (2016) to assess fault-slip potential (Walsh et al., 2017) in FWB integrating detailed fault map, well logs, and outcrop characterization. Given uncertainty ranges, their analysis shows most faults in FWB are highly vulnerable to reactivation subject to injection operations.

The Azle area, the area of interest in this study, experienced a series of earthquakes between late 2013 and early 2014 with the maximum magnitude larger than Mw3. Previous two site-specific studies utilized numerical simulations to understand the mechanism of the Azle earthquakes incorporating 70 gas producers and two injectors in the Barnett and the Ellenburger, respectively. Hornbach et al. (2015) built a single-phase flow model and found that with different parameter combinations, it is possible that pore pressure at the fault could exceed up to 0.14MPa. They found the pressure increase could propagate to the basement through highly conductive fault and lead to sufficient reduction in the effective normal stress to reactivate a critically-stressed fault (Reasenberg and Simpson, 1992; Stein, 1999). Based on the detailed review of the area and provided data by Hornbach et al. (2015), Chen et al. (2020b) investigated the Azle area using coupled fluid flow and geomechanical simulations including the entire computational domain, from the overburden to the basement, to investigate actual stress and pressure change in the basement. The model was calibrated integrating injectors' bottom-hole pressure (BHP) and earthquake magnitude and showed that sufficient plastic strain can be accumulated in the basement compared to the observed earthquakes without direct fluid interaction in the basement. The deformation in the basement was mainly owing to the poroelastic effect caused by unbalanced loading in the reservoir where injection and production is mainly dominant in northwest and southeast across the faults, respectively.

The motivation of the current study is to revisit the Azle area with detailed fault modeling and build a predictive model for seismicity events to assess potential risks associated with oil and gas operation conditions. There are mainly two improvements in terms of fault modeling compared to the previous study (Chen et al., 2020b). The first improvement is the fault geometry. In the previous study, the faults were built as flat planes based on single dip and strike data from the literature (Hornbach et al., 2015) and earthquake locations (Railroad Commission of Texas, 2015a; Railroad Commission of Texas, 2015b). However, the fault geometry for the current study was provided by the operator based on the seismic survey. This significantly reduces uncertainties associated with fault locations and orientations in the previous studies. Second improvement is the representation of the faults in the geomechanical simulation model. In the previous study, the faults were represented as grid cells with distinct properties (e.g., low cohesion value), compared to other formation cells. The current study represents faults as discontinuous surfaces which can explicitly calculate displacement along the fault surface (Jha and Juanes, 2014; Rutqvist et al., 2016; Urpi et al., 2016). In order to capture the slip along discontinuous surfaces, we employed CMG-ABAQUS one-way coupling simulations. Figure 52 shows the overall workflow. The workflow starts with Petrel to create a detailed Azle geologic model including faults, horizons and wells. Next, based on the geologic model, we build a flow simulation model and a corresponding geomechanical simulation model. When it comes to numerical simulations, our focus is first on the CMG model. We calibrate the CMG model by history matching injectors' and producers' well responses. The calibrated pressure distribution in the CMG model is then updated into the ABAQUS model. Given the calibrated pressure, we proceed to ABAQUS simulations and assess slip and resulting fault frictional energy, which is correlated with observed seismic events to build predictive seismological model. Unlike previous studies where the seismic events were correlated with wastewater injection volume, our workflow finds a direct relationship between the seismic events and the fault frictional energy from the geomechanical simulations. This makes the workflow more robust in the sense that it adds the mechanistic component by numerically solving the momentum balance equation over the entire simulation model in response to disposal water and hydrocarbon operations.

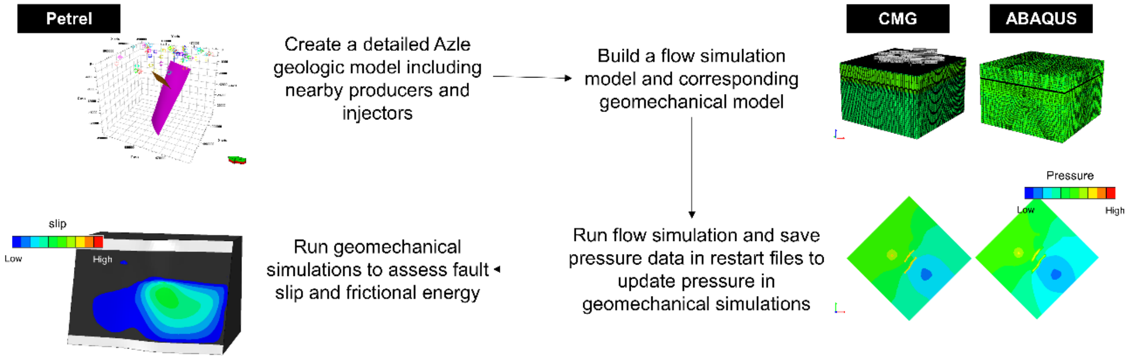

Figure 52. Workflow for one-way CMG-ABAQUS coupling simulation to assess fault slip

Model Input Data Review

A wide range of data, including injectors, producers, faults, and horizons has been integrated to build flow and geomechanical simulation models. Two conjugated Azle faults and horizons for each formation, Marble falls, Barnett, Ellenburger and the crystalline basement, were provided by the operator. Well information, including location and rates, was either from literature and public data base, or was provided by the operator. The locations of 70 producers and two injectors are from (Hornbach et al., 2015). Two injectors' rate and tubing-head pressure (THP) data are available in H-10 form in Railroad Commission of Texas website (Railroad Commission of Texas, 2019a). The gas and water production rates are from public records (Railroad Commission of Texas, 2019b), database (Enverus, 2019) and some of producers' THP are provided by the operator. Figure 53(a) shows the well locations, Barnett horizon, faults and simulation model coverage (12km×12km). Because the provided horizon is only part of the simulation model coverage, the horizon had to be extended. We found that there is not much variation of depth, less than 100m, in the provided horizons, thus we simply took the average depth of each horizon and assumed that horizons are flat over the simulation domain (Figure 53(b)). The average depths for formations tops are 1702m, 1800m, 1900m, 3007m, for the Marble Falls, the Barnett, the Ellenburger and the basement, respectively and the simulation model extended vertically to 8km deep.

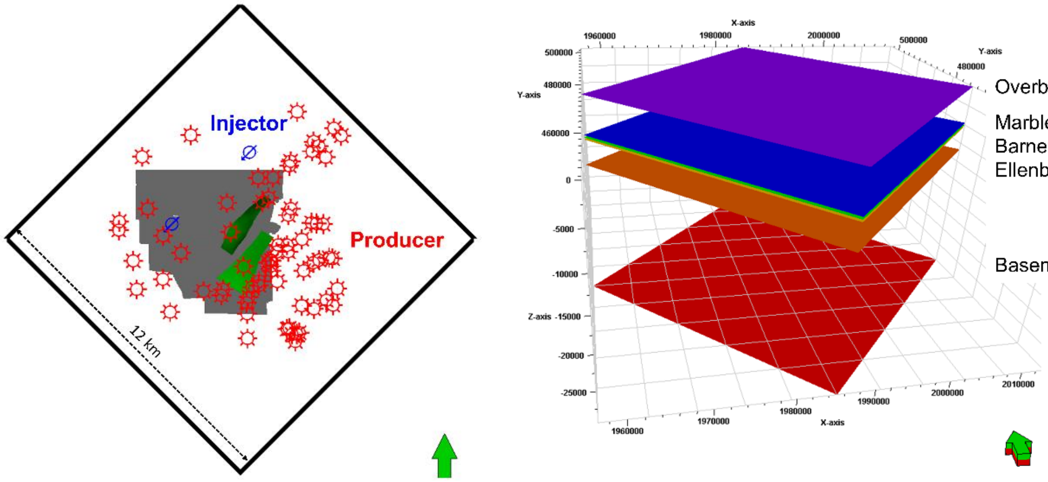

(a) (b)

Figure 53. Provided formation horizons: (a) horizon and simulation model coverage and (b) horizon representation in the models

There are two conjugated faults in the Azle area. The main fault extends from the Barnett to the deep basement while the antithetic fault only covers the Barnett and the Ellenburger (Hornbach et al., 2015). The operator-provided fault picks, based on the seismic survey, were originally rough. Therefore, we had to sufficiently refine the original data to generate relatively smooth fault surfaces so that the surfaces can be incorporated in simulation models. Figure 54 shows the original faults picks and earthquake locations from the North

Texas earthquake catalog study (Quinones et al., 2019). The provided fault surfaces are consistent with the earthquake locations. In addition, we can see that the earthquakes mainly started from the basement (Figure 54(a)) and also larger earthquakes were recorded in the basement (Figure 54(b)).

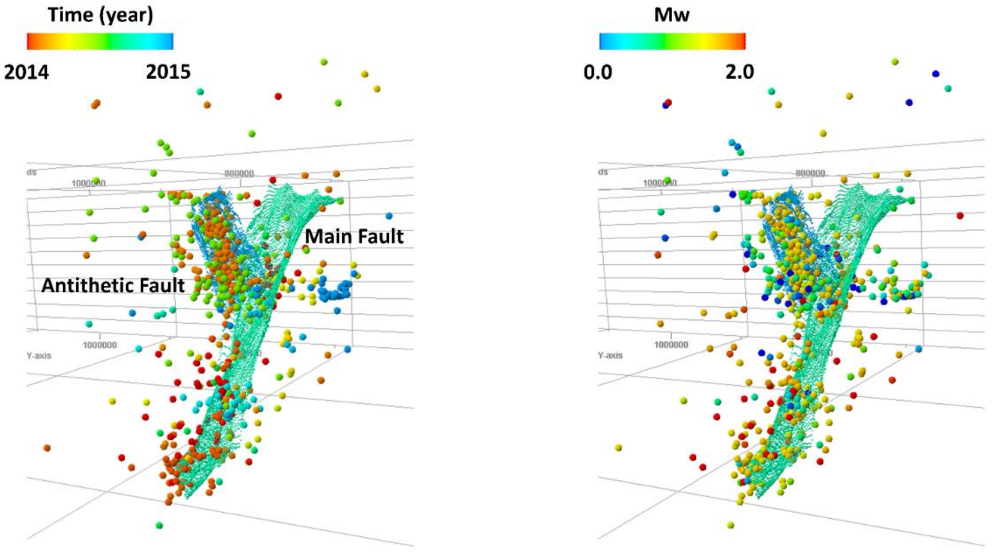

(a) (b)

Figure 54. Azle faults and earthquake locations: (a) earthquake record time and (b) moment magnitude

With the provided fault picks, fault surfaces were generated and smoothed in Petrel to properly mesh the simulation models. Figure 55 shows the procedure of importing fault picks into CMG and ABAQUS simulation models. Meshing CMG model is relatively straightforward. Structured gridding in Petrel can be directly transferred to CMG platform using RESCUE format. However, meshing ABAQUS model involves multiple steps including format conversion in SOLIDWORKS. It requires iteration process because we ideally want to preserve the original geometry of the faults in the simulation model while

ABAQUS mesh cannot resolve high roughness and complexity of the original faults. Therefore, we first sufficiently smooth the faults in Petrel to be incorporated in ABAQUS model. Next, we imported the faults in Petrel to CMG model to make sure the fault geometry is consistent in both simulation models. The implication of Figure 55 is that any fault geometry from field measurements can be incorporated into the flow and geomechanical simulation models, capturing detailed features of the faults in the analysis.

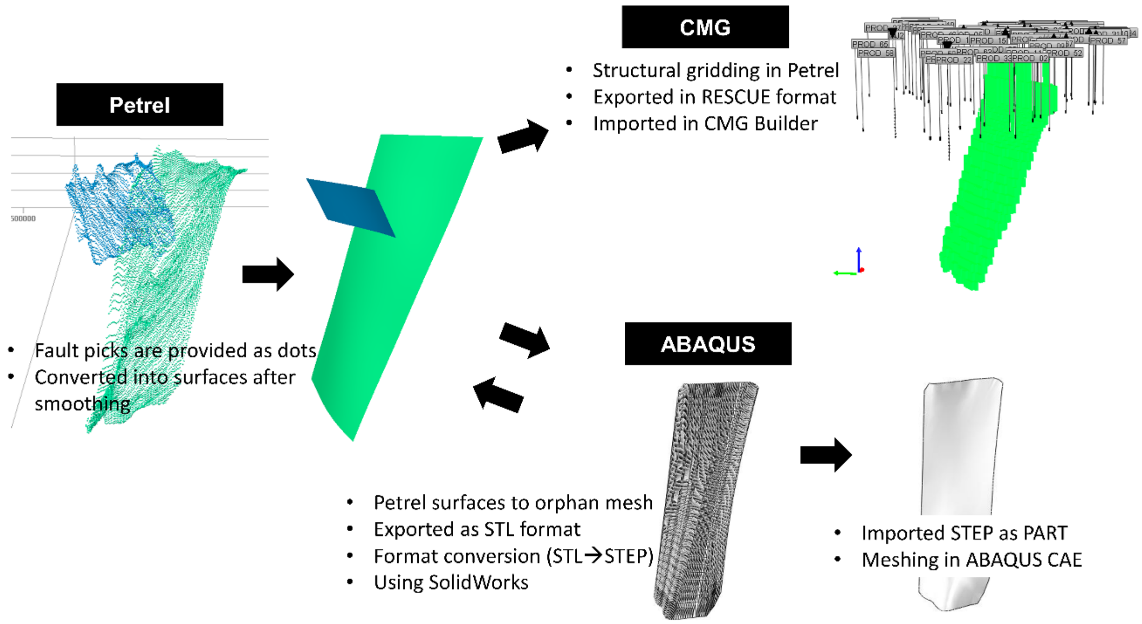

Figure 55. Procedure of incorporating faults into simulation models

The final main (purple) and antithetic (dark blue) fault configuration for the simulation models are shown in Figure 56(a). The median value of dip angle and azimuth for the main and antithetic faults are 68°, 310° and 61°, 125°, respectively. The main fault is steeper than the antithetic fault. However, the strike direction of those two faults are almost parallel except that the main fault is dipping to northwest whereas the antithetic fault is dipping to southeast. This implies that given the median dip azimuth and assuming normal faulting stress regime, the most favorable maximum horizontal stress direction for the main and antithetic faults to slip (the vertical and the minimum horizontal stress plane) would be 40° and 35° from the north to the east, respectively.

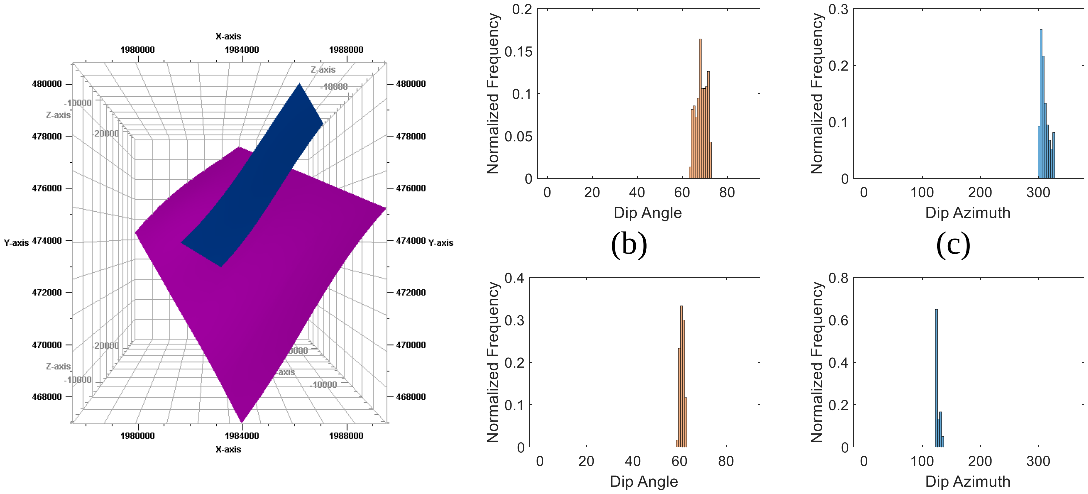

(b) (c)

(a) (d) (e)

Figure 56. Final faults geometry for simulation models: (a) fault representation in Petrel, histogram of (b) the main fault dip angle, (c) the main fault dip azimuth, (d) the antithetic fault dip angle, and (e) the antithetic fault dip azimuth in degree

The in-situ stress is critical input as well as the fault configuration in the analysis because the stress and the fault plane together determine the fault criticality. In regards to principal stress data, Hennings et al. (2019) subdivided the Fort Worth Basin into four stress areas of relatively constant stress conditions, mainly the maximum horizontal stress direction and relative stress magnitude. According to their analysis, the Azle area belongs to the stress area 2. Table 12 lists the initial stresses, maximum horizontal stress direction, pore pressure and associated uncertainty in the stress area 2. The relative principal stress magnitude can be quantified with A_ϕ, which is

$$A_\phi = (n+0.5) + (-1)^n \left(\frac{(S_2 - S_3)}{(S_1 - S_3)} - 0.5 \right) \quad \begin{cases} n = 0 \text{ for normal faulting} \\ n = 1 \text{ for strike-slip faulting} \\ n = 2 \text{ for reverse faulting} \end{cases} \qquad (11)$$

where S_1, S_2, and S_3 are the maximum, intermediate and minimum principal stress magnitude, respectively (Simpson, 1997). From Table 12, the initial setting for the simulation models take 26.01MPa/km, 25.55MPa/km, 14.20MPa/km, and 10.65MPa/km for the vertical, the maximum and minimum horizontal stresses, and pore pressure, respectively.

Table 12. Stress, pressure and fault parameters and their uncertainty for the Azle area (after Hennings et al. (2019))

Base Value							Uncertainty Range	
Shmax Azimuth (°)	A_ϕ	Friction coefficient	Pp (psi/ft)	Sv (MPa/km)	Shmax (MPa/km)	Shmin (MPa/km)	Shmax azimuth (MPa/km)	A_ϕ
32	1	0.7	0.471	26.01	26.01	14.20	16	0.22

Given the principal stresses, we can project the in-situ stress onto the main fault plane using tensor transform (Lee et al., 2012) and see how critically-stressed the fault is. After the tensor-transformation, the stress state of each point in the fault plane is represented in the dot in Mohr circle diagram. Figure 57(a) shows the 3D Mohr circle diagram and coulomb failure envelop, assuming friction coefficient of 0.7, at 3,000m, close to the boundary of the Ellenburger and the basement. The color code in the figure indicates the horizontal distance between the stress state and the failure enveloped ($\Delta\sigma_n^{'}$), which is also referred as critical pore pressure, the pore pressure increase required to cause fault slip (Chang, 2017; Wiprut and Zoback, 2000). Each point in Figure 57(a) corresponds to stress state of discretized main fault plane (Figure 57(b)). The stress projection confirms the well-known fact that the Azle faults are critically-stressed (Snee and Zoback, 2016), very favorable for the slip, and even some part of the main fault is above the failure envelop. The geomechanical simulator corrects such unphysical stress state, allowing initial slips for these areas during the equilibrium step. Therefore, the actual initial stress state for the geomechanical simulation is realistic, below the failure envelop (Byerlee, 1978).

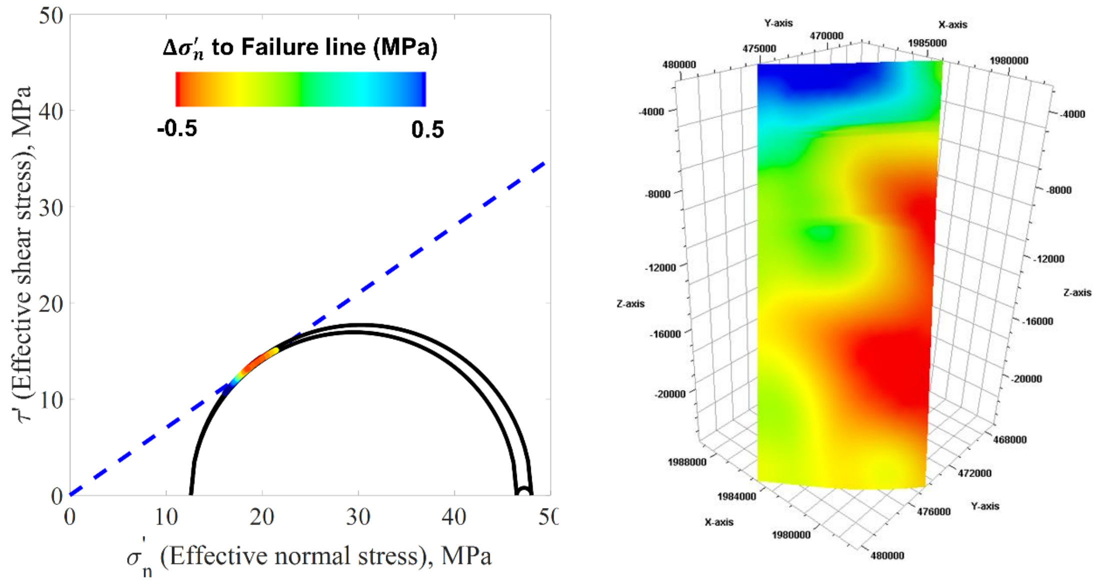

(a) (b)

Figure 57. Initial stress state and fault geometry: (a) Mohr-circle diagram with the initial effective stress and the projected stress and (b) initial stress projection onto the main fault plane

Simulation Models

Flow simulations in this study were performed in CMG IMEX, a black-oil forward simulator. The flow simulations provide the calibrated pressure distributions to the geomechanical simulations to assess fault slip evolution. The multiphase flow simulator discretizes the continuity equation in the finite difference scheme and solve for pressure and saturation of phases. Given initial pore pressure, flow properties and operational constraints, the simulator computes pressure and saturation distributions as well as local well responses, following the mass conservation principle. The continuity equation for the fluid flow in porous media is given by

$$\nabla \cdot \left[k_o k_f \frac{\rho_f}{\mu_f} \left(\nabla p_f - \rho_f g \right) \right] = \frac{d\left(\phi \rho_f\right)}{dt} + Q_f \, , \tag{12}$$

where k_o is the intrinsic permeability, g is the gravitational acceleration, and ϕ is the porosity. The subscript f indicates phase, k_f is the relative permeability, ρ_f is the fluid density, and Q_f is the source/sink term for phase f .

The flow simulation model consists of 736,196 cells ($134 \times 134 \times 41$) and contains 72 wells. Two of them are injectors, perforated in the Ellenburger and the rest of them are producers, perforated in the Barnett. The initial pore pressure gradient is 10.65MPa/km and the faults in the CMG model are represented by a set of grid cells thus the faults have zig-zag configuration in the model (Figure 58(a)). The flow simulation starts from 2005 and ends in 2020. Table 13 summarizes permeability and porosity of formations as flow simulations input based on Chen et al. (2020b). In the Barnett shale, we put high permeability at producers to represent hydraulic fractures. The hydraulic fracture penetrates to the bottom of the Barnett, contacting with the Ellenburger in the model because the fracturing operation in the thin Barnett formation might put in direct communication between the Barnett and the Ellenburger (Nicot, 2009). The hydraulic fracture and Ellenburger permeability are part of the history matching parameters and they are to be adjusted during model calibration process.

The geomechanical simulator numerically solves the quasi-static momentum balance equation using the finite element discretization scheme. The governing equation for the geomechanics is

$$\nabla \cdot \boldsymbol{\sigma} + \rho_b g = 0, \tag{13}$$

where $\boldsymbol{\sigma}$ is the total stress tensor, and ρ_b is the bulk density. The assumption of the infinitesimal transformation allows the strain tensor, $\boldsymbol{\varepsilon}$, to be symmetric gradient of the displacement vector, $\mathbf{u}$, as

$$\boldsymbol{\varepsilon} = \frac{1}{2}\left(\nabla^T \mathbf{u} + \nabla \mathbf{u}\right) = 0\,. \tag{14}$$

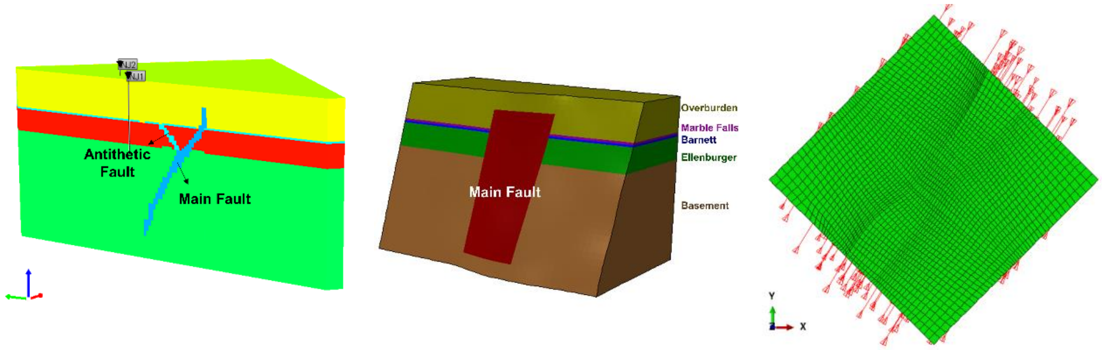

(a) (b) (c)

Figure 58. Flow and geomechanical simulation models: (a) CMG model, (b) ABAQUS model, (c) the maximum horizontal stress (intermediate principal stress) direction in the ABAQUS model

The geomechanical simulation model has 98,010 grid cells (104,848 nodes) which is coarser than the flow simulation model. The pressure distribution in the geomechanical model at each time step is updated from the calibrated flow simulation. The faults in the ABAQUS model are represented as discontinuous surfaces and the slip along the discontinuous surfaces is governed by the Coulomb failure criteria, assuming 0.7 of friction coefficient. The Young's modulus and Poisson's ratio for formations are summarized in Table 13. The initial effective stresses are 15.36MPa/km, 14.9MPa/km, and 3.55MPa/km for the vertical, maximum and minimum horizontal stresses with 32°NE (32° from y-axis to x-axis in Figure 58(c)). Figure 58(c) shows the maximum horizontal stress direction after the equilibrium step for the initialization. The transformed stress input with fixed displacement boundary provides correct horizontal stress direction. It is worth noting that though the fault geometry is based on the seismic survey, we allowed the fault slip to propagate beyond the original fault picks such that the slip is not constrained only in the original fault interpretation.

Table 13. Flow and geomechanical properties for simulation input

Formation	Permeability (md)	Porosity	Young's Modulus (GPa)	Poisson's ratio
Overburden	0.01	0.2	14.4	0.2
Marble Falls	0.01	0.2	60	0.2
Barnett	1e-5	0.06	40	0.23
Ellenburger	5-100	0.055	60	0.2
Basement	1e-4	0.05	43	0.27

Flow Model Calibration

For the CMG model calibration, the wells are constrained by fluid rate. For producers, the fluid rate combines water and gas production rates and for injectors, it is water injection rate. The gas volume is converted from the surface condition to the reservoir condition using tubing head pressure (THP), fluid properties and well configuration. The well responses to history-match include injectors' BHP, producers' gas production. Among 70 producers, THP for 28 wells were available, provided by the operator. Using a commercial software PROSPER, wellbore model was built and imported to the flow simulation model to include 28 THP well data in the history matching. Compared to the previous study, including multiphase flow and THP in the history matching is a new feature in the current study.

The model calibration was performed in CMOST, minimizing errors in injectors' BHP, the operators' THP, and the cumulative gas production for each producer. The global error to minimize is the weighted summation of each error in BHP, THP and cumulative gas production,

$$Error_{global} = w_{BHP} Error_{BHP} + w_{THP} Error_{THP} + w_{Cum.Gas} Error_{Cum.Gas} \tag{15}$$

where w is the weight for each objective function.

CMOST defines the history match error for a well i as

$$Q_i = \frac{\sqrt{\dfrac{\sum_{t=1}^{T(i)} \left(Y_{i,t}^{s} - Y_{i,t}^{m}\right)^2}{NT(i)}}}{scale_i} \tag{16}$$

where the subscript t indicates time, $NT(i)$ is the total number of measured data points, $Y_{i,t}^{s}$ is the simulation result, $Y_{i,t}^{m}$ is the measure results and $scale_i$ is the normalization scale to avoid the scale effect when different data types are integrated (Computer Modeling Group, 2018).

Before performing history matching, we conducted sensitivity analysis to identify heavy hitters, the influential parameters for this particular history matching problem. Table 14 lists the parameters and their ranges for the sensitivity analysis. The parameters are associated with flow properties of hydraulic fractures, the Barnett, the Ellenburger, the faults. The compressibility and permeability anisotropy are also included in the sensitivity analysis. The error in the sensitivity analysis was evaluated changing one parameter at-a-time such that we can see the impact of the parameter change on the misfit while other parameters are fixed. Figure 59 shows the sensitivity result in the tornado chart. It is identified that the fracture permeability and the permeability anisotropy are the most influential parameters. This implies the interaction between water disposal in the Ellenburger and hydrocarbon production in the Barnett has a great impact on the flow simulation results. After the sensitivity analysis, the parameters with strong influence on the error, from the fracture permeability to the formation compressibility, are kept and less influential parameters are discarded for the model calibration.

Table 14. Sensitivity analysis parameters

Category	History Matching Parameters	Low	Base	High
Hydraulic Fractures	Permeability (md)	0.01	0.2	1
Barnett	Water saturation	0.2	0.4	0.6
	Porosity	0.055	0.06	0.065
	Permeability (md)	1E-4	1E-5	1E-6
Ellenburger	Porosity	0.05	0.055	0.06
	Permeability (md)	5	30	100
Fault	Permeability (md)	1E-6	1E-5	1E-2
Formations	Permeability anisotropy (Kv/Kh)	0.01	0.1	0.2
	Compressibility (KPa^{-1})	1.5E-7	2.6E-7	4E-7

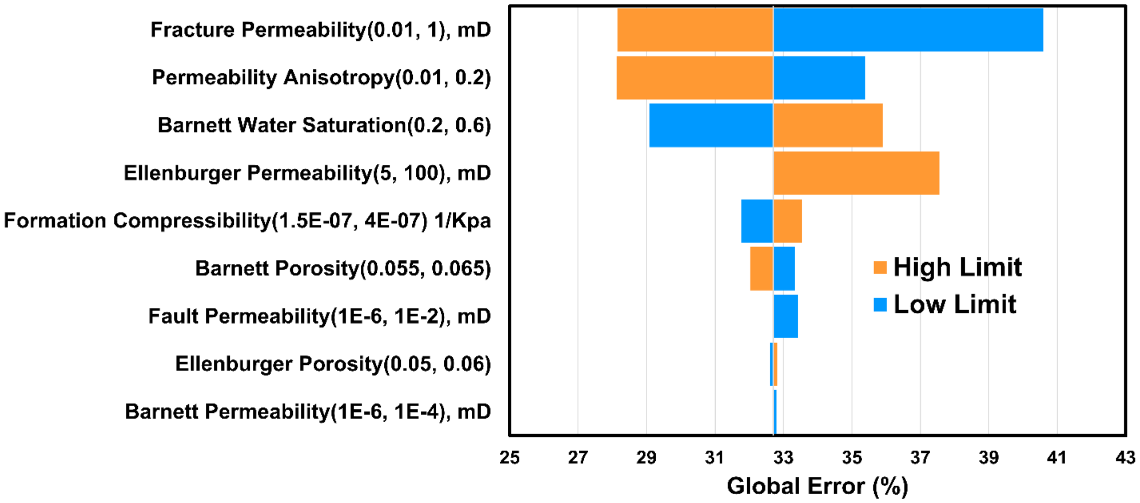

Figure 59. Tornado chart for sensitivity analysis results

In order to history-match the well responses, we simulated 1,000 cases using an evolutionary algorithm to minimize the misfit between the history data and the simulation results. Figure 60(a) shows that the evolutionary algorithm gradually reduces the global error as it runs more simulations. The models with less global misfits are selected as updated models to show the improvement from the base model, the initial model that we started from. The optimal case is the model with the least global misfit among 1,000 simulations. Several wells are sampled to check the history matching quality of the injectors' BHP (Figure 60(b)-(c)), producers' cumulative gas production (Figure 60(d)-(f)) and THP (Figure 60(g)-(i)). Figure 60(b)-(c) show that the optimal case closely reproduces the history BHP of both injectors. The updated models also follows the trend of the BHP history. Figure 60(d)-(f) shows good agreement in cumulative gas production between the history data and the updated models. Compared to the BHP and the gas production, THP shows relatively larger variation. However, the overall trends from the updated models are also in good agreement with the history data. Therefore, it is found that the satisfactory quality of history matching results were achieved.

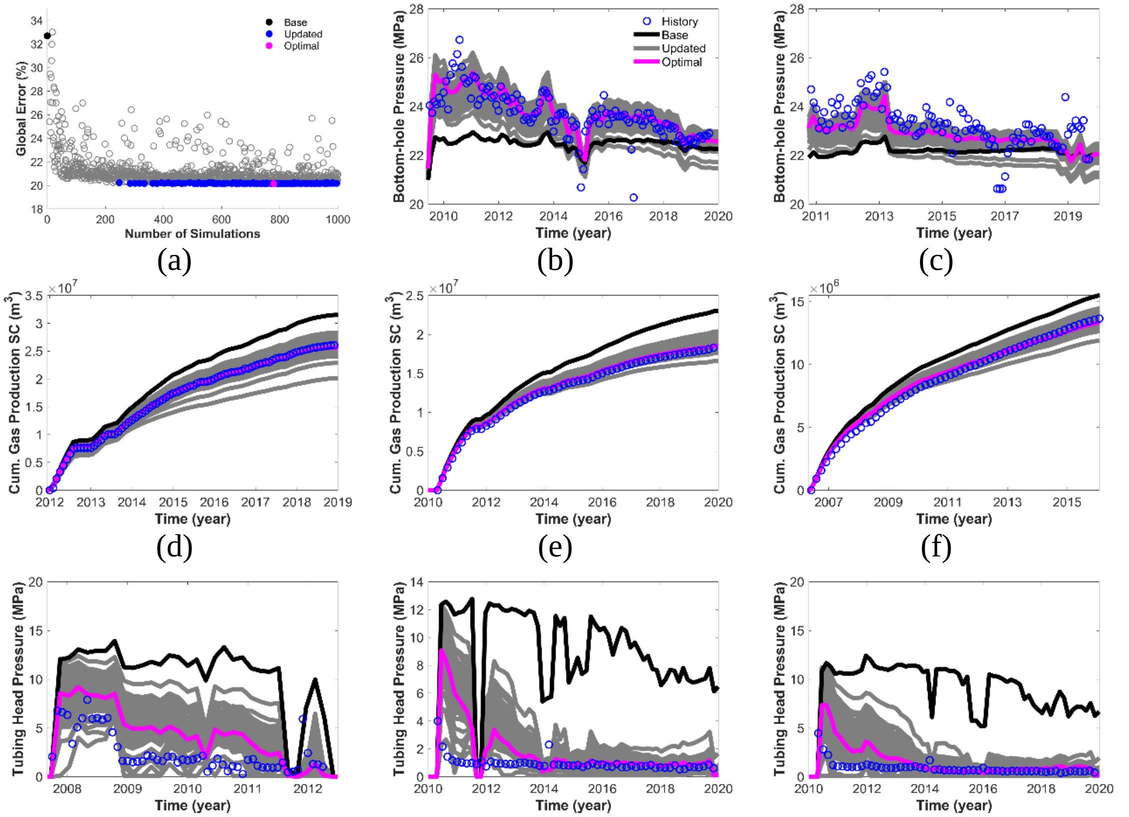

(a) (b) (c)

(d) (e) (f)

(g) (h) (i)

Figure 60. History matching results from sampled wells: (a) global misfit with number of simulations, bottom-hole pressure of (b) injector #1 (c) injector #2, gas cumulative production in surface condition of (d) producer #2, (e) producer #21, (f) producer #52, tubing head pressure of (g) producer #17 (h) producer #21 and (i) producer #44

The improvement also can be seen in history matching parameter distributions. Figure 61 shows history matching parameter ranges before and after the model calibration. Before the model calibration, the parameters were almost uniformly distributed and the distribution ranges have significantly reduced after the calibration. Especially, Ellenburger permeability, permeability anisotropy, Barnett water saturation, and fracture permeability show significant reduction in the distribution range. The calibrated low Barnett water saturation implies that in order to reproduce history gas production rate, the Barnett has to be highly gas-saturated.

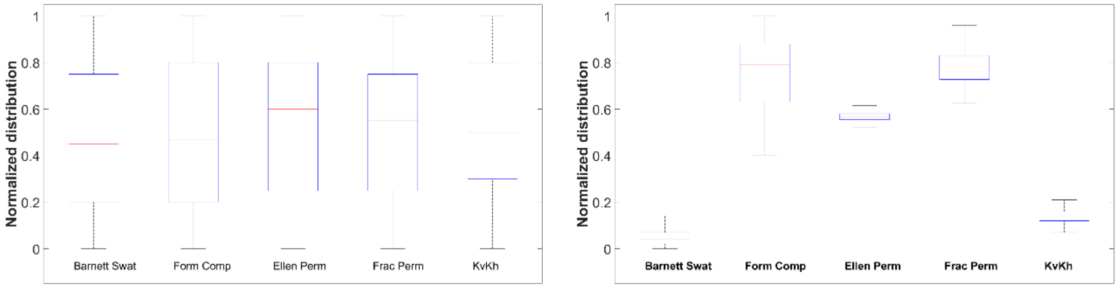

(a) (b)

Figure 61. History matching parameter distributions: (a) prior and (b) posterior

After the flow model calibration, we took the calibrated pressure distributions and updated the pressure in the geomechanical simulation model. The ABAQUS then computes stress change due to the pressure disturbance in response to the injection and the production and assesses subsequent fault slip and fault frictional energy.

Geomechanical Simulation Results

In the proposed workflow, the pressure change from the CMG model is reflected in the stress field change and fault slip in the ABAQUS model. Therefore, it is crucial to accurately update pressure from the CMG model to the ABAQUS model. However, the pressure value coordinates in the CMG model and the ABAQUS are not identical due to different mesh resolution and discretization scheme. Therefore, we utilized the inbuilt interpolation function, *griddata* in *Matlab*, to transfer pressure information from the CMG model to the ABAQUS model. The interpolation function estimates pressure value at ABAQUS nodes, given pressure values at CMG cell center and cell center coordinates in 3D space. Figure 62 shows pressure map comparison at different times between CMG and ABAQUS with the base case. Even though the small difference might come from different resolution and value coordinates between two simulation domains, pressure maps from CMG and ABAQUS show consistency.

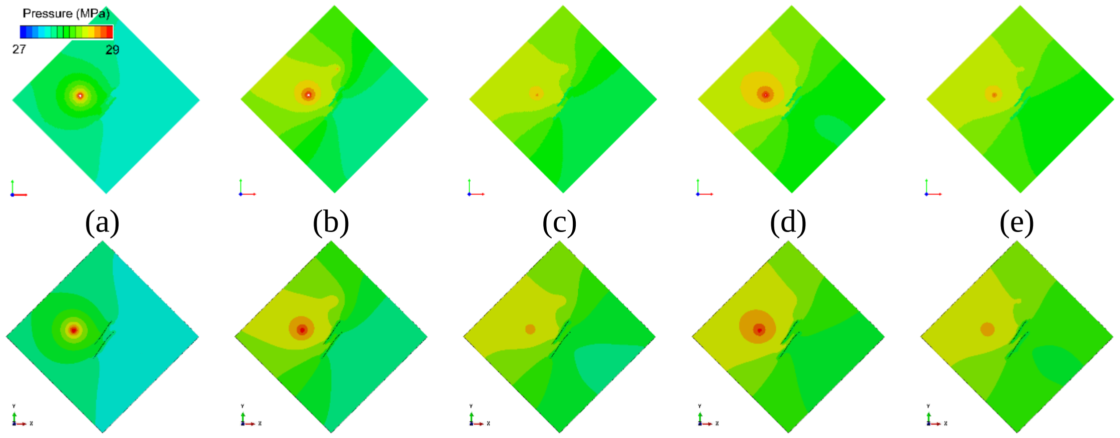

(a) (b) (c) (d) (e)

(f) (g) (h) (i) (j)

Figure 62. Pressure distribution comparison between the CMG (a)-(e) and the ABAQUS (f)-(i) at different times. Columns from left to right indicate 2010, 2013, 2015, 2018, and 2020, respectively

Figure 63 shows the ABAQUS simulation results after the calibrated pressure data has been updated. Figure 63(a) and Figure 63(b) show field-wise water injection and fluid production, respectively. The vertical lines in the figures indicate times at 2008, right before the water injection, 2009, right after the water injection, 2014, the time when earthquakes were observed, and 2018. Figure 63(c) shows the fault slip evolution from the first time step along the red line in Figure 63(e). Before the water injection, the slip mainly occurs in the reservoir and after the injection, the slip starts propagating down to the basement. In 2014, we observe a larger slip in the basement and the slip propagates further down, even -6km deep and the below, yet there is no significant difference after 2014. Figure 63(d) shows pressure change from the first time step along the red line in Figure 63(e). Owing to the hydrocarbon production, the Barnett experiences depletion at an early time while the Ellenburger shows slight pressure increase at a later time due to the water injection. Figure 63(e)-(h) show slip magnitude along the entire main fault at different times. An interesting observation is that we do not see any pressure change in the basement while we do see fault slip in the basement. This is consistent with previous study's conclusion that the poroelastic effect resulted from the unbalance loading across the faults appears to be the primary mechanism of the Azle earthquake in the deep crystalline basement (Chen et al., 2020b).

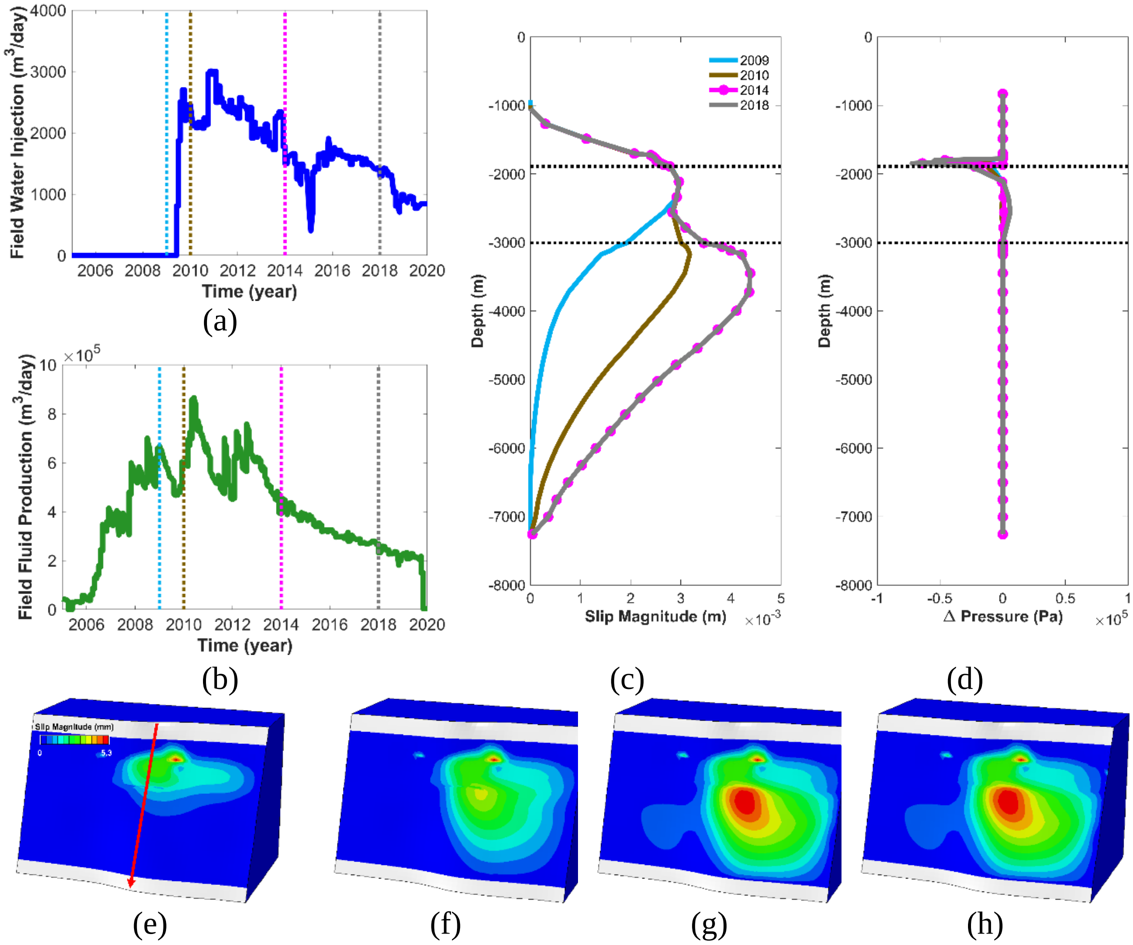

(a) (b) (c) (d) (e) (f) (g) (h)

Figure 63. Field-wise fluid injection/production and subsequent ABAQUS simulation results: (a) field water injection, (b) field fluid production, (c) fault slip evolution from the initial state, (d) pressure change from the initial state, (e) fault slip magnitude in 2009, (f) fault slip magnitude in 2010, (g) fault slip magnitude in 2014, and (h) fault slip magnitude in 2018

Given the slip magnitude, fault contact area and shear stresses on the fault surfaces, we can calculate the frictional energy generated from the fault slip as

$$\sum_{i=1}^{n} cshear_i \times cnarea_i \times cslip_i \, , \qquad (17)$$

where n is the number of node on the fault plane, $cshear$ is the shear stress on the fault surface, $cnarea$ is the contact area, and $cslip$ is the fault slip. Note that shear stress and slip are vector that we have two components on the fault surface, indicated by the subscript i. The calculated frictional energy is then compared with the energy converted from the observed earthquakes. We estimated the radiated energy from the moment magnitude of the observed earthquakes using

$$M_w = \frac{2}{3}\log E_s - 3.2\,, \tag{18}$$

where M_w is the moment magnitude and E_s is the radiated energy (Kanamori, 1977).

We compared the cumulative fault frictional energy and radiated energy from the observed earthquakes. Note that the energy profiles in Figure 64(a) are in different scale. The radiated energy from the earthquakes is about only 1% of the cumulative frictional energy. However, in regards to the energy profile shape, the cumulative energy already flattens out around 2014 when the sharp surge in the radiated energy was observed. We then broke down the energy into formations and looked at the incremental frictional energy. Figure 64(b) shows the incremental fault frictional energy at different formation and histogram of the earthquakes with magnitude larger than 1.5. The incremental energy profiles from the basement and the Ellenburger show distinctive features in the magnitude and the timing. About 90% of the entire fault frictional energy is attributed to the basement which is consistent with the observation that larger earthquakes occurred in the basement. We can see that there is the time gap between the Ellenburger and the basement in terms of the peak incremental energy and the basement shows more slip at the later time, especially around 2014 when the earthquakes were reported, compared to the Ellenburger. However, this is still very little energy from the basement to correlate with observed earthquake frequency. Hence, we investigated the sensitivity of the incremental energy profile so that the incremental energy can be better correlated with the observed earthquake events.

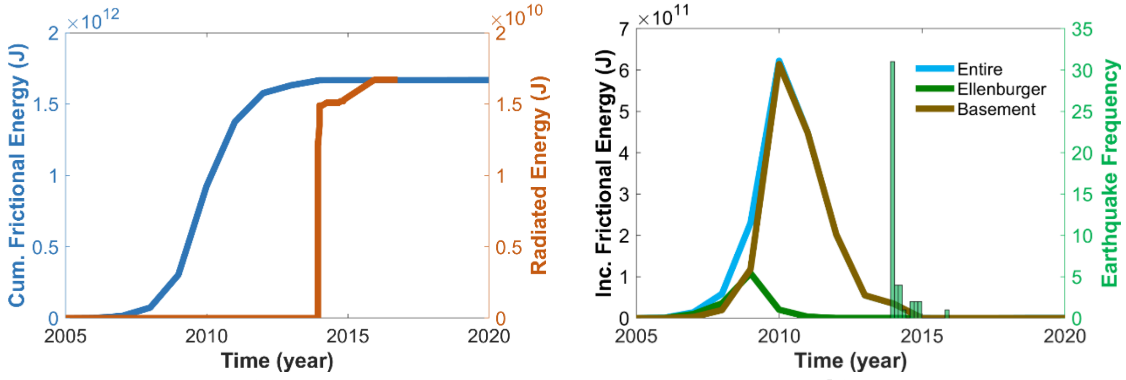

(a) (b)

Figure 64. Energy profiles from the ABAQUS model and earthquakes: (a) comparison between cumulative fault frictional energy from the ABAQUS model and radiated energy from earthquakes, (b) incremental fault frictional energy in formations and earthquake frequency with magnitude larger than 1.5

Sensitivity Study of Energy Profile

Stress Gradient and Direction in Geomechanical Simulation Model

Based on the parameter uncertainties in Table 12, we generated four simulation cases with different parameter combinations as summarized in Table 15. Compared to the base case, Case 1 is assigned with larger maximum horizontal stress, Case 2 is assigned with smaller maximum horizontal stress and Case 3 is assigned with larger minimum horizontal stress. For Case 4, the maximum horizontal stress direction is changed from 32° to 48° NE**.**

Table 15. Simulation cases for geomechanical parameter sensitivity

Simulation Case	Sv (MPa/km)	Shmax (MPa/km)	Shmin (MPa/km)	A_ϕ	Shmax azimuth (°)
Base Case	26.01	25.6	14.2	0.96	32
Case 1	26.01	28.5	14.2	1.2	32
Case 2	26.01	23.5	14.2	0.78	32
Case 3	26.01	25.6	16.0	0.96	32
Case 4	26.01	25.6	14.2	0.96	48

Figure 65 shows the results of geomechanical parameter sensitivity with the magenta vertical line indicating 2014 when the majority of earthquake occurred. Case 2 (smaller maximum horizontal stress) and Case 4 (maximum horizontal stress direction of 48° NE) show larger cumulative fault frictional energy compared to the base case while Case 1 (larger maximum horizontal stress) and Case 3 (larger minimum horizontal stress) show less frictional energy (Figure 65(a)). Figure 65(b) shows the incremental frictional energy from the geomechanical parameter sensitivity. The different geomechanical parameters have an impact on the magnitude of the frictional energy and yet the parameters did not change the general trend of the energy, especially for the peak incremental energy timing. Therefore, we investigated the sensitivity of flow simulation setting on the energy profile to examine its impact on the peak energy timing.

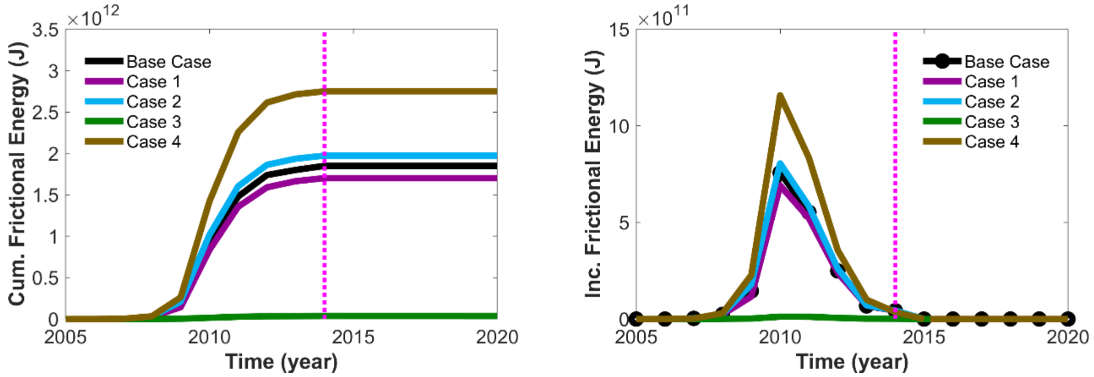

(a) (b)

Figure 65. Frictional energy in basement comparison between different geomechanical parameters: (a) cumulative fault frictional energy (b) incremental fault frictional energy

Extended Fault Geometry in Flow Simulation Model

After we found that stress magnitude and direction do not change the peak incremental energy timing, we revisited the flow simulation model. Figure 66 shows the calibrated pressure maps at the Ellenburger bottom at different times. The two injectors are in the northwest side of the model and 70 producers are distributed over the simulation domain and yet most of them are concentrated in southeast side of the model. We found that the southeast part, where production is dominant, is also pressurized around 2012 (Figure 66(d)). This implies that pressure increase from the injectors propagates to the other side of the fault in 2012. Knowing that the driving mechanism for the earthquakes in the basement is pressure imbalance across the faults from the previous study (Chen et al., 2020b), we extended the faults in the CMG model, expecting that larger faults with low permeability act like flow barriers that the pressure communication across the faults would be delayed.

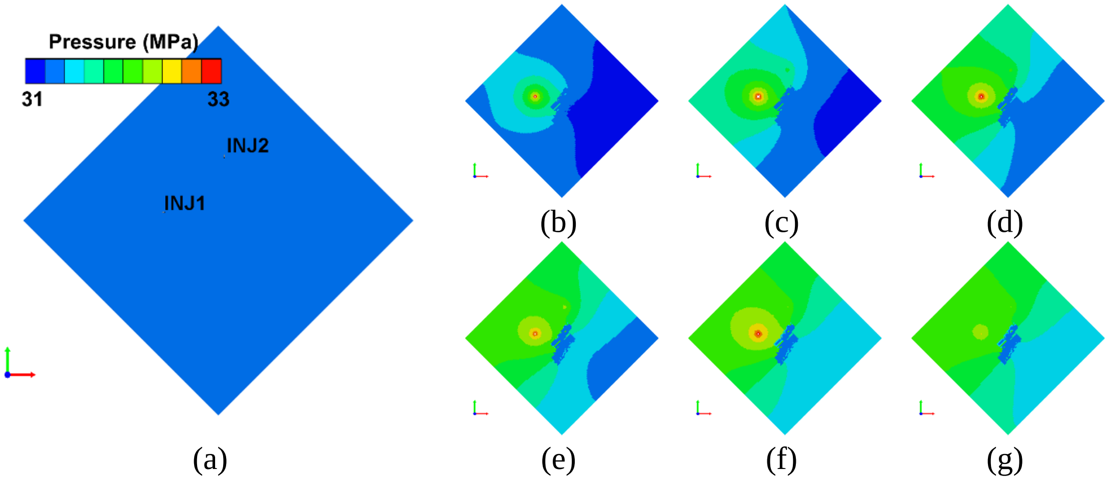

Figure 66. Pressure maps at different times: from (a) 2009 to (g) 2015

Figure 67 shows the original and extended fault geometry in the CMG model and corresponding pressure maps at different times. The blue parts in Figure 67(a)-(b) are faults cells in the CMG model. With the updated fault configuration, we history matched the CMG model again. Even though the extended fault does not completely separate two sides of the faults, the CMG model with the extended faults magnifies the pressure difference across the faults (Figure 67(g)-(j)) compared to the original CMG model (Figure 67(c)-(f)).

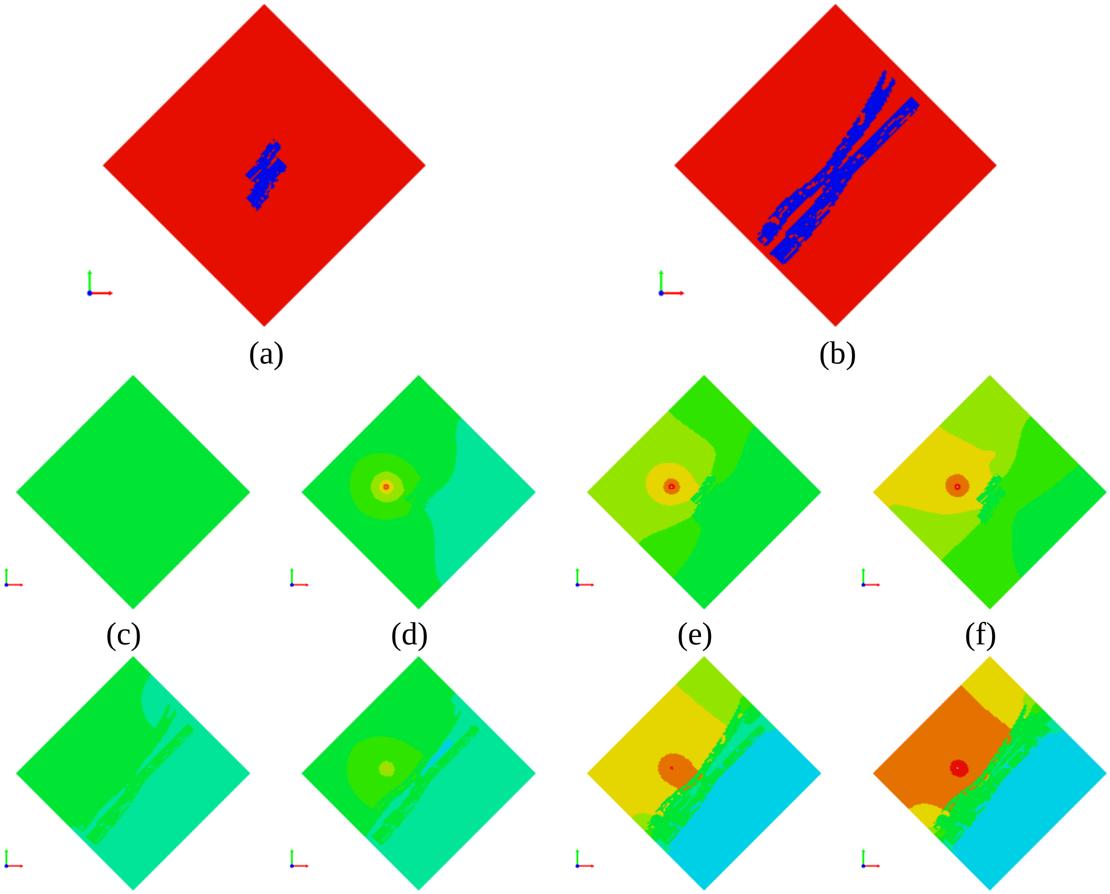
(a) (b)
(c) (d) (e) (f)
(g) (h) (i) (j)

Figure 67. Faults configuration in the CMG model and pressure maps from 2009-2014: (a)the original faults, (b)the extended faults, (c)-(f) pressure maps with the original faults and (g)-(j) pressure maps with the extended faults in the CMG model

Such difference in pressure distribution has an impact on the fault slip. Figure 68 shows the fault slip incremental at different times from 2009 to 2014. After the water injection, the slip starts propagating to the basement (Figure 68 (b)) and the slip incremental keeps increasing until 2012. Compared to the previous cases, Figure 68 shows a larger slip even after 2012. Another observation is that the peak slip incremental is now 2012 as opposed to 2010 in the previous cases.

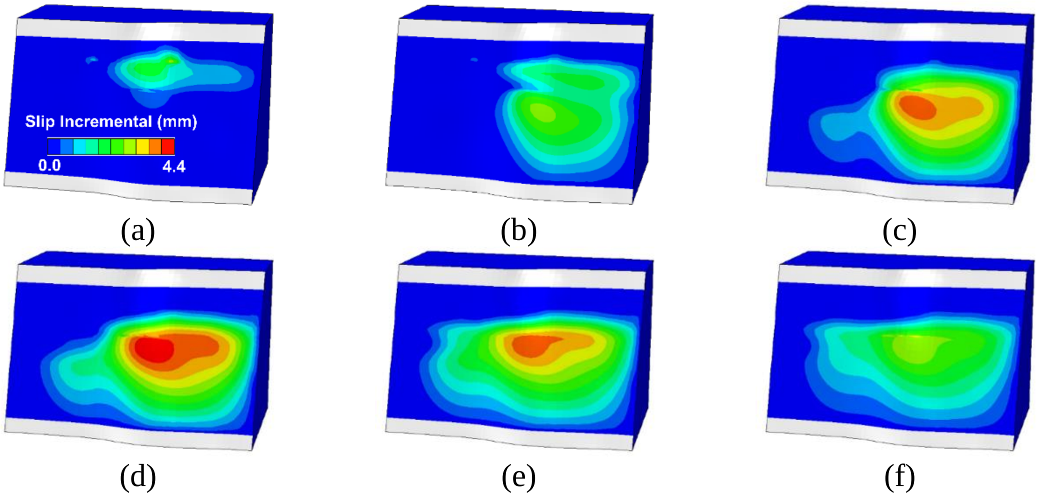

(a) (b) (c)

(d) (e) (f)

Figure 68. Fault slip incremental of the large fault case at different times: (a) 2009, (b) 2010, (c) 2011, (d) 2012, (e) 2013, and (f) 2014

Given the fault slips with the extended faults in the CMG model, we calculated the fault frictional energy and compared with the small fault case, which is the original case. The different trend in the energy file is now seen. Figure 69(a) shows the cumulative frictional energy profiles. With the extended faults, the cumulative frictional energy keeps increasing even after 2014. When we look at the incremental frictional energy (Figure 69 (b)), the peak incremental energy is around 2012 as opposed to 2010 in the original case. The onset of the fault slip in both cases is around 2009-2010, related to the water injection, and yet the extended fault case produces the peak fault slip in 2012 and large slip even after 2014. This rationalizes employing the energy profile from the extended fault case to better correlate with the observed earthquake events compared to the original case.

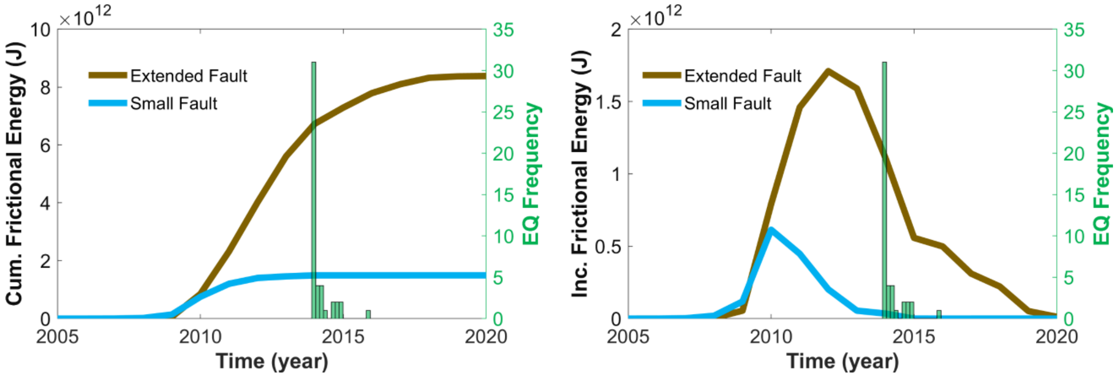

(a) (b)

Figure 69. Frictional energy in basement comparison between the extended fault case and the original fault case: (a) cumulative fault frictional energy (b) incremental fault frictional energy

Boundary Effect in Flow Simulation Model

Lastly, we investigated the sensitivity of the boundary effect in the flow model. The previously presented flow models have closed boundary, no flux from and to the model outer boundary. The flow model size was designed to be comparably large enough (12km ×12km in i and j direction) to previous the Azle area studies (Chen et al., 2020b; Hornbach et al., 2015). However, the flow models, especially with the large fault geometry, show that the pressure disturbance from the wells can reach the model boundary with large pressure difference. In reality, the disturbance might not be limited to the flow model boundary. Hence, we investigated the impact of the flow model boundary, which eventually affects the overall pressure distribution in the model. Instead of building new flow model with larger size, we imposed a constant pressure at the outer boundary. In order to impose constant pressure at the model boundary, we assigned high pore-volume multiplier (×10,000) to the boundary cells. The high pore-volume cells in the boundary make the reservoir under infinite pressure support from the boundary. For example, if the reservoir is pressurized, the boundary cells absorb outflow from the reservoir and if the reservoir is depleted, there is influx from the boundary to the reservoir. With high pore-volume cells incorporated in the CMG model, we history matched the model again and compared the resulting pressure maps. Figure 70(a) shows pressure map with high pore-volume cells at the boundary. Figure 70(b)-(c) show the pressure maps in 2011 from closed boundary and open boundary, respectively. Compared to the closed boundary, the pressure disturbance in the open boundary case is mainly observed at the center of the model, not the vicinity of the boundary. Note that both cases have the large fault configuration in the simulation models.

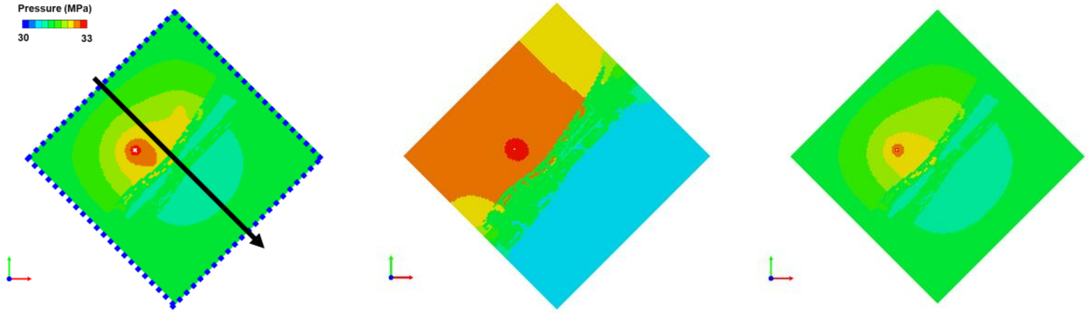

(a) (b) (c)

Figure 70. Imposing constant pressure boundary in the flow model and pressure map comparison: (a) High pore-volume cells in the boundary highlighted by blue dashed line, (b) pressure map with closed boundary model in 2011, and (c) pressure map with open boundary model in 2011

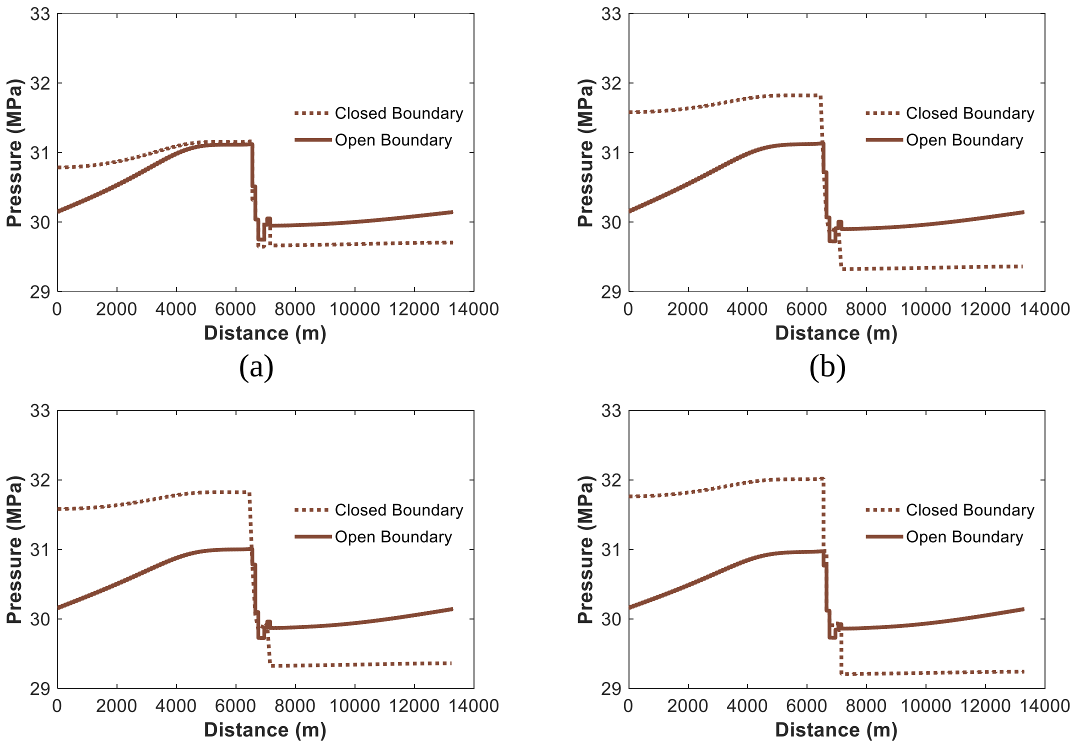

(a) (b)

(c) (d)

Figure 71. Pressure profile along the black arrow in Figure 70 at different times: (a) 2011, (b) 2012, (c) 2013, and (d) 2014

To compare the pressure difference in detail, we took the pressure profile along the black arrow in Figure 70(a) and visualized at different times. Figure 71 shows the pressure profile and confirms that pressure disturbance is maximum at the center, near the fault, and diminishes, approaching the boundary in open boundary case. Also, the pressure difference across the fault amplifies with time in the closed boundary case while the pressure difference does not significantly change in the open boundary case.

The less pressure difference across the faults is reflected in the fault slip in the ABAQUS model. Figure 72 shows the fault slip incremental with the pressure updated from the open boundary case. Compared to Figure 68, the open boundary case shows smaller fault slip incremental in general. Also, the most slip occurs in 2010-2011 and after that the slip incremental decreases whereas with the closed boundary case, the peak slip incremental is around 2012.

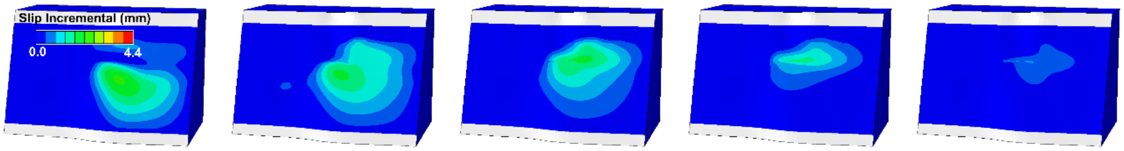

(a) (b) (c) (d) (e)

Figure 72. Fault slip incremental of the open boundary case at different times: (a) 2010, (b) 2011, (c) 2012, (d) 2013, and (e) 2014

Figure 73 shows the comparison in the energy profile of different flow boundary conditions. The incremental energy profile in the open boundary case shows a similar trend with that in the small fault case: peak in 2010 and small energy around 2014. Therefore, we selected the energy profile in the closed boundary with the extended fault configuration model to build a correlation with the observed earthquakes.

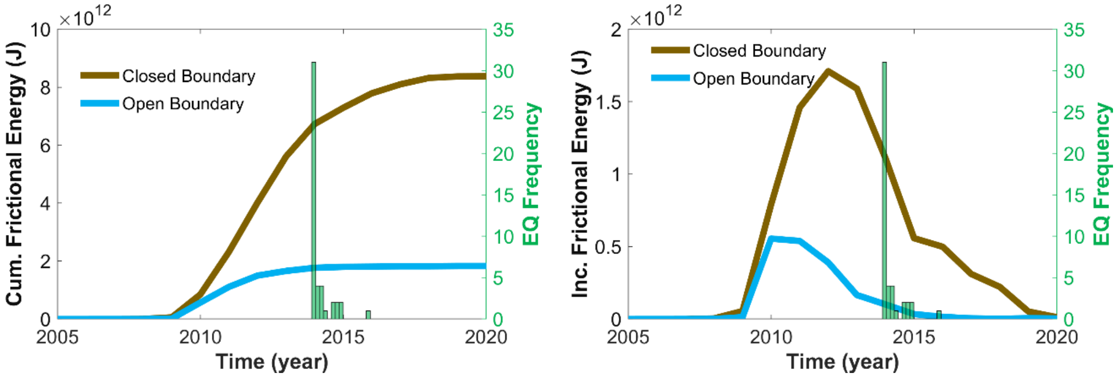

(a) (b)

Figure 73. Frictional energy in basement comparison between the open boundary case and closed boundary case: (a) cumulative fault frictional energy (b) incremental fault frictional energy

Site-specific Empirical Seismological Model

The objective of building a seismological model is to have predictive capability of induced earthquakes, given operational conditions. Lele et al. (2015); Lele et al. (2016) built an empirical seismological model to forecast production-induced seismicity in Groningen gas field, Netherland. They correlated the frictional energy from the geomechanical simulation model and the observed earthquakes to predict the number of earthquakes. Similarly, we built the Azle-specific seismological model based on observed earthquakes near the Azle area and the fault frictional energy from the ABAQUS model to assess potential fluid-induced seismic events

We correlated the incremental fault frictional energy from the closed-boundary flow simulation model and the observed earthquake frequency with the magnitude larger than 1.5. Given the same time, we put the incremental frictional energy in x-axis and the observed earthquake events in y-axis. Then, regression models were built using polynomials and exponential function (Figure 74). Table 16 summarizes their equations for parametric regression forms. It appears that 3rd order polynomial and exponential function are relatively good fit for this particular case. However, as shown in Figure 74, the correlation highly depends on the parametric regression forms. Moreover, the best fit should be case-dependent. In other words, we need to try multiple regression forms to find the best fit in different cases which is not robust and easy to be generalized.

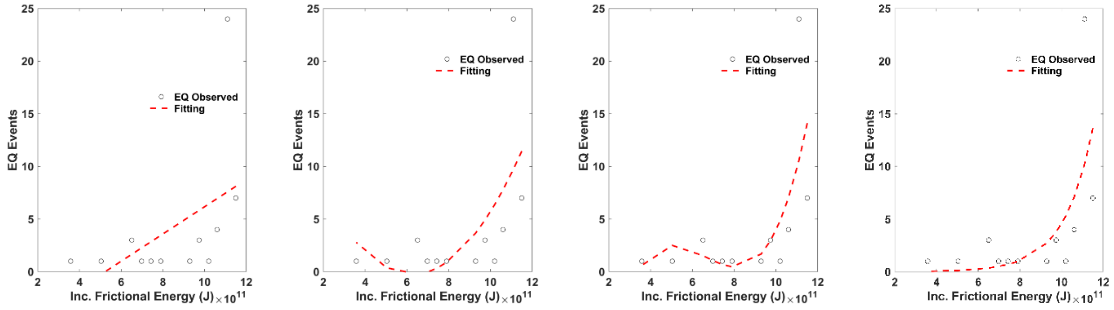

(a) (b) (c) (d)

Figure 74. Correlation between frictional dissipation energy from the ABAQUS model and observed earthquake events: (a) linear form, (b) second-order polynomial, (c) third-order polynomial, and (d) exponential forms

Table 16. Equations for polynomials and exponential regression between the incremental energy and earthquake events

Regression type	Equations
Linear	$y = 1.294 \times 10^{-11} x - 6.765$
Second-order polynomial	$y = 4.257 \times 10^{-23} x^2 - 5.326 \times 10^{-11} x + 1.639 \times 10^1$
Second-order polynomial	$y = 1.467 \times 10^{-34} x^3 - 2.889 \times 10^{-22} x^2 + 1.794 \times 10^{-10} x - 3.336 \times 10^1$
Exponential	$y = 3.058 \times 10^{-3} \exp\left(7.306 \times 10^{-12} x\right)$

Another issue is that there is a possibility of the predicted earthquakes from regression forms showing unphysical behavior. For example, Figure 75 shows the predicted earthquakes using polynomials and exponential function. The predicted earthquakes using 2nd order polynomial shows an increase in the earthquake events after 2015. This is because the correlation using 2nd order polynomial shows a concave-up trend in Figure 74(b), giving higher earthquake frequency with the incremental energy less than 6×10^{11}. This is unphysical in the sense that it is unrealistic to expect frequent earthquakes while the energy profile from the ABAQUS models shows monotonic decrease after 2015.

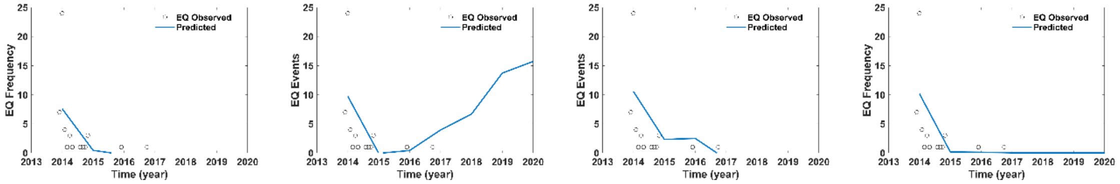

(a) (b) (c) (d)

Figure 75. Predicted earthquake frequency using the correlations: (a) linear, (b) second-order polynomial, (c) third-order polynomial, and (d) exponential forms

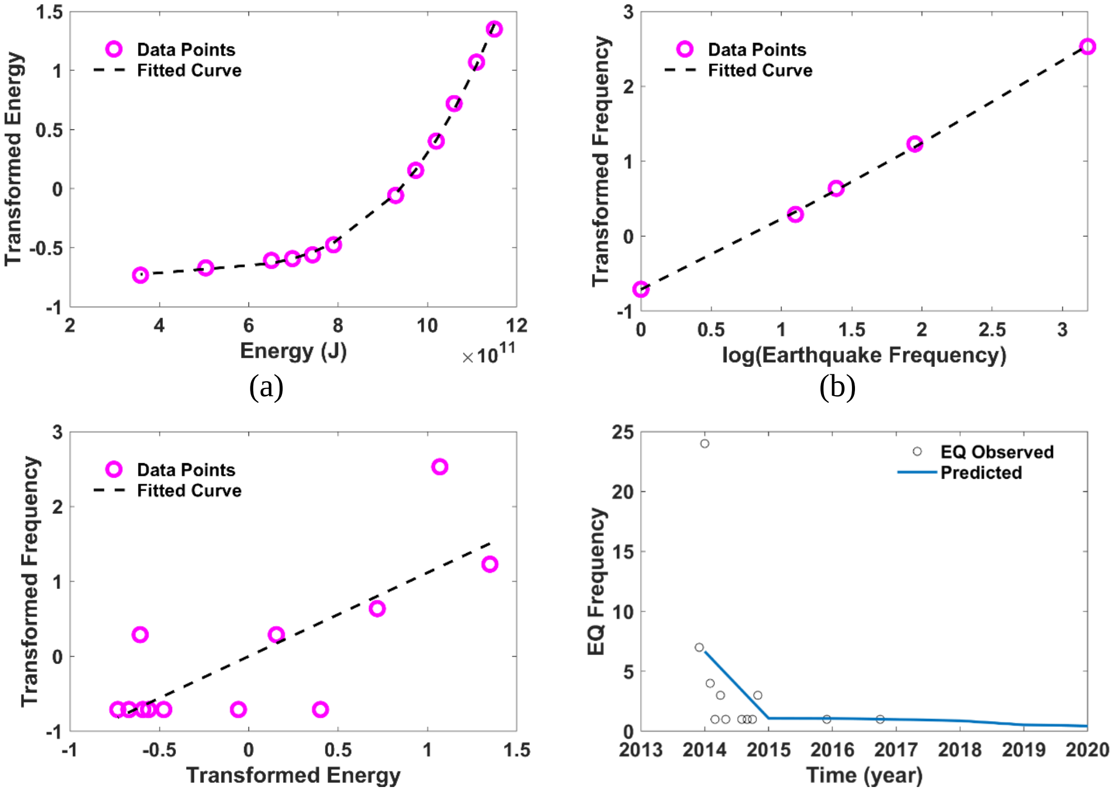

(a) (b) (c) (d)

Figure 76. Application of ACE algorithm to the frictional energy from ABAQUS model and the earthquake events: (a) transformation of the incremental frictional energy, (b) transformation of the earthquake frequency, (c) the maximum correlation between the transformed energy and the earthquake frequency, (d) predicted earthquake frequency using the correlation

Therefore, we tried non-parametric regression using Alternating Conditional Expectation (ACE) algorithm (Breiman and Friedman, 1985; Mishra and Datta-Gupta, 2017). The ACE algorithm automatically finds the optimum transformation of variables such that the correlation between transformed variables is maximized (See (Xue et al., 1997) for the detailed implementation). Using the algorithm, we found the optimum transformation of the incremental energy (Figure 76(a)) and earthquake frequency (Figure 76(b)) and we obtained the maximum correlation between two transformed variables (Figure 76(c)). The equation forms for the optimum transformation and the correlation is summarized in Table 17 and R^2 in Figure 76(a)-(c) are 0.99, 0.99, and 0.61, respectively. Figure 76(d) shows the predicted earthquake frequency with the correlation. The non-parametric regression predicts a monotonic decrease in the earthquake frequency, which is consistent with the incremental energy profile from the ABAQUS model. The advantage of the non-parametric regression is that we can use it generally regardless of the data type and format. Also, we do not need to assume any functional forms for the regression thus, there is no need for trying multiple functional forms to find the best fit between data sets.

Table 17. Optimum transformation and the correlation equations

Transformation / Correlation	Equation Forms
Energy Transformed	$E_{tr} = 7.15\times10^{-36} E_{og}^{3} - 1.07\times10^{-23} E_{og}^{2} + 5.52\times10^{-12} E_{og} - 1.66$
Frequency Transformed	$f_{tr} = 3.92\times10^{-2} \ln\left(f_{og}\right)^{2} - 8.99\times10^{-1} \ln\left(f_{og}\right) - 0.7123$
Maximum Correlation	$y = 1.467\times10^{-34} x^{3} - 2.889\times10^{-22} x^{2} + 1.794\times10^{-10} x - 3.336\times10^{1}$

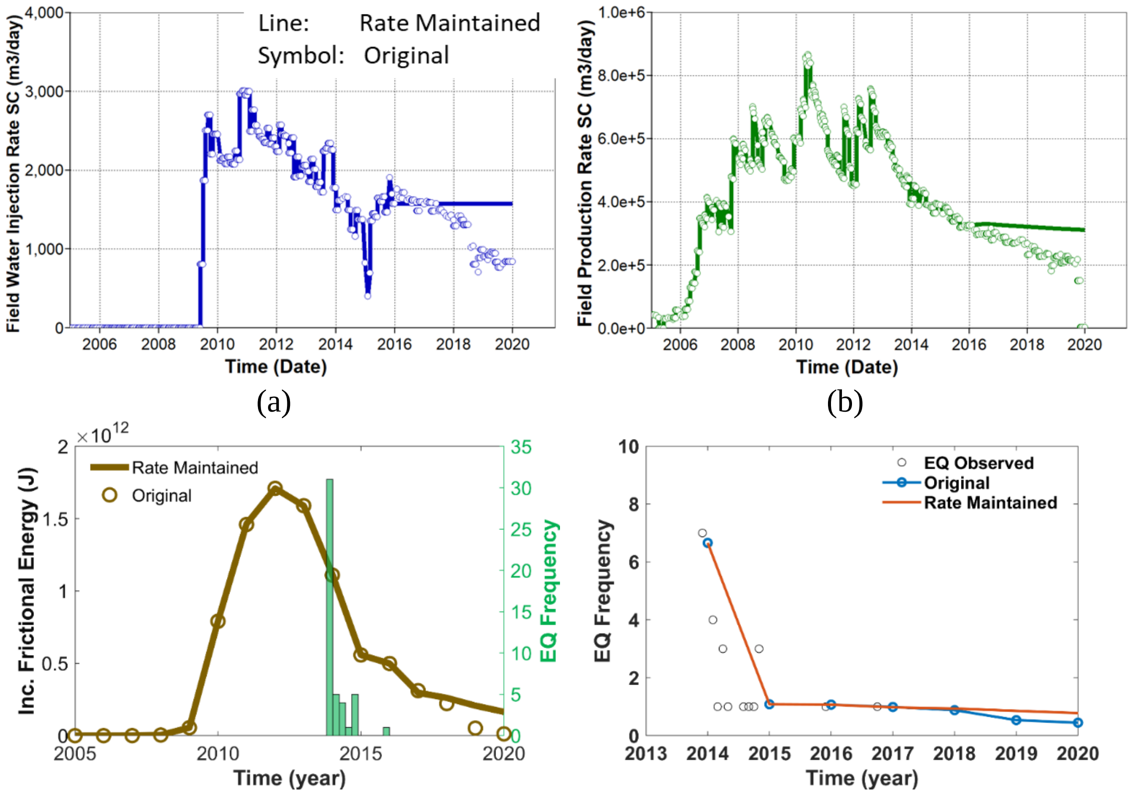

(a) (b)

(c) (d)

Figure 77. Rate-maintained operating condition and results comparison with the original operation: (a) field-wise water injection, (b) field-wise fluid (water+gas) production, (c) incremental frictional energy profile comparison, and (d) predicted earthquake frequency comparison

Lastly, we investigated what-if scenario to demonstrate how the empirical seismological model can be applied to different operation conditions to assess potential seismicity. Taking suggestions of the operator, we maintained production and injection rates after 2016 and see how this operational change makes a difference in the predicted earthquake frequency. Figure 77(a) and Figure 77(b) show field-wide water injection and fluid production, respectively. The field-wide production slightly decreases after 2016 because the reservoir loses its energy with time and cannot support the same level of production. We simulated the history matched CMG model with the maintained rates after

2016 and the pressure was then updated to the ABAQUS model to assess the incremental fault frictional energy. With the maintained rates, the incremental frictional energy slightly increased around 2018-2020 (Figure 77(c)). Such increase in the energy has an impact on the predicted earthquake frequency. However, though the maintained rates case showed higher earthquake frequency predicted (Figure 77(d)), the impact was relatively small. With this exercise, it appears that frequent earthquakes are unexpected with current operation condition. This is mainly because first, the production will keep decreasing as the reservoir gets depleted. Second, the operator might not increase the injection level as high as 2010-2012 level ever again.

Discussion

Many studies find the reason of fluid-induced seismicity, graphically analyzing shear failure and slip of rock volume or specific weak planes with Mohr circles and Coulomb failure line. However, does the shear failure or slip always accompany with seismicity? A field test in south France showed that it is not always the case. Guglielmi et al. (2015) injected fluid underground near faults in south France and measured resulting fault slip and seismicity. The fault slip in their experiment was in response to increasing fluid pressure along the fault plane and they found that most of the fault slip was aseismic slip, the fault slip that does not produce associated seismicity. Similar observation is made in this study. For example, Figure 64(a) shows the cumulative fault frictional energy is about 100 times larger than the radiated energy which is converted from observed earthquake magnitude, indicating that only very small portion of the slip is possibly released in the Azle area in terms of induced seismicity. However, this ratio cannot be easily generalized. Hence, we built an empirical seismological model using the observed earthquakes and the energy from the ABAQUS model for the Azle area specifically.

We could have utilized the cumulative, not incremental, frictional energy from the ABAQUS model and the radiated energy from the earthquakes to find the correlation. For example, based on Figure 64(a), we might expect only 1% of the cumulative energy from the ABAQUS model to be released as earthquakes. However, this approach cannot tell whether the radiated energy is going to be one large earthquake event or smaller multiple events. Since our interest was in assessing the number of relatively large earthquake events (the magnitude larger than 1.5 in this study), which possibly can be felt and damage properties on surface, we took the incremental fault frictional energy and the observed earthquake events to predict the frequency of large earthquakes.

The incremental energy profiles of all the presented cases in this study show a time gap between the peak earthquake events and the peak energy profile. We do not know at this moment that the incremental energy peak should or may not be aligned with the peak of the observed earthquake frequency. However, the consistent observation in all the cases is that the peak of the energy profile is before 2014, when the peak earthquake events is, and the energy monotonically decreases after 2014. This results in the prediction of infrequent earthquake events regardless of the disagreement of the peak timing. For example, Figure 78 shows the incremental energy profiles from the open boundary case with the time shift of 1-4 years and the histogram of earthquake frequency is fixed.

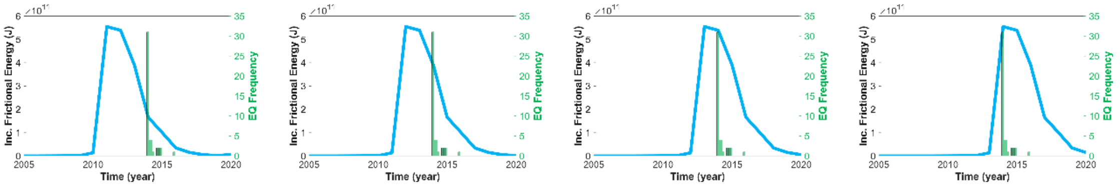

(a) (b) (c) (d)

Figure 78. Incremental energy profile from the open boundary case with time shift and histogram of earthquake frequency: (a) 1-year, (b) 2-year, (c) 3-year, and (d) 4-year time shift

With the shifted profiles, we applied the ACE algorithm and quantified the correlations. Figure 79(a) shows the R^2 of each correlation and 3-year time shift scores the highest R^2. We compared the prediction of earthquake frequency with the original model, no time shift case, and 3-year time shift model, the correlation with the highest R^2. Only a small difference was observed in the comparison after 2017 and it is hard to tell the difference is meaningful (Figure 79(b)). The implication of this exercise is we can expect that as long as the energy profiles show similar trends, where the peak is before 2014 followed by monotonic decrease, the predicted earthquakes would be only few and we observe such trends from all the ABAQUS simulation cases presented in this study.

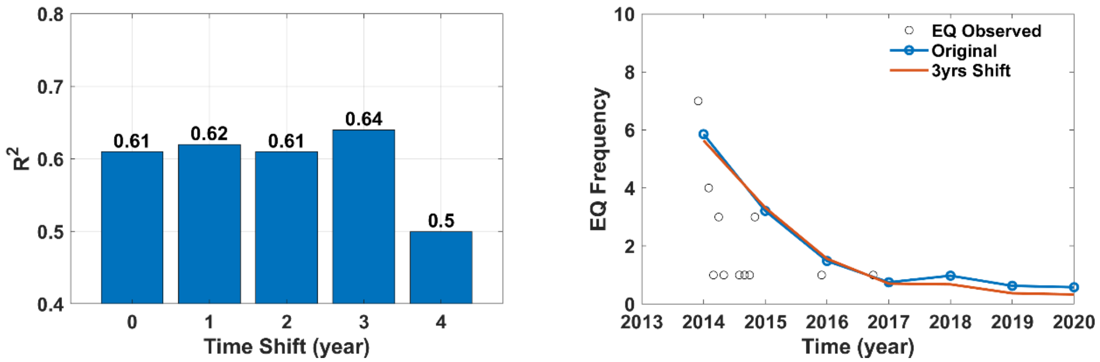

(a) (b)

Figure 79. The correlation results with the time shift: (a) R^2 with time shift of 0-4 years and (b) prediction results with 3-year time-shifted correlation

One of the potential improvements of the current work is to utilize dynamic friction coefficient. The static friction coefficient of 0.7 is assumed for the entire fault surfaces throughout this study based on (Hennings et al., 2019). However, as Scholz (1998) well summarized, it is understood that the friction coefficient could be dynamic and is rate- and state- dependent (Dieterich, 1979; Ruina, 1983) along with the loading time (Dieterich, 1978) and temperature (Stesky et al., 1974). Such slip-weakening or -hardening friction coefficients described by the empirical and heuristic model are not included in this study. Though current rate- and state- constitutive laws for rock friction is in a favor of aseismic slip (Bao and Eaton, 2016), incorporating the dynamic friction coefficient as well as heterogeneous slip (Ye and Ghassemi, 2020) with complex failure modes (Ferrill et al., 2017; Ferrill et al., 2020) would be helpful to provide more insights to understand and assess the fluid-induced earthquakes like Azle earthquakes.

Conclusion

Fluid injection and/or withdrawal to/from the subsurface inevitably results in the alteration of stress state in the reservoir. Possibly, such change in the stress condition unintentionally leads to reactivation of the existing faults, even away from the reservoir, followed by large earthquakes which are potentially felt in the surface and damage properties. Therefore, rigorous analysis is required to manage and assess risks associated with fluid injection and extraction activities near faults.

We revisited the earthquakes near the Azle area, where hydrocarbon production and produced water disposal occur simultaneously, with detailed fault modeling. While the previous Azle earthquakes studies investigated causal factors and the mechanisms of the earthquakes, the objective of the presented study is to quantitatively assess potential induced seismicity using fluid flow and geomechanical coupling simulations. The detailed fault modeling was realized by representing the faults as discontinuous surfaces in the geomechanical simulation model and incorporating seismic interpretation of the faults by the operator. We first calibrated the flow simulation model using injectors' BHP, producers' THP and gas production. An evolutionary algorithm gradually decreased the history matching misfits and generated a satisfactory quality of history-matched results. The calibrated pressure was then updated to the geomechanical simulation model to evaluate mechanistic behavior of the faults after the initial shear failure, including the fault slip and the fault frictional energy. Since the fault slip is a sufficient condition for induced earthquakes (i.e., not all fault slips are co-seismic), we compared the fault frictional energy from the geomechanical simulation model with the released energy from the observed earthquakes to build an empirical seismological model for the Azle area. The non-parametric ACE algorithm maximized the correlation between the fault frictional energy and the observed earthquake frequency. It was found that frequent earthquakes with the magnitude larger than 1.5 are unexpected with the current operational condition mainly because the production will keep decreasing as the reservoir gets depleted and the disposal level will be managed to be low.

The present workflow which integrates a large volume of field data provides systematic and robust analysis of fluid-induced earthquake prediction, which is essential to assess and manage potential seismicity risk associated with the fluid production/injection activity.

CHAPTER V

CONCLUSIONS AND RECOMMENDATIONS

Summary and Conclusion

In this dissertation, we utilized coupled fluid flow and geomechanical modeling to optimize unconventional field development and to quantitatively assess fluid-induced seismicity. In order to capture complex dynamics in unconventional reservoirs, physics-based reservoir simulations are necessary. However, the number of newly drilled and completed wells far outpaces the number of wells that can be analyzed with reservoir simulations which require extensive resources and manpower. To bridge the gap, we introduce proxy or surrogate models for full-physics reservoir simulations for fast and scaleable applications with underlying physics to find the optimum unconventional field development. Oil and gas activities alter stress and pressure field in subsurface due to hydrocarbon production and produced water disposal. The disturbance can possibly lead to the reactivation of existing faults causing unintended earthquakes which can damage properties in surface. It is important to have the capability to rigorously assess and manage risks associated with fluid-induced seismicity with detailed geological features and robust numerical simulations.

In Chapter II, we have proposed an empirical model for fracture compaction/dilation and the model was verified using ABAQUS, a fully coupled fluid flow and geomechanical simulator. The model relies on physical parameters to represent fracture permeability and porosity modification as function of pressure. In the simulation workflow, the fracture geometry and property are inferred from the injection phase modeling using finite difference simulation and it seamlessly transitions to FMM-based simulation for the following production phase modeling. We successfully applied the proposed method to a field case for rapid history matching and completion design sensitivity.

In Chapter III, we have developed a hybrid model for unconventional field development, combining physics-based reservoir simulations and data-driven machine learning algorithms. The reservoir simulations consist of injection and production phases so that we can capture the impact of completion designs, child well spacing and timing on the well performance. We tried to find the optimum structure of neural network model and achieved high accuracy ($R^2 = 0.94$) with orders of magnitude faster computation compared to the reservoir simulation. By incorporating history matching algorithm, the hybrid model applications smoothly scale from the well level to the field level for the optimum field development strategy, capturing well interaction including parent and child wells.

In Chapter IV, we incorporated horizons and faults provided by the operator into flow (CMG) and geomechanical (ABAQUS) simulation models for detailed fault modeling. We first calibrated the CMG model using injector's BHP, producers' THP and gas production. The calibrated pressure is updated to the ABAQUS model to assess fault slip and we compare the fault frictional energy with observed earthquakes. We looked at the sensitivity of the extended faults in the CMG model. The extended faults act like a flow barrier which delays the flow communication across the faults, resulting the delay of the incremental energy peak. Lastly, we built an empirical seismological model using ACE algorithm and the seismological model suggests very low frequency of the earthquakes after 2015, given the operational conditions.

Recommendations

The followings are potential improvements from the proposed workflows in this dissertation.

1. The current injection phase modeling using pressure-dependent fracture properties cannot account for the effect of pressure depletion in fracture propagation (e.g. the change of maximum horizontal stress direction and the increase in stress anisotropy impacting fracture propagation). To incorporate these aspects, the proposed method should benchmark such cases with rigorously coupled fluid flow and geomechanical simulations.
2. The hydraulic fractures are demonstrated in tartan gridding throughout the dissertation. To add more flexibility in fracture geometry, unstructured grid and embedded discrete fracture model (EDFM) can be considered for future development to potentially account for complex geometry, interacting with existing natural fractures.
3. There is more information becoming available from unconventional reservoirs. With the advent of fiber optic sensors, distributed temperature sensing (DTS)

and distributed acoustic sensing (DAS) allow us to obtain temperature and deformation distributions around a completed well. Utilizing DTS and DAS would help better characterize hydraulic fractures and assess hydraulically fractured shale well performance.

4. The friction coefficient in Mohr-Coulomb failure criterion is set to be a constant in this study. There is evidence in the literature that the friction coefficient can be a dynamic value depending on state or slip-rate. In the future study, it would be interesting to see the impact of dynamic friction coefficient on the fault frictional energy.

REFERENCES

Baek, S., Akkutlu, I.Y., Lu, B., Ding, S. and Xia, W., 2019. Shale Gas Well Production Optimization using Modified RTA Method-Prediction of the Life of a Well. Unconventional Resources Technology Conference (URTEC).

Bandis, S., Lumsden, A. and Barton, N., 1983. Fundamentals of rock joint deformation, International Journal of Rock Mechanics and Mining Sciences & Geomechanics Abstracts. Elsevier, pp. 249-268.

Bansal, N., Han, J., Shin, Y. and Blasingame, T., 2018. Reservoir Characterization to Understand Optimal Well Spacing – A Wolfcamp Case Study, SPE/AAPG/SEG Unconventional Resources Technology Conference. Unconventional Resources Technology Conference, Houston, Texas, USA, pp. 17.

Bao, X. and Eaton, D.W., 2016. Fault activation by hydraulic fracturing in western Canada. Science, 354(6318): 1406-1409.

Barton, N., Bandis, S. and Bakhtar, K., 1985. Strength, deformation and conductivity coupling of rock joints, International journal of rock mechanics and mining sciences & geomechanics abstracts. Elsevier, pp. 121-140.

Breiman, L. and Friedman, J.H., 1985. Estimating optimal transformations for multiple regression and correlation. Journal of the American statistical Association, 80(391): 580-598.

Byerlee, J., 1978. Friction of rocks, Rock friction and earthquake prediction. Springer, pp. 615-626.

Chang, C., 2017. Critical pore pressure assessment for CO 2 geological storage in Gyeongsang Basin, Korea, from a geomechanics perspective. Geosciences Journal, 21(4): 617-630.

Chang, K. and Segall, P., 2016a. Injection-induced seismicity on basement faults including poroelastic stressing. Journal of Geophysical Research: Solid Earth, 121(4): 2708-2726.

Chang, K.W. and Segall, P., 2016b. Seismicity on basement faults induced by simultaneous fluid injection–extraction. Pure and Applied Geophysics, 173(8): 2621-2636.

Chen, H. et al., 2020a. Fracture inference and optimal well placement using a multiscale history matching in a HPHT tight gas reservoir, Tarim Basin, China. Upstream Oil and Gas Technology, 2: 100002.

Chen, R., Xue, X., Datta-Gupta, A., Yu, H. and Kalyanaraman, N., 2019. The Impact of Cluster Spacing on Multi-Fractured Well Performance, SPE Liquids-Rich Basins Conference-North America. Society of Petroleum Engineers.

Chen, R., Xue, X., Park, J., Datta-Gupta, A. and King, M.J., 2020b. New insights into the mechanisms of seismicity in the Azle area, North Texas. Geophysics, 85(1): EN1-EN15.

Chen, Z., Jeffrey, R.G., Zhang, X. and Kear, J., 2017. Finite-Element Simulation of a Hydraulic Fracture Interacting With a Natural Fracture. SPE-163609-PA, 22(01): 219-234.

Chipperfield, S.T. et al., 2007. Shear Dilation Diagnostics: A New Approach for Evaluating Tight Gas Stimulation Treatments, SPE Hydraulic Fracturing Technology Conference. Society of Petroleum Engineers, College Station, Texas, U.S.A., pp. 15.

Cho, Y., Apaydin, O.G. and Ozkan, E., 2012. Pressure-Dependent Natural-Fracture Permeability in Shale and its Effect on Shale-Gas Well Production, SPE Annual Technical Conference and Exhibition. Society of Petroleum Engineers, San Antonio, Texas, USA, pp. 18.

Cipolla, C.L., 2009. Modeling Production and Evaluating Fracture Performance in Unconventional Gas Reservoirs. SPE-118536-JPT, 61(09): 84-90.

Cipolla, C.L., Fitzpatrick, T., Williams, M.J. and Ganguly, U.K., 2011. Seismic-to-simulation for unconventional reservoir development, SPE Reservoir Characterisation and Simulation Conference and Exhibition. Society of Petroleum Engineers.

Computer Modeling Group, 2018. Computer Modelling Group Ltd.; "Enhance & Accelerate Sensitivity Analysis, History Matching, Optimization & Uncertainty Analysis". *CMG CMOST User Guide*(Version 2016).

Datta-Gupta, A., Xie, J., Gupta, N., King, M.J. and Lee, W.J., 2011. Radius of Investigation and its Generalization to Unconventional Reservoirs. SPE-118536-JPT, 63(07): 52-55.

Davies, J.P. and Davies, D.K., 1999. Stress-Dependent Permeability: Characterization and Modeling, SPE Annual Technical Conference and Exhibition. Society of Petroleum Engineers, Houston, Texas, pp. 16.

Dempsey, D., Kelkar, S., Davatzes, N., Hickman, S. and Moos, D., 2015. Numerical modeling of injection, stress and permeability enhancement during shear stimulation at the Desert Peak Enhanced Geothermal System. International Journal of Rock Mechanics and Mining Sciences, 78: 190-206.

Dieterich, J.H., 1978. Time-dependent friction and the mechanics of stick-slip, Rock friction and earthquake prediction. Springer, pp. 790-806.

Dieterich, J.H., 1979. Modeling of rock friction: 1. Experimental results and constitutive equations. Journal of Geophysical Research: Solid Earth, 84(B5): 2161-2168.

Economides, M.J. and Nolte, K.G., 1989. Reservoir stimulation, 2. Prentice Hall Englewood Cliffs, NJ.

EIA, 2019. U.S. Crude Oil and Natural Gas Proved Reserves, Year-End 2018, U.S. Energy Information Publication report.

Ellsworth, W.L., 2013. Injection-induced earthquakes. Science, 341(6142).

Elsworth, D., Spiers, C.J. and Niemeijer, A.R., 2016. Understanding induced seismicity. Science, 354(6318): 1380-1381.

Enverus, 2019. Online research queries (www.enverus.com).

Ertekin, T. and Sun, Q., 2019. Artificial Intelligence Applications in Reservoir Engineering: A Status Check. Energies, 12(15): 2897.

Fenwick, D., Scheidt, C. and Caers, J., 2014. Quantifying asymmetric parameter interactions in sensitivity analysis: application to reservoir modeling. Mathematical Geosciences, 46(4): 493-511.

Ferrill, D.A. et al., 2017. Mechanical stratigraphy and normal faulting. Journal of Structural Geology, 94: 275-302.

Ferrill, D.A., Smart, K.J. and Morris, A.P., 2020. Fault failure modes, deformation mechanisms, dilation tendency, slip tendency, and conduits v. seals. Geological Society, London, Special Publications, 496(1): 75-98.

Finkbeiner, T., Zoback, M., Flemings, P. and Stump, B., 2001. Stress, pore pressure, and dynamically constrained hydrocarbon columns in the South Eugene Island 330 field, northern Gulf of Mexico. AAPG bulletin, 85(6): 1007-1031.

Frohlich, C., 2012. Two-year survey comparing earthquake activity and injection-well locations in the Barnett Shale, Texas. Proceedings of the National Academy of Sciences, 109(35): 13934-13938.

Frohlich, C. et al., 2016. A historical review of induced earthquakes in Texas. Seismological Research Letters, 87(4): 1022-1038.

Ghanizadeh*, A. et al., 2016. Unpropped/propped fracture permeability and proppant embedment evaluation: A rigorous core-analysis/imaging methodology, Unconventional Resources Technology Conference, San Antonio, Texas, 1-3 August 2016. Society of Exploration Geophysicists, American Association of Petroleum …, pp. 1824-1852.

Gidley, J.L., 1989. Recent advances in hydraulic fracturing, Society of Petroleum Monograph Series Vol. 12.

Goertz-Allmann, B.P., Goertz, A. and Wiemer, S., 2011. Stress drop variations of induced earthquakes at the Basel geothermal site. Geophysical Research Letters, 38(9).

Gono, V., Olson, J.E. and Gale, J.F., 2015. Understanding the correlation between induced seismicity and wastewater injection in the Fort Worth basin, 49th US Rock Mechanics/Geomechanics Symposium. American Rock Mechanics Association.

Gonzalez-Chavez, M., Dahi Taleghani, A. and Olson, J.E., 2015. A Cohesive Model for Modeling Hydraulic Fractures in Naturally Fractured Formations, SPE Hydraulic Fracturing Technology Conference. Society of Petroleum Engineers, The Woodlands, Texas, USA, pp. 16.

Goodman, R.E., 1989. Introduction to rock mechanics, 2. Wiley New York.

Guglielmi, Y., Cappa, F., Avouac, J.-P., Henry, P. and Elsworth, D., 2015. Seismicity triggered by fluid injection–induced aseismic slip. Science, 348(6240): 1224-1226.

Guo, X., Wu, K., An, C., Tang, J. and Killough, J., 2019. Numerical Investigation of Effects of Subsequent Parent-Well Injection on Interwell Fracturing Interference Using Reservoir-Geomechanics-Fracturing Modeling. SPE-163609-PA, 24(04): 1,884-1,902.

Haddad, M., Du, J. and Vidal-Gilbert, S., 2017. Integration of Dynamic Microseismic Data With a True 3D Modeling of Hydraulic-Fracture Propagation in the Vaca Muerta Shale. SPE-163609-PA, 22(06): 1714-1738.

Haddad, M. and Sepehrnoori, K., 2014. Simulation of Multiple-Stage Fracturing in Quasibrittle Shale Formations Using Pore Pressure Cohesive Zone Model, SPE/AAPG/SEG Unconventional Resources Technology Conference. Unconventional Resources Technology Conference, Denver, Colorado, USA, pp. 16.

Hennings, P.H. et al., 2019. Injection-induced seismicity and fault-slip potential in the Fort Worth Basin, Texas. Bulletin of the Seismological Society of America, 109(5): 1615-1634.

Hetz, G. et al., 2017. History Matching of Frequent Seismic Surveys Using Seismic Onset Times at the Peace River Field, Canada, SPE Annual Technical Conference and Exhibition. Society of Petroleum Engineers.

Hornbach, M.J. et al., 2015. Causal factors for seismicity near Azle, Texas. Nature Communications, 6(1): 1-11.

Hornbach, M.J. et al., 2016. Ellenburger wastewater injection and seismicity in North Texas. Physics of the Earth and Planetary Interiors, 261: 54-68.

Huang, J., Datta-Gupta, A. and Augustine, J.R., 2017. Optimization of Hydraulic Fracture Development and Well Performance Using Limited Entry Perforations, SPE Oklahoma City Oil and Gas Symposium. Society of Petroleum Engineers, Oklahoma City, Oklahoma, USA, pp. 16.

Huang, J., Yang, C., Xue, X. and Datta-Gupta, A., 2016. Simulation of Coupled Fracture Propagation and Well Performance under Different Refracturing Designs in Shale Reservoirs, SPE Low Perm Symposium. Society of Petroleum Engineers, Denver, Colorado, USA, pp. 26.

Iino, A., Onishi, T. and Datta-Gupta, A., 2019. Optimizing CO 2-and Field-Gas-Injection EOR in Unconventional Reservoirs Using the Fast-Marching Method. SPE-187116-PA.

Iino, A. et al., 2017a. Efficient Modeling and History Matching of Shale Oil Reservoirs Using the Fast Marching Method: Field Application and Validation, SPE Western Regional Meeting. Society of Petroleum Engineers, Bakersfield, California, pp. 28.

Iino, A. et al., 2017b. Rapid Compositional Simulation and History Matching of Shale Oil Reservoirs Using the Fast Marching Method, SPE/AAPG/SEG Unconventional Resources Technology Conference. Unconventional Resources Technology Conference, Austin, Texas, USA, pp. 21.

Jha, B. and Juanes, R., 2014. Coupled multiphase flow and poromechanics: A computational model of pore pressure effects on fault slip and earthquake triggering. Water Resources Research, 50(5): 3776-3808.

Ji, L., Sen, V., Min, K.S. and Sullivan, R., 2019. Numerical Simulation of DFITs Within a Coupled Reservoir Flow and Geomechanical Simulator - Insights Into

Completions Optimization, SPE Hydraulic Fracturing Technology Conference and Exhibition. Society of Petroleum Engineers, The Woodlands, Texas, USA, pp. 18.

Ji, L., Settari, A.T., Sullivan, R.B. and Orr, D., 2004. Methods For Modeling Dynamic Fractures In Coupled Reservoir And Geomechanics Simulation, SPE Annual Technical Conference and Exhibition. Society of Petroleum Engineers, Houston, Texas, pp. 9.

Jo, H., Santos, J.E. and Pyrcz, M.J., 2020. Conditioning well data to rule-based lobe model by machine learning with a generative adversarial network. Energy Exploration & Exploitation, 38(6): 2558-2578.

Kam, P., Nadeem, M., Novlesky, A., Kumar, A. and Omatsone, E.N., 2015. Reservoir characterization and history matching of the Horn River shale: An integrated geoscience and reservoir-simulation approach. Journal of Canadian Petroleum Technology, 54(06): 475-488.

Kanamori, H., 1977. The energy release in great earthquakes. Journal of Geophysical Research, 82(20): 2981-2987.

Kanfar, M. and Wattenbarger, R., 2012. Comparison of empirical decline curve methods for shale wells, SPE Canadian Unconventional Resources Conference. Society of Petroleum Engineers.

Keranen, K.M., Savage, H.M., Abers, G.A. and Cochran, E.S., 2013. Potentially induced earthquakes in Oklahoma, USA: Links between wastewater injection and the 2011 Mw 5.7 earthquake sequence. Geology, 41(6): 699-702.

Keranen, K.M. and Weingarten, M., 2018. Induced seismicity. Annual Review of Earth and Planetary Sciences, 46: 149-174.

Keshavarz, A., Badalyan, A., Carageorgos, T., Bedrikovetsky, P. and Johnson Jr, R., 2015. Stimulation of coal seam permeability by micro-sized graded proppant placement using selective fluid properties. Fuel, 144: 228-236.

Keshavarz, A., Yang, Y., Badalyan, A., Johnson, R. and Bedrikovetsky, P., 2014. Laboratory-based mathematical modelling of graded proppant injection in CBM reservoirs. International Journal of Coal Geology, 136: 1-16.

Kim, H., Olalotiti-Lawal, F. and Datta-Gupta, A., 2019. Multi-Resolution Grid Connectivity-Based Transform for Efficient History Matching of Unconvetional Reservoirs, SPE/AAPG/SEG Unconventional Resources Technology Conference. Unconventional Resources Technology Conference, Denver, Colorado, USA.

Kozlowski, K. et al., 2018. The Importance of Overburden and Pore Pressure on Horizontal Stress Magnitude Determination; an Example From the Delaware Basin, SPE/AAPG/SEG Unconventional Resources Technology Conference. Unconventional Resources Technology Conference, Houston, Texas, USA, pp. 15.

Langenbruch, C., Weingarten, M. and Zoback, M.D., 2018. Physics-based forecasting of man-made earthquake hazards in Oklahoma and Kansas. Nature Communications, 9(1): 1-10.

Lee, H. and Cho, T., 2002. Hydraulic characteristics of rough fractures in linear flow under normal and shear load. Rock Mechanics and Rock Engineering, 35(4): 299-318.

Lee, H., Ong, S.H., Azeemuddin, M. and Goodman, H., 2012. A wellbore stability model for formations with anisotropic rock strengths. Journal of Petroleum Science and Engineering, 96: 109-119.

Lee, J., 1982. Well testing. Society of Petroleum Engineers.

Lele, S. et al., 2015. Groningen 2015 geomechanical analysis. Final Report. Exxon Mobiel Upstream Research Company (Spring TX, USA)/NAM (Assen).

Lele, S.P. et al., 2016. Geomechanical modeling to evaluate production-induced seismicity at Groningen field, Abu Dhabi International Petroleum Exhibition & Conference. Society of Petroleum Engineers.

Liang, B., Du, M. and Yanez, P.P., 2019. Subsurface well spacing optimization in the Permian Basin. Journal of Petroleum Science and Engineering, 174: 235-243.

Liu, L., Liu, Y., Yao, J. and Huang, Z., 2020. Efficient Coupled Multiphase-Flow and Geomechanics Modeling of Well Performance and Stress Evolution in Shale-Gas Reservoirs Considering Dynamic Fracture Properties. SPE-163609-PA.

Liu, M. et al., 2016. A wellbore stability model for a deviated well in a transversely isotropic formation considering poroelastic effects. Rock Mechanics and Rock Engineering, 49(9): 3671-3686.

Lu, Y., Rajora, M., Zou, P. and Liang, S.Y., 2017. Physics-embedded machine learning: case study with electrochemical micro-machining. Machines, 5(1): 4.

Maucec, M. et al., 2015. Multivariate analysis and data Mining of Well-Stimulation Data by use of classification-and-regression tree with enhanced interpretation and prediction capabilities. SPE Economics & Management, 7(02): 60-71.

McGarr, A., Simpson, D., Seeber, L. and Lee, W., 2002. Case histories of induced and triggered seismicity. International Geophysics Series, 81(A): 647-664.

Min, K.-B., Rutqvist, J., Tsang, C.-F. and Jing, L., 2004. Stress-dependent permeability of fractured rock masses: a numerical study. International Journal of Rock Mechanics and Mining Sciences, 41(7): 1191-1210.

Min, K.S., Sen, V., Ji, L. and Sullivan, R.B., 2018. Optimization of Completion and Well Spacing for Development of Multi-Stacked Reservoirs Using Integration of Data Analytics, Geomechanics and Reservoir Flow Modeling, SPE/AAPG/SEG Unconventional Resources Technology Conference. Unconventional Resources Technology Conference, Houston, Texas, USA, pp. 11.

Mishra, S. and Datta-Gupta, A., 2017. Applied statistical modeling and data analytics: A practical guide for the petroleum geosciences. Elsevier.

Mittal, R., Oruganti, Y. and McBurney, C., 2015. Re-Fracturing Simulations: Pressure-Dependent SRV and Shear Dilation of Natural Fractures, Unconventional Resources Technology Conference. Unconventional Resources Technology Conference, San Antonio, Texas, USA, pp. 15.

Molinari, D., Sankaran, S., Symmons, D. and Perrotte, M., 2019. A Hybrid Data and Physics Modeling Approach Towards Unconventional Well Performance Analysis, SPE Annual Technical Conference and Exhibition. Society of Petroleum Engineers.

Nicot, J.-P., 2009. Assessment of industry water-use in the Barnett Shale gas play (Fort Worth Basin), Gulf Coast Association of Geological Socieities Transactions, 59: 539-551.

Nordgren, R., 1972. Propagation of a vertical hydraulic fracture. Society of Petroleum Engineers Journal, 12(04): 306-314.

Park, J., Datta-Gupta, A., Singh, A. and Sankaran, S., 2020a. Hybrid Physics and Data-Driven Modeling for Unconventional Field Development–Onshore US Basin Case Study. Unconventional Resources Technology Conference (URTEC).

Park, J., Datta-Gupta, A., Singh, A. and Sankaran, S., 2020b. Hybrid Physics and Data-Driven Modeling for Unconventional Field Development – Onshore US Basin Case Study, SPE/AAPG/SEG Unconventional Resources Technology Conference. Unconventional Resources Technology ConferenceAustin, Texas, USA, pp. 22.

Park, J., Iino, A., Datta-Gupta, A., Bi, J. and Sankaran, S., 2019a. Rapid modeling of injection and production phases of hydraulically fractured shale wells using the fast marching method. Unconventional Resources Technology Conference (URTEC).

Park, J., Iino, A., Datta-Gupta, A., Bi, J. and Sankaran, S., 2019b. Rapid Modeling of Injection and Production Phases of Hydraulically Fractured Shale Wells using the Fast Marching Method, SPE/AAPG/SEG Unconventional Resources Technology Conference. Unconventional Resources Technology Conference, Denver, Colorado, USA.

Park, J., Iino, A., Datta-Gupta, A., Bi, J. and Sankaran, S., 2020c. Novel hybrid fast marching method-based simulation workflow for rapid history matching and completion design optimization of hydraulically fractured shale wells. Journal of Petroleum Science and Engineering, 196: 107718.

Park, J. and Janova, C., 2019. SRV Characterization and Optimum Lateral Well Spacing Study of Two-well Pad in Midland Basin, SPE/AAPG/SEG Unconventional Resources Technology Conference. Unconventional Resources Technology Conference, Denver, Colorado, USA, pp. 17.

Park, J. and Janova, C., 2020. Stimulated Reservoir Volume Characterization and Optimum Lateral Well Spacing Study of Two-Well Pad: Midland Basin Case Study. Geofluids, 2020.

Park, J. and Kim, J., 2016. Importance of Fluid Compressibility and Multi-Phase Flow in Numerical Modeling of Hydraulic Fracture Propagation, 50th U.S. Rock Mechanics/Geomechanics Symposium. American Rock Mechanics Association, Houston, Texas, pp. 8.

Park, J., Yang, G., Satija, A., Scheidt, C. and Caers, J., 2016. DGSA: A Matlab toolbox for distance-based generalized sensitivity analysis of geoscientific computer experiments. Computers & geosciences, 97: 15-29.

Parker, J., Bazan, L.W., Tran, V.P., White, R. and Lattibeaudiere, M.G., 2015. Technology Integration: A Methodology to Enhance Production in Horizontal Wolfcamp Shale Wells in the Delaware Basin, SPE Liquids-Rich Basins Conference - North America. Society of Petroleum Engineers, Midland, Texas, USA, pp. 32.

Pedregosa, F. et al., 2011. Scikit-learn: Machine learning in Python. the Journal of machine Learning research, 12: 2825-2830.

Perkins, T. and Kern, L., 1961. Widths of hydraulic fractures. SPE-118536-JPT, 13(09): 937-949.

Pieters, D.A. and Graves, R.M., 1994. Fracture Relative Permeability: Linear or Non-Linear Function of Saturation, International Petroleum Conference and Exhibition of Mexico. Society of Petroleum Engineers, Veracruz, Mexico, pp. 10.

Pogacnik, J., Elsworth, D., O'Sullivan, M. and O'Sullivan, J., 2016. A damage mechanics approach to the simulation of hydraulic fracturing/shearing around a geothermal injection well. Computers and Geotechnics, 71: 338-351.

Quinones, L. et al., 2019. Tracking Induced Seismicity in the Fort Worth Basin: A Summary of the 2008–2018 North Texas Earthquake Study CatalogTracking Induced Seismicity in the FWB: A Summary of the 2008–2018 North Texas Earthquake Study Catalog. Bulletin of the Seismological Society of America, 109(4): 1203-1216.

Railroad Commission of Texas, 2015a. Commission called hearing to consider whether operation of the Enervest Operating Llc, Briar Lease, Well No. 1 (Api No. 42-497-36875, Uic Permit No. 12112), in the Couglin (Strawn) field, is causing or contributing to seismic activity in the vicinity of Reno, Parker County, Texas.

Railroad Commission of Texas, 2015b. Commission called hearing to consider whether operation of the XTO Energy, Inc., West Lake Swd, Well No. 1 (Api No. 42-367-34693, Uic Permit No. 12872), in the Newark, East (Barnett Shale) field, is causing or contributing to seismic activity in the vicinity of Reno, Parker County, Texas.

Railroad Commission of Texas, 2019a. H10 Filling System.

Railroad Commission of Texas, 2019b. Online research queries.

Raleigh, C., Healy, J. and Bredehoeft, J., 1976. An experiment in earthquake control at Rangely, Colorado. Science, 191(4233): 1230-1237.

Reasenberg, P.A. and Simpson, R.W., 1992. Response of regional seismicity to the static stress change produced by the Loma Prieta earthquake. Science, 255(5052): 1687-1690.

Ruina, A., 1983. Slip instability and state variable friction laws. Journal of Geophysical Research: Solid Earth, 88(B12): 10359-10370.

Rutqvist, J. et al., 2016. Fault activation and induced seismicity in geological carbon storage–Lessons learned from recent modeling studies. Journal of Rock Mechanics and Geotechnical Engineering, 8(6): 789-804.

Rutqvist, J. and Tsang, C.-F., 2002. A study of caprock hydromechanical changes associated with CO 2-injection into a brine formation. Environmental Geology, 42(2-3): 296-305.

Saad, I.B., 2013. Selecting Material Parameters in Abaqus for Cohesive Elements Defined in Terms Of Traction-Separation. Dassault Systemes Simulia Corp.

Samnejad, M., Aminzadeh, F. and Jha, B., 2017. Simulation of Hydraulic Fracturing-Induced Permeability Stimulation Using Coupled Flow and Continuum Damage Mechanics, SPE Annual Technical Conference and Exhibition. Society of Petroleum Engineers, San Antonio, Texas, USA, pp. 16.

Santos, J.E. et al., 2020. PoreFlow-Net: A 3D convolutional neural network to predict fluid flow through porous media. Advances in Water Resources, 138: 103539.

Scholz, C.H., 1998. Earthquakes and friction laws. Nature, 391(6662): 37-42.

Schuetter, J., Mishra, S., Zhong, M. and LaFollette, R., 2018. A data-analytics tutorial: Building predictive models for oil production in an unconventional shale reservoir. SPE-163609-PA, 23(04): 1,075-1,089.

Segall, P., 1989. Earthquakes triggered by fluid extraction. Geology, 17(10): 942-946.

Segall, P., Grasso, J.R. and Mossop, A., 1994. Poroelastic stressing and induced seismicity near the Lacq gas field, southwestern France. Journal of Geophysical Research: Solid Earth, 99(B8): 15423-15438.

Segall, P. and Lu, S., 2015. Injection-induced seismicity: Poroelastic and earthquake nucleation effects. Journal of Geophysical Research: Solid Earth, 120(7): 5082-5103.

Sen, V., Min, K.S., Ji, L. and Sullivan, R., 2018. Completions and Well Spacing Optimization by Dynamic SRV Modeling for Multi-Stage Hydraulic Fracturing, SPE Annual Technical Conference and Exhibition. Society of Petroleum Engineers, Dallas, Texas, USA, pp. 11.

Sethian, J.A., 1996. A fast marching level set method for monotonically advancing fronts. Proceedings of the National Academy of Sciences, 93(4): 1591-1595.

Sethian, J.A., 1999. Fast marching methods. SIAM review, 41(2): 199-235.

Shin, D.H. and Sharma, M.M., 2014. Factors Controlling the Simultaneous Propagation of Multiple Competing Fractures in a Horizontal Well, SPE Hydraulic Fracturing Technology Conference. Society of Petroleum Engineers, The Woodlands, Texas, USA, pp. 20.

Simpson, R.W., 1997. Quantifying Anderson's fault types. Journal of Geophysical Research: Solid Earth, 102(B8): 17909-17919.

Singh, A.P., 2016. Forecasting Production Data for Existing Wells and New Wells. US Patent Application, 14/646/688.

Sneddon, I. and Elliot, H., 1946. The opening of a Griffith crack under internal pressure. Quarterly of Applied Mathematics, 4(3): 262-267.

Snee, J.E.L. and Zoback, M.D., 2016. State of stress in Texas: Implications for induced seismicity. Geophysical Research Letters, 43(19): 10,208-10,214.

Song, B. and Ehlig-Economides, C.A., 2011. Rate-normalized pressure analysis for determination of shale gas well performance, North American unconventional gas conference and exhibition. Society of Petroleum Engineers.

Stein, R.S., 1999. The role of stress transfer in earthquake occurrence. Nature, 402(6762): 605-609.

Stesky, R., Brace, W., Riley, D. and Robin, P.-Y., 1974. Friction in faulted rock at high temperature and pressure. Tectonophysics, 23(1-2): 177-203.

Tang, C., Tham, L., Lee, P., Yang, T. and Li, L., 2002. Coupled analysis of flow, stress and damage (FSD) in rock failure. International Journal of Rock Mechanics and Mining Sciences, 39(4): 477-489.

Tchelepi, H.A. and Fuks, O., 2020. Limitations of physics informed machine learning for nonlinear two-phase transport in porous media. Journal of Machine Learning for Modeling and Computing, 1(1).

Urpi, L., Rinaldi, A.P., Rutqvist, J., Cappa, F. and Spiers, C.J., 2016. Dynamic simulation of CO2-injection-induced fault rupture with slip-rate dependent friction coefficient. Geomechanics for Energy and the Environment, 7: 47-65.

Valkó, P.P. and Lee, W.J., 2010. A better way to forecast production from unconventional gas wells, SPE annual technical conference and exhibition. Society of Petroleum Engineers.

Vasco, D., Keers, H. and Karasaki, K., 2000. Estimation of reservoir properties using transient pressure data: An asymptotic approach. Water Resources Research, 36(12): 3447-3465.

Vasco, D.W. and Datta-Gupta, A., 2016. Subsurface Fluid Flow and Imaging: With Applications for Hydrology, Reservoir Engineering, and Geophysics. Cambridge University Press.

Walsh, F., Zoback, M., Pais, D., Weingartern, M. and Tyrell, T., 2017. FSP 1.0: A program for probabilistic estimation of fault slip potential resulting from fluid injection. User Guide from the Stanford Center for Induced and Triggered Seismicity.

Wang, H., Marongiu-Porcu, M. and Economides, M.J., 2016. Poroelastic and Poroplastic Modeling of Hydraulic Fracturing in Brittle and Ductile Formations. SPE-174869-PA, 31(01): 47-59.

Wang, J.-A. and Park, H., 2002. Fluid permeability of sedimentary rocks in a complete stress–strain process. Engineering Geology, 63(3-4): 291-300.

Wattenbarger, R.A., El-Banbi, A.H., Villegas, M.E. and Maggard, J.B., 1998. Production analysis of linear flow into fractured tight gas wells, SPE rocky mountain regional/low-permeability reservoirs symposium. Society of Petroleum Engineers.

Winterfeld, P.H. and Wu, Y.-S., 2011. Parallel simulation of CO2 sequestration with rock deformation in saline aquifers, SPE Reservoir Simulation Symposium. Society of Petroleum Engineers.

Wiprut, D. and Zoback, M.D., 2000. Fault reactivation and fluid flow along a previously dormant normal fault in the northern North Sea. Geology, 28(7): 595-598.

Witherspoon, P.A., Wang, J.S., Iwai, K. and Gale, J.E., 1980. Validity of cubic law for fluid flow in a deformable rock fracture. Water Resources Research, 16(6): 1016-1024.

Wu, Y.-S. et al., 2014a. Simulation of coupled processes of flow, transport, and storage of CO2 in saline aquifers, Colorado School of Mines, Golden, CO (United States).

Wu, Y.-S., Li, J., Ding, D., Wang, C. and Di, Y., 2014b. A Generalized Framework Model for the Simulation of Gas Production in Unconventional Gas Reservoirs. SPE-163609-PA, 19(05): 845-857.

Xie, J., Yang, C., Gupta, N., King, M.J. and Datta-Gupta, A., 2015. Integration of Shale-Gas-Production Data and Microseismic for Fracture and Reservoir Properties With the Fast Marching Method. SPE-163609-PA, 20(02): 347-359.

Xiong, H., Liu, S., Feng, F., Liu, S. and Yue, K., 2019. Optimizing Fracturing Design and Well Spacing with Complex-Fracture and Reservoir Simulations: A Permian Basin Case Study. SPE-174869-PA.

Xue, G., Datta-Gupta, A., Valko, P. and Blasingame, T., 1997. Optimal transformations for multiple regression: application to permeability estimation from well logs. SPE Formation Evaluation, 12(02): 85-94.

Xue, X., Yang, C., Onishi, T., King, M.J. and Datta-Gupta, A., 2019a. Modeling Hydraulically Fractured Shale Wells Using the Fast Marching Method with Local Grid Refinements LGRs and Embedded Discrete Fracture Model EDFM, SPE Reservoir Simulation Conference. Society of Petroleum Engineers.

Xue, X. et al., 2018. Reservoir and Fracture-Flow Characterization Using Novel Diagnostic Plots. SPE-163609-PA, Preprint(Preprint): 22.

Xue, X. et al., 2019b. Reservoir and fracture-flow characterization using novel diagnostic plots. SPE-163609-PA, 24(03): 1,248-1,269.

Yang, C., Sharma, V.K., Datta-Gupta, A. and King, M.J., 2017a. Novel approach for production transient analysis of shale reservoirs using the drainage volume derivative. Journal of Petroleum Science and Engineering, 159: 8-24.

Yang, C., Vyas, A., Datta-Gupta, A., Ley, S.B. and Biswas, P., 2017b. Rapid multistage hydraulic fracture design and optimization in unconventional reservoirs using a novel Fast Marching Method. Journal of Petroleum Science and Engineering, 156: 91-101.

Yang, C., Xue, X., King, M.J. and Datta-Gupta, A., 2017c. Flow Simulation of Complex Fracture Systems With Unstructured Grids Using the Fast Marching Method, SPE/AAPG/SEG Unconventional Resources Technology Conference. Unconventional Resources Technology Conference, Austin, Texas, USA, pp. 18.

Yao, Y., 2012. Linear elastic and cohesive fracture analysis to model hydraulic fracture in brittle and ductile rocks. Rock Mechanics and Rock Engineering, 45(3): 375-387.

Ye, Z. and Ghassemi, A., 2020. Heterogeneous Fracture Slip and Aseismic-Seismic Transition in a Triaxial Injection Test. Geophysical Research Letters, 47(14): e2020GL087739.

Zhai, G. and Shirzaei, M., 2018. Fluid injection and time-dependent seismic hazard in the Barnett Shale, Texas. Geophysical Research Letters, 45(10): 4743-4753.

Zhang, G., Liu, H., Zhang, J., Wu, H. and Wang, X., 2010. Three-dimensional finite element simulation and parametric study for horizontal well hydraulic fracture. Journal of Petroleum Science and Engineering, 72(3-4): 310-317.

Zhang, R., Jiang, Z., Sun, Q. and Zhu, S., 2013. The relationship between the deformation mechanism and permeability on brittle rock. Natural Hazards, 66(2): 1179-1187.

Zhang, Y. et al., 2016. From Streamlines to Fast Marching: Rapid Simulation and Performance Assessment of Shale-Gas Reservoirs by Use of Diffusive Time of Flight as a Spatial Coordinate. SPE-163609-PA, 21(05): 1883-1898.

Zhang, Y. et al., 2018. A Physics-Based Data-Driven Model for History Matching, Prediction, and Characterization of Unconventional Reservoirs. SPE-163609-PA, 23(04): 1105-1125.

Zhu, J., Forrest, J., Xiong, H. and Kianinejad, A., 2017. Cluster Spacing and Well Spacing Optimization Using Multi-Well Simulation for the Lower Spraberry Shale in Midland Basin, SPE Liquids-Rich Basins Conference - North America. Society of Petroleum Engineers, Midland, Texas, USA, pp. 14.

Zimmerman, R.W. and Yeo, I.W., 2000. Fluid flow in rock fractures: From the Navier-Stokes equations to the cubic law. Geophysical Monograph-American Geophysical Union, 122: 213-224.

Zoback, M.D., 2010. Reservoir geomechanics. Cambridge University Press.

APPENDIX A

BARTON-BANDIS MODEL MODIFICATION

The original paper (Barton et al., 1985) describes the decrease in the fracture permeability as the fracture closes under the normal stress. The present study modified the original equation such that the fracture permeability reduction follows multiple paths which is more applicable to hydraulic fractures with proppant embedded. The following derivation tries to honor the original notation as much as possible.

The joint closure model based on the large body of experimental data is introduced as follows (Equation 6 in the original paper),

$$\sigma_n^{'} = \frac{\Delta V_j}{a - b\Delta V_j}, \tag{19}$$

where $\sigma_n^{'}$ is the effective normal stress, and ΔV_j is the fracture closure under effective normal stress, and a and b are constants. The inverse of a is equal to the normal fracture stiffness, K_n, and a/b is the maximum possible fracture closure, V_m. If the above equation is rearranged in terms of the joint closure, now we have

$$\Delta V_j = \frac{\sigma_n^{'}}{K_n + \sigma_n^{'}/V_m}. \tag{20}$$

The original paper mentions that changes of the mechanical aperture, ΔV_j, can be coupled with fracture conductivity using Equation 4, 5, and 7 in the original paper which are

$$e = \left(12k\right)^{0.5}, \tag{21}$$

$$w = JRC^{2.5} / \left(E / w\right)^{2} \ \mu m, \tag{22}$$

$$E = E_0 - \Delta E, \tag{23}$$

respectively. In the equations, k is the conductivity in units of length squared (=permeability), e is the conducting aperture, E is the mechanical aperture, E_0 is the initial aperture and JRC is the joint roughness coefficient. Note that ΔE is equivalent to ΔV_j in Equation (20) and Equation (21) is simply the cubic law. Equation (22) is the empirical correlation based on the observation from the Fig 4 in the original paper and it is only valid for $E \geq e$. Combining Equation (21) and (22), the permeability can be written in terms of the aperture as follows

$$k = \frac{E^4}{12 JRC^5}, \tag{24}$$

and given the initial aperture, the initial permeability can be written as

$$k_0 = \frac{{E_0}^4}{12 JRC^5}. \tag{25}$$

Canceling out the numerator, the permeability reduction from the initial permeability is described as

$$k = k_0 \left(\frac{E}{E_0}\right)^4, \tag{26}$$

Note that E decreases from E_0 governed by Equation (20).

Equation (26) is the form that is utilized in commercial reservoir simulators to describe fracture permeability reduction using the Barton-Bandis model. For example, CMG STAR, which is coupled fluid flow and geomechanics simulator, utilizes the Barton-Bandis model (GPERMBB is the keyword) in the form of

$$k_f = kccf\left(\frac{e_{CMG}}{e_{CMG\_0}}\right)^4, \tag{27}$$

where k_f is the fracture closure permeability, $kccf$ is the fracture closure permeability which is the initial fracture permeability in Equation (25), e_{CMG} is the fracture aperture, and e_{CMG_0} is the initial fracture aperture in CMG. Note that e_{CMG} and e_{CMG_0} in Equation (27) are identical to E and E_0 in Equation (26).

Both Equation (26) and (27) demonstrate the fracture closure permeability degradation which follows a single path because of the V_m in the original paper. For example, CMG STAR defines the residual fracture closure permeability when ΔE in Equation (23) is equal to V_m meaning that the fracture permeability always converges to the residual permeability. However, this might not be the case for hydraulically fractured wells. Depending on retained fracture permeability with proppant embedded, the initial fracture permeability decreases along multiple paths (Ghanizadeh* et al., 2016; Keshavarz et al., 2015; Keshavarz et al., 2014).

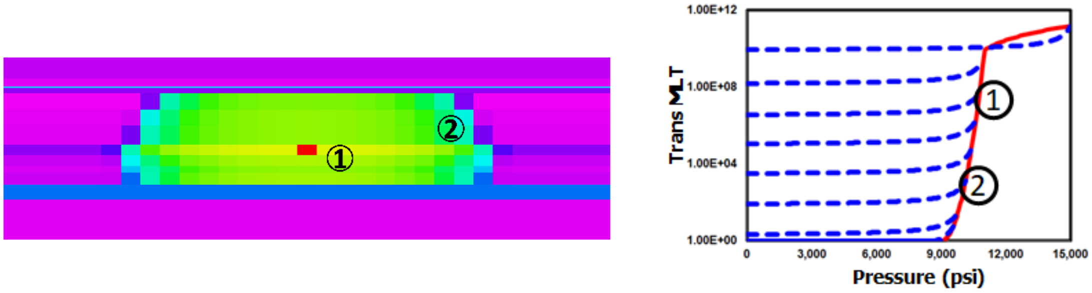

(a) (b)

Figure 80. The schematics of the retained permeability after hydraulic fracturing and resulting permeability reduction paths: (a) permeability after the hydraulic fracturing, (b) transmissibility multiplier curves

For example, Figure 80 shows the retained permeability after the hydraulic fracturing and transmissibility multiplier curves. The area close to the wellbore (indicated as 1) has higher retained permeability as compared to the area far away from the wellbore (indicated as 2). Depending on the retained permeability with proppant embedded, the permeability should be modeled such that the permeability decreases in multiple paths: the area 1 in Figure 80(a) follows the path 1 in Figure 80(b) and the permeability in the area 2 in Figure 80(a) decreases along the path 2 in Figure 80(b).

Therefore, the original equation is modified such that the permeability reduction follows multiple paths depending on the retained permeability after the stimulation. Assuming that the permeability when ΔE is equal to V_m is the residual fracture permeability, $k_{residual}$, then from Equation (26), V_m can be written as

$$V_m = E_0 \left[1 - \left(\frac{k_{residual}}{k_0} \right)^{1/4} \right] \tag{28}$$

Now, we define $k_{residual} / k_0$ as the residual permeability ratio, k_{rf} so that the residual permeability is proportional to the retained fracture permeability after the stimulation. Combining Equation (28) and Equation (20) leads to

$$\Delta V_j = \frac{\sigma_n^{'}\left(E_0 \times \left(1 - k_{rf}^{1/4}\right)\right)}{K_n\left(E_0 \times \left(1 - k_{rf}^{1/4}\right)\right) + \sigma_n^{'}} . \tag{29}$$

Now, Equation (23) is written as

$$E = E_0 - \frac{\sigma_n^{'}\left(E_0 \times \left(1 - k_{rf}^{1/4}\right)\right)}{K_n\left(E_0 \times \left(1 - k_{rf}^{1/4}\right)\right) + \sigma_n^{'}} = E_0\left(1 - \frac{\sigma_n^{'}\left(1 - k_{rf}^{1/4}\right)}{K_n\left(E_0 \times \left(1 - k_{rf}^{1/4}\right)\right) + \sigma_n^{'}}\right). \tag{30}$$

Finally, Equation (26) can be written in a permeability multiplier form as follows

$$\frac{k}{k_0} = \left(1 - \frac{\sigma_n^{'}\left(1 - k_{rf}^{1/4}\right)}{K_n\left(E_0 \times \left(1 - k_{rf}^{1/4}\right)\right) + \sigma_n^{'}}\right)^4 . \tag{31}$$

APPENDIX B

STRESS TENSOR TRANSFORMATION AND FAULT SLIP POTENTIAL CALCULATION

Stress Tensor Transformation

Stress components in 3D can be represented in tensor form. Therefore, by 2nd-order tensor transformation, the stress in a coordinate system can be transformed to another coordinate system. This stress transformation to represent the stress components in different coordinate systems is essential to assess fault slip. This is because in most cases, the fault plane might not be necessarily aligned with the principal stress (in-situ stress) directions where the principal stress directions might not be parallel with the global coordinate system (North, East, Downward) either. In this appendix, we follow the stress transformation concept in Lee et al. (2012); Liu et al. (2016) and the notations in Lee et al. (2012), which are originally used to evaluate wellbore stability in anisotropic formations. The underlying logic is identical and yet the analogy is that they investigated the failure of a depositional bedding plane while we consider the failure of an existing weak plane (i.e., fault plane).

We introduce three coordinate systems: in-situ stress coordinate system (ICS), global coordinate system (GCS), and weak plane coordinate system (WCS). For the transformation, GCS is the reference coordinate system where X_e is the North, Y_e is the East, and Z_e is vertically pointing down. This follows the convention that the principal stress direction and the weak plane geometry (e.g. dip and dip direction) are usually expressed by referencing GCS. Therefore, the principal stresses, normal stresses on three orthogonal planes when there are no shear stress components, along ICS are first mapped into GCS and the stresses then are projected onto WCS. The relationships between the coordinate systems are presented in Figure 81(a)-(b).

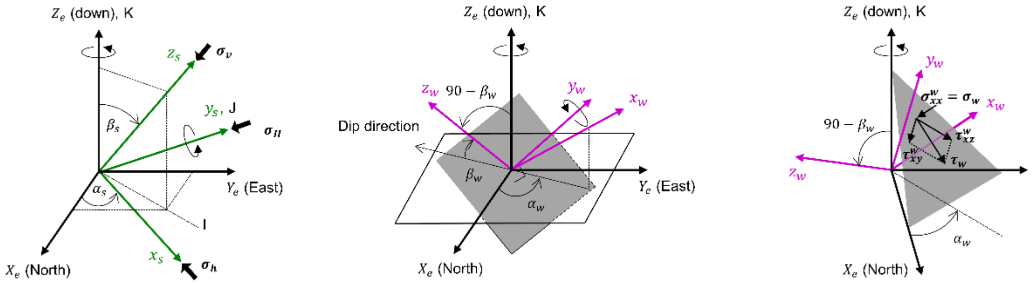

(a) (b) (c)

Figure 81. Relationships between coordinate systems and projected stresses on the weak plane: (a) relationship between GCS and ICS, (b) relationship between GCS and WCS, and (c) projected normal and shear stresses on the weak plane

Between coordinate systems, two angles help define the relationship. For example, between GCS and ICS (Figure 81(a)), the stress azimuth (α_S) measures the angle between the minimum horizontal stress direction (x_s) and the North (X_e). The stress deviation (β_S) defines the angle between the direction toward vertical down (Z_e) and the vertical stress direction (z_s). It is worth noting that most of petroleum engineering applications in deep subsurface assume that Z_e is parallel to z_s thus β_S is zero. The stresses in GCS, transformed from the principal stresses in ICS, are calculated by

$$\boldsymbol{\sigma}_\mathbf{g} = \mathbf{R}_{ItoG}^\mathbf{T} \boldsymbol{\sigma}_\mathbf{p} \mathbf{R}_{ItoG}, \tag{32}$$

where $\boldsymbol{\sigma}_{\mathbf{g}}$ is the stresses in GCS and $\boldsymbol{\sigma}_{\mathbf{p}}$ is the principal stresses defined as

$$\boldsymbol{\sigma}_{\mathbf{p}} = \begin{pmatrix} \sigma_H & 0 & 0 \\ 0 & \sigma_h & 0 \\ 0 & 0 & \sigma_v \end{pmatrix}, \tag{33}$$

and $\mathbf{R}_{ItoG}$ is the rotation matrix from ICS to GCS defined as

$$\mathbf{R}_{ItoG} = \begin{pmatrix} \cos\alpha_s \cos\beta_s & \sin\alpha_s \cos\beta_s & \sin\beta_s \\ -\sin\alpha_s & \cos\alpha_s & 0 \\ -\cos\alpha_s \sin\beta_s & -\sin\alpha_s \cos\beta_s & \cos\beta_s \end{pmatrix}. \tag{34}$$

The stress transformation from WCS to GCS follows a similar manner, described by two angles (Figure 81(b)). The dip direction – 180° (α_w) measures the angle between the North (X_e) and the projection of x_w on the horizontal plane. The dip angle (β_w) defines the angle between z_w axis and the horizontal plane. The rotation matrix from WCS to GCS, $\mathbf{R}_{WtoG}$, is

$$\mathbf{R}_{WtoG} = \begin{pmatrix} \cos\alpha_w \cos\beta_w & \sin\alpha_w \cos\beta_w & \sin\beta_w \\ -\sin\alpha_w & \cos\alpha_w & 0 \\ -\cos\alpha_w \sin\beta_w & -\sin\alpha_w \cos\beta_w & \cos\beta_w \end{pmatrix}. \tag{35}$$

The notation and configuration in Figure 81(b) are with reference to GCS. However, what we eventually need is the stresses in WCS. Thus, knowing that the rotation matrix is orthogonal, we transform the stresses from WCS to GCS by

$$\boldsymbol{\sigma}_{\mathbf{w}} = \mathbf{R}_{WtoG} \boldsymbol{\sigma}_{\mathbf{g}} \mathbf{R}_{WtoG}^{\mathbf{T}}, \tag{36}$$

where $\boldsymbol{\sigma}_{\mathbf{w}}$ is the stresses in WCS. Note that the sequence of the matrix multiplication in Eq.(32) Eq. (36) are different.

After the principal stresses are transformed into WCS, we can obtain the normal and shear stresses onto the weak plane. Figure 81(c) shows projected normal and shear stresses onto the weak plane where the normal stress (σ_w) is

$$\sigma_w = \sigma_{xx}^{w}, \tag{37}$$

and resultant shear stress (τ_w) is defined by Goodman (1989)

Fault Slip Potential Calculation

We can graphically analyze the shear failure of a rock or a weak plane using Mohr-Coulomb criterion. Given principal stresses, we can draw Mohr circle where $\sigma_3', \sigma_2',$ and σ_1' in Figure 82 indicate minimum, intermediate, and maximum principal stress, respectively. With rock or fault properties, we can draw the Coulomb failure line where the slope of the line is friction coefficient and y intercept is the cohesion, the intrinsic shear strength. If the circle touches the line in Figure 82(a), then there is a shear failure and slip in rock volume. For specific weak plane, the principal stresses can be projected onto the plane. The stress state is then represented by a dot in the circle (i.e. $(\sigma_w, \tau_\mathrm{w})$ if we follow the notation in the previous stress transformation section). In this case, the shear failure along this particular plane is determined whether this dot touches the line or not.

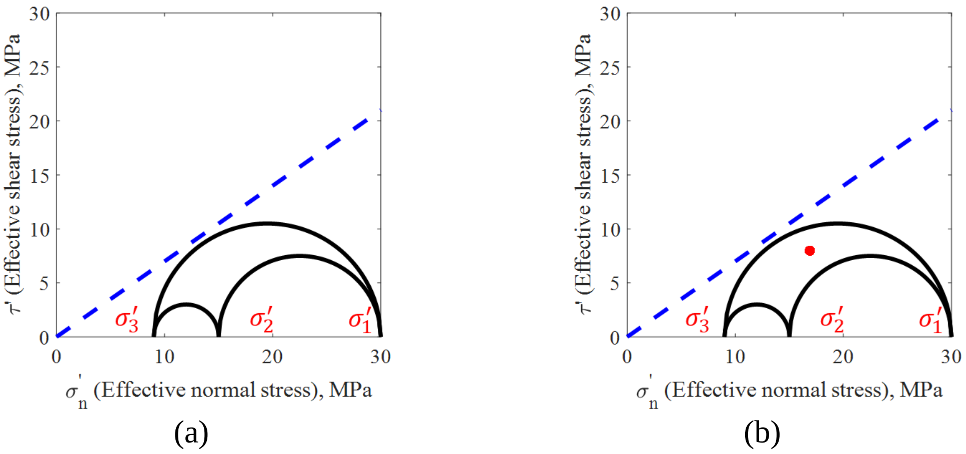

(a) (b)

Figure 82. Mohr-Coulomb shear failure criterion: (a) 3D Mohr circle (black circles) and Coulomb failure line (blue straight line) and (b) stress state for particular plane represented by red dot

Fault Slip Potential (FSP) is the probability for an existing fault to shear-fail, given pore pressure increase by fluid injection. Therefore, shear failure driven by poroelastic effect cannot be evaluated using the current FSP approach. The following is to provide detail examples of FSP calculation, associated with the use of the stress transformation, and how to interpret its results. Table 18 lists input parameters and their uncertainty ranges for the example FSP calculation. The input parameters are associated with principal stresses, maximum horizontal stress direction, pore pressure, fault property (friction coefficient) and fault geometry (dip and dip direction). For the demonstration purpose, we randomly sampled parameters from Table 18 to generate 16 cases which are summarized in Table 19. Note that vertical stress and pore pressure gradient are fixed to be 26.01MPa/km and 10MPa/km, respectively and the depth of 3,000m is assumed for the calculation.

Table 18. FSP calculation input parameters and their uncertainty range

Parameters	Base Value	Uncertainty
Sv (MPa/km)	26.01	0
Shmax (MPa/km)	25.55	3
Shmin (MPa/km)	14.20	1
Pore Pressure (MPa/km)	10.00	0
Shmax Azimuth (°)	32	16
Fault Friction Coefficient	0.7	0.1
Fault Dip (°)	60	10
Fault Dip Direction (°)	315	15

Table 19. Sampled parameters for 16 cases

Case	Shmax (MPa/km)	Shmin (MPa/km)	Shmax Azimuth (°)	Friction Coefficient	Dip Direction (°)	Dip Angle (°)	Critical Pp (MPa)
a	22.849	14.759	43.361	0.65071	318.54	67.146	0.8241
b	23.969	15.11	26.176	0.73255	308.58	57.81	5.0754
c	23.429	13.814	23.467	0.69973	322.68	54.743	3.5912
d	25.803	14.467	35.66	0.78782	315.3	50.482	6.2998
e	27.72	14.397	29.105	0.64694	327.76	59.659	0.6044
f	26.466	14.177	47.49	0.77579	311.8	68.429	1.5562
g	24.849	14.034	45.482	0.75549	320.31	64.677	0.3068
h	28.1	15.073	40.668	0.6742	306.61	63.545	2.2484
i	26.062	14.218	31.036	0.68097	329.8	61.687	1.4431
j	25.257	13.603	33.554	0.74104	304.33	57.355	-1.1726
k	24.285	13.41	37.442	0.7187	301.86	65.598	-3.0926
l	27.126	13.453	21.685	0.63248	325.47	55.053	0.4568
m	22.968	13.836	16.888	0.77091	320.82	51.773	8.8846
n	26.844	14.841	38.66	0.61181	309.56	69.636	0.705
o	28.187	13.254	19.106	0.70612	302.88	53.296	-1.8837
p	24.506	14.674	25.129	0.61572	313.39	61.238	-0.585

Given parameters, we projected the principal stresses onto the fault plane and visualized it in Mohr circle diagram. Figure 83 shows Mohr circle diagram of 16 cases based on parameters in Table 19. Among 16 cases, 4 cases show that the stress state touches or is above the failure line, highlighted by the red dot (Figure 83(j), (k), (o), and (p)). In this case, FSP for this particular fault plane is 25%. This value is based on static parameters while FSP should depend on pore pressure change which can be dynamically updated from flow simulation models. Based on Terzaghi'z effective stress law, increase in pore pressure decreases effective normal stress, the grain stress that is actually associated with the failure of geo-material, driving the Mohr circle toward the failure line. We investigated the sensitivity of pore pressure increase in FSP. Assuming 1MPa and 2MPa of pore pressure increase, the Mohr circle diagrams are updated in Figure 84 and Figure 85, respectively. It is found that the increase in pore pressure makes the faults more vulnerable for the slip. For example, case (j) does not meet the failure criterion with 0 (Figure 83) and 1MPa (Figure 84) pressure increase yet the criterion is satisfied with 2MPa pressure increase (Figure 85). With 1MPa increase in pore pressure, 9 cases satisfy the failure criterion, providing FSP of 56%. With the 2MPa increase, FSP increases to 69%.

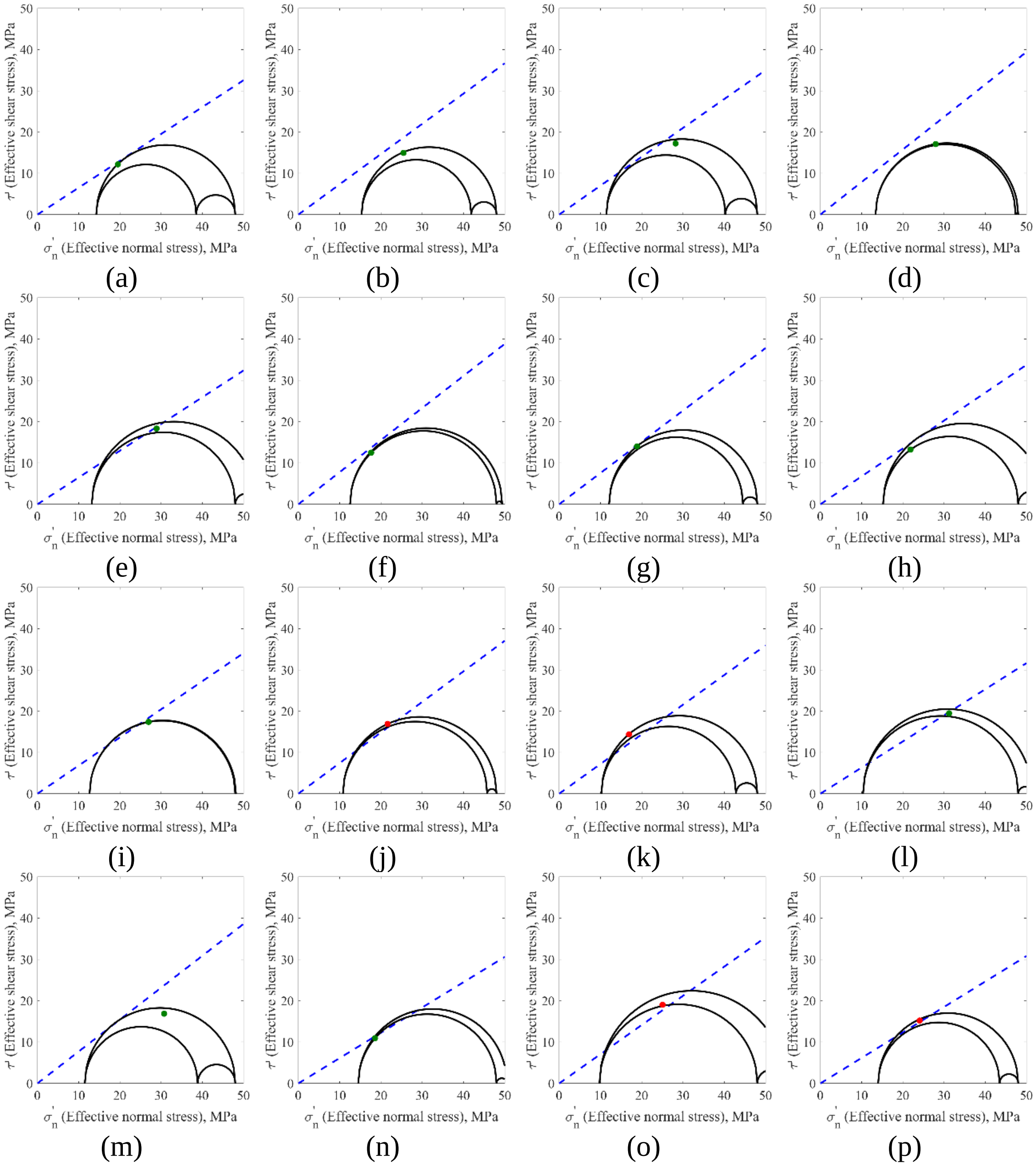

(a) (b) (c) (d)
(e) (f) (g) (h)
(i) (j) (k) (l)
(m) (n) (o) (p)

Figure 83. Mohr circle diagram of 16 cases based on Table 19

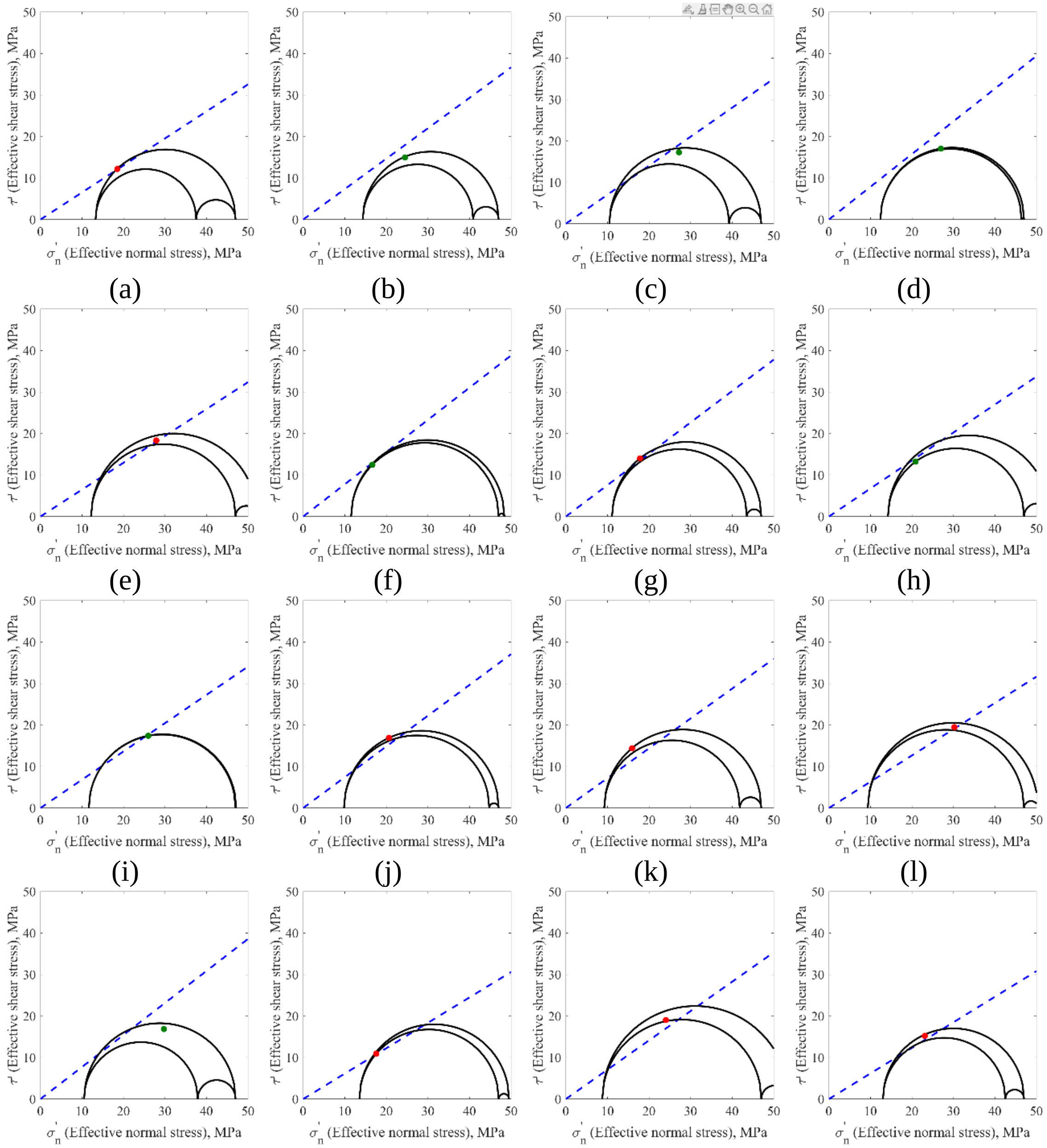

(a) (b) (c) (d)

(e) (f) (g) (h)

(i) (j) (k) (l)

(m) (n) (o) (p)

Figure 84. Mohr circle diagram of 16 cases based on Table 19 with 1MPa pressure increase

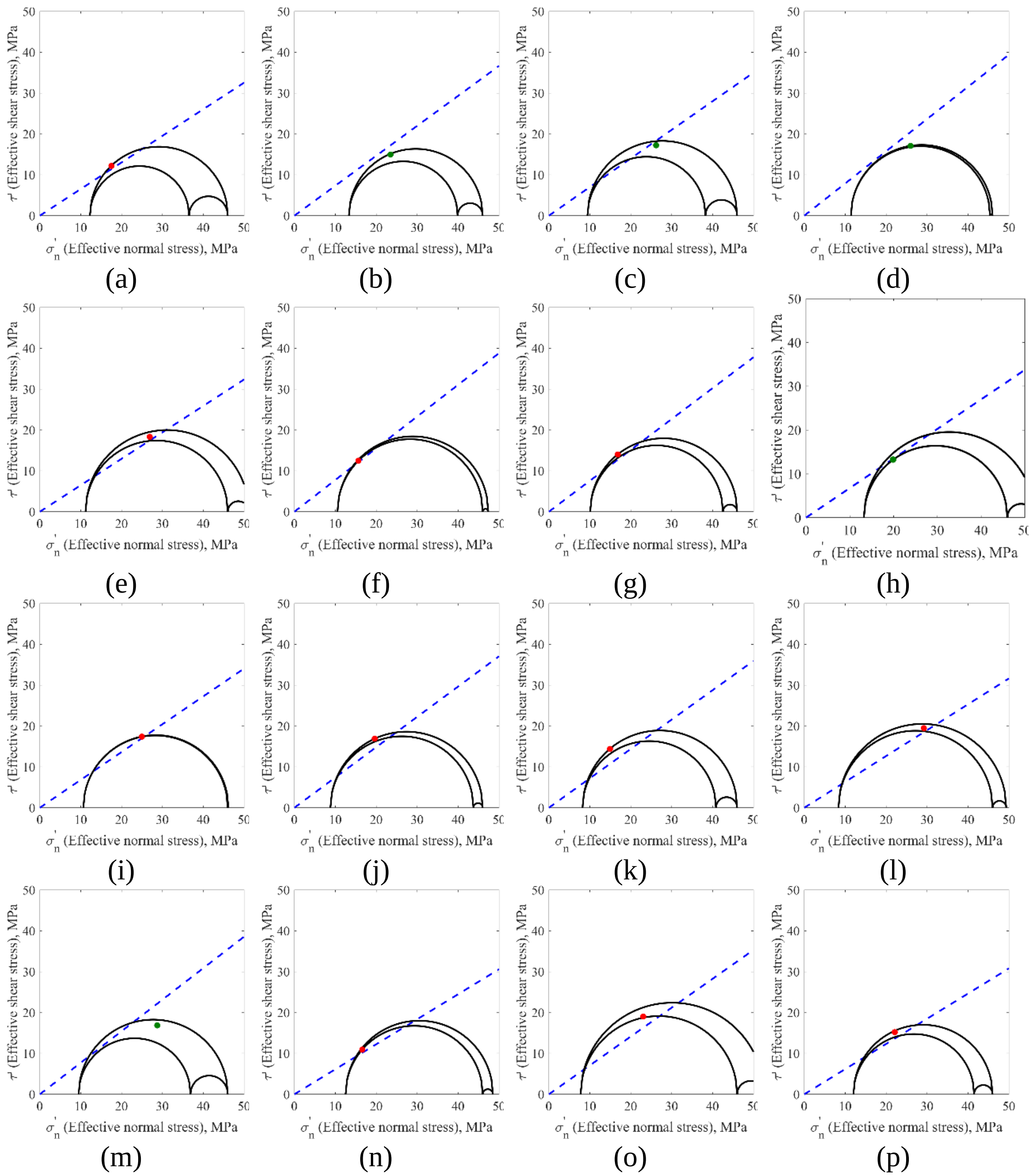

(a) (b) (c) (d)

(e) (f) (g) (h)

(i) (j) (k) (l)

(m) (n) (o) (p)

Figure 85. Mohr circle diagram of 16 cases based on Table 19 with 2MPa pressure increase

The above demonstration can be summarized into cumulative distribution function (CDF) of the critical pore pressure. The horizontal distance between the failure line and the stress state, $\Delta\sigma_n^{'}$, is defined as critical pore pressure, the necessary pore pressure to start a shear failure (Finkbeiner et al., 2001). The last column in Table 19 indicates the critical pore pressure based on the Mohr circle diagrams in Figure 83. We visualize the critical pore pressure in histogram. Figure 86(a) shows that the critical pore pressure is concentrated in lower values, implying that the fault is originally critically stressed, favorable for the fault slip to occur. The continuous CDF in Figure 86(b) indicates that FSP with 1MPa and 2MPa pressure increase is 0.58 and 0.78, respectively. The discrepancy in FSP calculation between Mohr circle diagram and CDF will diminish with larger number of samples.

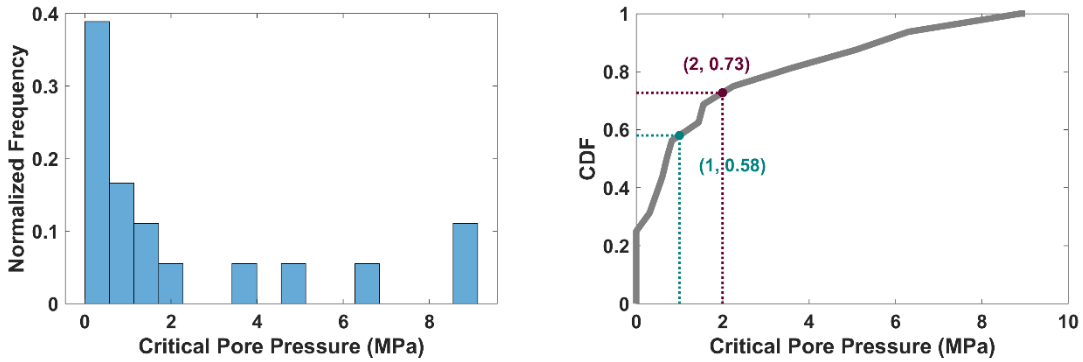

(a) (b)

Figure 86. Histogram and cumulative distribution function of critical pore pressure in Table 19